



**Politecnico
di Torino**



POLITECNICO DI TORINO

Master of Science in Mechanical Engineering

Master's Thesis

Investigation of the effect of porosity on fatigue behavior for DMLS built parts using 3D X-ray Computed Tomography

Supervisors

(Politecnico di Torino)

Prof. Luca Iuliano

Asst. Prof. Abdollah Saboori

(Leibniz Universität Hannover)

Prof. Dr.-Ing. Roland Lachmayer

M. Sc. Behrend Bode

Candidate

Taha Hakan Demirci

Academic Year 2021-2022

ACKNOWLEDGEMENTS

First, I would like to express my gratitude to Prof. Roland Lachmayer and M.Sc. Behrend Bode for giving me this opportunity to write my master's thesis in this lovely city, Hannover. Also, I should express my appreciation to M.Sc. Patrik Müller for making this long time pass easier by being friendly and available whenever I needed guidance through all the stages of my master's thesis. He and M.Sc. Bode selflessly shared their knowledge and showed a strong will to support me all this time. It would have been a different story without their guidance and mentorship. I must admit that I consider myself lucky to have had the opportunity to work with them; it would have been very boring if they weren't there.

I wish to thank my supervisors from Politecnico di Torino, Prof. Luca Iuliano, and Asst. Prof. Abdollah Saboori for giving me the chance to conduct my master's thesis in Germany by allowing me to handle all the bureaucratic processes easily with their fast responses.

Moreover, all the experiments were carried out at Institut für Produktentwicklung und Gerätebau (IPeG) at Leibniz Universität Hannover. I am grateful for the availability of tools and all kinds of equipment that I needed to conduct the experiments. I want to thank all the institute staff for being helpful and for their excellent collaboration.

Finally, I would like to express my deepest gratitude to my family for their all kinds of support during this period and in my life. I could not have undertaken this journey without their continuous trust in me.

ABSTRACT

Following recent developments in manufacturing technology, Additive Manufacturing (AM) has become an important figure in the production of complex geometries in which conventional subtractive methods are typically incapable of producing or are excessively high costs. However, AM techniques have their capabilities and limitations. One limitation that affects mechanical properties, particularly fatigue strength under cyclic loads, is unwanted material porosity causing fatigue failure. Fatigue failure, due to its nature, is random, and a reason for this stochastic nature is the uncertainty of the porosity dispersion in the AM-built part. A commonly used AM process is Laser Powder Bed Fusion (LPBF), which can print near full-density (99.5+%) parts if process parameters are set correctly. Therefore, EOSINT M 280 printer based on Direct Metal Laser Sintering (DMLS) technology, which is also an LPBF technique, was used to manufacture fatigue test specimens using 1.2709 metal powder with a chemical composition 18Ni9Co5Mo1Ti. Porosity in twenty-five fatigue specimens was analyzed using 3D X-ray Computed Tomography (XCT). Bruker SkyScan 1275 micro-CT was used to scan the samples. Fatigue tests were performed with a custom-made torsion fatigue test machine. Twenty tests have been conducted, five tests each for four different torsion angles at 5 Hz frequency and $R = -1$. Fatigue test results were compared with the porosity values measured by XCT in order to build a stochastic material model for predicting the fatigue lives of larger-sized objects in which scanning for porosity is not applicable.

TABLE OF CONTENTS

ACKNOWLEDGEMENTS	II
ABSTRACT	III
ABBREVIATIONS	X
NOMENCLATURE	XI
1. INTRODUCTION	1
2. FUNDAMENTALS	3
2.1. Additive Manufacturing Technology.....	3
2.1.1. Powder Bed Fusion	5
2.1.2. Laser Powder Bed Fusion	8
2.2. Fatigue	17
2.2.1 Wöhler Curve	17
2.2.2 Fatigue Life Prediction.....	18
2.2.3 Cyclic Loading in Fatigue Testing	18
2.2.3 Fatigue Beach Marks.....	20
2.3. X-ray Computed Tomography	22
3. METHODS.....	26
3.1. Research Problem	26
3.2 Previous Research.....	26
3.3 Experimental Methodology	29
3.2.1 Fatigue Testing Bench.....	29
3.2.2 Specimen Material.....	31
3.2.3 Specimen Geometry	32
3.2.4 Surface Treatment	35
3.2.5 Torsion Fatigue Test Machine	36
3.2.6 Custom Grip Design.....	38
3.2.7 Alignment Check.....	40
3.2.8 Instrumentation for Monitoring.....	41
3.2.9 Motor.....	41

3.2.10 X-ray Computed Tomography Scans	42
3.2.11 Critical Region and Pore Location Effect	51
3.2.12 Fatigue Test Procedure	55
3.4 Obstacles and Solutions	61
4. RESULTS	62
4.1 CT Scan Results	63
4.2 Fatigue Test Results	71
4.2.1 Porosity Ratios and Fatigue Life Comparison	72
4.2.2 Correlation Analysis	76
4.2.3 S-N Curve	80
5. CONCLUSIONS, RECOMMENDATIONS, AND LIMITATIONS	81
APPENDIX A	84
REFERENCES	87

LIST OF TABLES

Table 3. 1: Chemical composition of MetcoAdd C300-A.....	31
Table 3. 2: Particle size distribution and hall flow of MetcoAdd C300-A.....	31
Table 3. 3: Material specifications of MetcoAdd C300-A	31
Table 3. 4: Typical post heat treatment properties of MetcoAdd C300-A	31
Table 3. 5: Dimensions chosen for the specimen	34
Table 3. 6: Lenze MCS 14L15 synchronous servo motor data	41
Table 3. 7: SkyScan 1275 micro-CT Specifications.....	43
Table 3. 8: Scanning Parameters	43
Table 3. 9: Twist angle, torque, and stress values for the tests	57
Table 4. 1: CTAn Porosity Results.....	64
Table 4. 2: Unpaired t-test of Object Density: Tabular Results	66
Table 4. 3: Pore size range.....	69
Table 4. 4: % Pore size volume in range for all specimens.....	70
Table 4. 5: Porosity and N_f values of fatigue specimens.....	71
Table 4. 6: Interpretation of the correlation coefficient r	77
Table 4. 7: Correlation results of total porosity vs. N_f	77
Table 4. 8: Correlation results of total porosity vs. N_f	78
Table 4. 9: Correlation results of total porosity vs. N_f	78
Table 4. 10: Correlation results of total porosity vs. N_f	79
Table 4. 11: Correlation results of total porosity vs. N_f	79

LIST OF FIGURES

Figure 2. 1: Additive Manufacturing Evolution Timeline [23]	4
Figure 2. 2: Powder Bed Fusion Process [29]	6
Figure 2. 3: Characteristic flaws of PBF processes [28]	7
Figure 2. 4: Common defects in the SLS process [46]	9
Figure 2. 5: Schematic diagram of process parameters of LPBF processes [49]	10
Figure 2. 6: Sintering neck process [50]	11
Figure 2. 7: Correlation between laser power and scan speed with porosity [52]	12
Figure 2. 8: Laser input energy density against porosity [46] [53]	13
Figure 2. 9: Influence of layer thickness on porosity of SLS printed samples [56]	14
Figure 2. 10: Influence of hatch space on porosity of SLS printed samples [56]	14
Figure 2. 11: Representative Wöhler/SN Curve [65]	17
Figure 2. 12: Examples of (a) fully reversed sinusoidal loading, (b) repeated stress, and (c) fluctuating stress [68]	20
Figure 2. 13: Beach marks showing the fatigue crack initiation, nucleation, and final fracture [70]	20
Figure 2. 14: Beach marks caused by different magnitudes of loads [71]	21
Figure 2. 15: Working principle of X-ray CT technology [74]	23
Figure 2. 16: X-ray tube (a) an X-ray tube schematic [77], (b) Bruker metal-ceramic sealed tube [78]	23
Figure 2. 17: Two 3D CT constructed volumes showing the porosity/defects [86]	25
Figure 3. 1: Fracture surface analysis and X-ray tomography prior to fatigue tests, allowing visualization of all pores in region of failure – highlighting the “killer pore” [91]	28
Figure 3. 2: Methodological approach steps	29
Figure 3. 3: Standard rotary bending fatigue testing machine setups according to DIN 50113	29
Figure 3. 4: Example of Morrison torsion grip in compliance with ISO 1352 [95]	30
Figure 3. 5: Specimen with circular cross-section	32
Figure 3. 6: Circular specimen end	32
Figure 3. 7: Stress contours on a cut section of the torsion specimen model	33
Figure 3. 8: Maximum and minimum shear stresses	34
Figure 3. 9: Rotary surface grinding machine	35
Figure 3. 10: As built specimens and a surface grinded specimen mounted on the machine	35
Figure 3. 11: Torsion Test Rig	36
Figure 3. 12: Test rig CAD model	37

Figure 3. 13: Thin plates.....	38
Figure 3. 14: ER16 clamping nut and collet.....	39
Figure 3. 15: Collet Holder design guidelines according to DIN 15488.....	39
Figure 3. 16: Collet holder.....	40
Figure 3. 17: Split muff coupling	40
Figure 3. 18: Split bar for axial alignment.....	40
Figure 3. 19: Cycle counter	41
Figure 3. 20: Bruker SkyScan 1275 3D X-ray Micro-CT Setup.....	42
Figure 3. 21: Brightness level stabilization by time	44
Figure 3. 22: Brightness level for the torsion specimen.....	44
Figure 3. 23: Area of interest for reconstruction	45
Figure 3. 24: Binary CT scan images (a) gauge section, (b) grip section	46
Figure 3. 25: NRecon parameters settings.....	46
Figure 3. 26: Greyscale area difference (a) too black (b) too white (c) optimal range	47
Figure 3. 27: Ring artifacts (a) ring artifacts are visible (b) no ring artifacts.....	47
Figure 3. 28: Beam hardening correction (a) 30% correction, (b) 45% correction.....	48
Figure 3. 29: Misalignment compensation (a) -1, (b) 2.....	48
Figure 3. 30: Binary images showing the grayscale threshold difference (a) CT image of a layer showing pores, (b) a good binary image, (c) a binary image containing noise, (d) a binary image missing some pores.....	49
Figure 3. 31: 3D models of two specimens showing porosity (a) specimen 14, (b) specimen 15	51
Figure 3. 32: Distribution of Misses and S22 stress of FEM models: (a) non-porous model (b) model containing $\varnothing 0.09$ mm pore and 0.16 mm distance under specimen [97]	52
Figure 3. 33: Stress contours with the pores: (a) Shear stress S13, (b) von Mises.....	53
Figure 3. 34: Stress contours of the non-porous model: (a) von Mises, (b) Shear stress S13	54
Figure 3. 35: Specimen 16: (a) all pores, (b) pores in the critical area.....	55
Figure 3. 36: Oscilloscope for torque cycle.....	56
Figure 3.37: Torsional stress, torsional moment, and section modulus diagrams.....	59
Figure 3. 38: Beach marks captured by the microscope: (a) specimen 5, (b) specimen 23	60
Figure 4. 1: Specimen relative density percentages	63
Figure 4. 2: Object Density: (a) Normal QQ plot, (b) Histogram with frequency distribution.....	65
Figure 4. 3: Estimation plot: Unpaired t-test of Object Density of two groups	66
Figure 4. 4: Total Porosity: (a) Normal QQ plot, (b) Histogram with frequency distribution	67

Figure 4. 5: Open Porosity: (a) Normal QQ plot, (b) Histogram with frequency distribution	67
Figure 4. 6: Closed Porosity: (a) Normal QQ plot, (b) Histogram with frequency distribution.....	67
Figure 4. 7: Number of Closed Pores: (a) Normal QQ plot, (b) Histogram with frequency distribution.....	68
Figure 4. 8: Closed and open porosity scatter of the samples	68
Figure 4. 9: % Pore size volume in range for fatigue specimens	70
Figure 4. 10: Total porosity vs. number of cycles to failure (Nf).....	72
Figure 4. 11: Closed porosity vs. number of cycles to failure (Nf)	73
Figure 4. 12: Open porosity vs. number of cycles to failure (Nf).....	73
Figure 4. 13: Number of closed pores vs. number of cycles to failure (Nf)	74
Figure 4. 14: Number of pores in critical area vs. number of cycles to failure (Nf)	74
Figure 4. 15: Fatigue life depending on the pore size	75
Figure 4. 16: Log-log plot of the angle of twist vs. number of cycles to failure (Nf)	80
Figure A. 1: ER16 Collet Holder Technical Drawing	84
Figure A. 2: Torsional Fatigue Test Specimen Technical Drawing	85
Figure A. 3: Straight Plate Technical Drawing	86

ABBREVIATIONS

<i>AM</i>	Additive Manufacturing
<i>ASTM</i>	American Society for Testing and Materials
<i>CAD</i>	Computer Aided Design
<i>CT</i>	Computed Tomography
<i>DIN</i>	Deutsches Institut für Normung
<i>DMLS</i>	Direct Metal Laser Sintering
<i>HCF</i>	High Cycle Fatigue
<i>IPeG</i>	Institut für Produktentwicklung und Gerätebau
<i>ISO</i>	International Standard Organization
<i>LCF</i>	Low Cycle Fatigue
<i>LPBF</i>	Laser Powder Bed Fusion
<i>PBF</i>	Powder Bed Fusion
<i>RP</i>	Rapid Manufacturing
<i>SEM</i>	Scanning Electron Microscope
<i>SLM</i>	Selective Laser Melting
<i>SLS</i>	Selective Laser Sintering
<i>STL</i>	Standard Triangle Language
<i>XCT</i>	X-Ray Computed Tomography

NOMENCLATURE

c	[m/s]	Light velocity
h	[Js]	Planck constant
I_0	[A]	Continuous standstill current
I_{\max}	[A]	Maximum current
I_r	[A]	Rated current
J_{mot}	[kgcm ²]	Moment of inertia of the motor
M_0	[Nm]	Continuous standstill torque
M_{\max}	[Nm]	Maximum torque
M_r	[Nm]	Rated torque
M_t	[Nm]	Torsional moment
N_f	[cycle]	Number of cycles to failure
n_r	[rpm]	Rated speed
P_r	[kW]	Rated power
R	[-]	Stress ratio
R_m	[MPa]	Tensile strength
$R_{p0.2}$	[MPa]	Yield strength
W_t	[mm ³]	Section modulus for torsion
Q	[J/mm ³]	Laser Input Energy Density
λ	[mm]	X-ray wavelength
τ	[MPa]	Shear stress
τ_a	[MPa]	Stress amplitude
τ_{\max}	[MPa]	Maximum stress
τ_{\min}	[MPa]	Minimum stress

1. INTRODUCTION

Additive Manufacturing (AM) is the process of joining materials layer upon layer to create three-dimensional (3D) objects from the desired 3D model data [1]. There are seven major types of AM [2], [3]. Among them, Powder Bed Fusion (PBF) is a commonly used method for the metal AM. PBF has been further categorized into several methods in which one of them is Laser Powder Bed Fusion (LPBF). LPBF is a promising technology that has gained attention in the industry due to its ability to fabricate high-quality, near-net-shape parts with near full density [4], [5]. However, it still has a relatively poor surface finish and dimensional accuracy compared to conventional subtractive manufacturing methods that slackens its widespread applications [6].

It is possible to manufacture complex-shaped and high-value metal parts by the AM technology to be used in critical applications, for example aerospace applications such as jet engines and turbine blades [7]. Since these applications have crucial importance, the durability of those components must be predicted and reliable. Even though AM technology has advanced a lot and proved its functional trustworthiness in recent years, there are still some characteristic issues, such as undesirable material porosity and surface roughness, that could lead the components to a premature fatigue failure. Fatigue failure of the AM parts is mainly driven by the presence of porosity and surface roughness, although surface roughness is relatively easy to improve by removing some material on the surface by various techniques. However, the surface roughness may still be a problem for the complex components with internal features since they cannot be post-machined internally [8].

Fatigue phenomenon, by its nature, is known to be a stochastic process [9], [10]. Fatigue failure occurs when a material is subjected to a cyclic application of loads that produce stresses or strains in the material, leading to changes in the material's microstructure resulting in crack initiation, propagation, and a sudden final failure [11]. Fatigue life prediction of AM or even conventionally manufactured metal parts is still a challenging problem despite the amount of research done in the past years [12]. Especially for AM-built components, varied fatigue behavior will be observed for a number of identical parts, possibly depending on the different porosity ratios.

Some destructive and non-destructive material inspection methods can help predict fatigue behavior. One of the non-destructive methods is X-ray Computed Tomography (XCT). XCT scans have been used commonly for porosity analysis to derive the fatigue behavior of metal parts by many researchers especially in the past decade. Ziótkowski et al. [13] used XCT to detect porosity in SLM-built 316L stainless steel specimens and found the pores'

size, shape, and orientation. According to the data obtained by the XCT, it was possible to determine the direction of the cracks and diagnose places that may be the point of fatigue crack initiation. In another research conducted by Biswal et al. [14], the XCT method was used periodically with interrupted fatigue testing to find out the pores that initiate and propagate the fatigue cracks of the wire + arc AM produced Ti-6Al-4V. They used XCT at intervals during the fatigue tests and discovered pores that increased their original size with the increase of load cycles. Also, Tammas-Williams et al. [15] used XCT to confirm that the presence of porosity strongly influences the fatigue life of AM-produced parts. Moreover, Plessis et al. [16] concluded that fatigue failure is more prone to depend on the total porosity extent and pores on the surface and within 1 mm of the surface. They are the typical crack initiation points, and the largest pores are likely to be the killer defects. They also noted that this issue had been underestimated up until the advances of the XCT method and the progress of LPBF materials. These developments led to the detection of surface and sub-surface pores as critical for fatigue phenomenon.

The purpose of this master's thesis is to determine the effect of uncertain porosity dispersion caused by the LPBF processes on fatigue behavior. The fatigue behavior of different parts produced by the same LPBF machine can be derived from the XCT scans by finding a correlation between the porosity ratios and the number of cycles to failure observed from the fatigue tests. Hence, the fatigue behavior of larger-sized parts that the XCT cannot scan due to dimension constraints can be predicted with this method. In this research, similarly to the previous works done, non-destructive XCT scans were run prior to the fatigue tests to gather useful information about the defect population, such as total, open, and closed porosity percentages, part densities, object and defect volumes, pore sizes, the total number of pores and the number of pores in the critical area. Torsion fatigue tests have been carried out with constant stress amplitudes with a stress ratio of $R = -1$. Four different twist angles were chosen to depict the scatter of fatigue lives under different stress levels, one in Low Cycle Fatigue (LCF) and three in High Cycle Fatigue (HCF) region. A total of twenty-five samples were scanned by XCT, and twenty of them were fatigue tested. From this point of view, assuming that there is a correlation between the material porosity and fatigue life, developing a stochastic model for fatigue failure due to random porosity distribution of the LPBF-built 1.2709 AM parts is the goal of this work. Hence, A statistical material model is aimed to be developed for the correlation between the porosity and fatigue failure within the framework of the applied non-destructive material inspection method XCT.

2. FUNDAMENTALS

2.1. Additive Manufacturing Technology

The first steps of Additive Manufacturing (AM) were driven by the invention of Rapid Prototyping (RP) by Hideo Kodama and Charles Hull in the 1980s with the development of 3D printing [17]. Since then, RP has immensely improved to include different forms of manufacturing techniques. The initial process was called *stereolithography*¹ and it was based on photo-polymerization, which first processed acrylates and then epoxies later. In the following years, new layer-based processes were developed, and an extended range of materials became qualified for AM applications, and all of them were plastics. Around the turn of the millennium, processes for making metal parts were introduced to the market [18]. In the early stages of the invention of RP, it has been mostly used for conceptual, functional, and technical prototypes. Following the developments of rapid tooling, rapid casting, and rapid manufacturing for tooling applications, casting applications, and pre-series production respectively, finally, AM has become a reality after the 2000s for end-usable products and is typically associated with production technologies and supply chains. Especially, the early 2000s were great times of achievement for the AM technology; in fact, the first commercially workable Selective Laser Sintering (SLS) printing machine which is also the printing technology used for this research was found around these years [19], [20].

Nowadays, AM technology is considered an indispensable figure in the industry; especially where there is a need for complex parts which would have been very difficult and costly to manufacture by conventional techniques like milling and casting. AM technology promises higher design freedom and therefore, an improved part performance consequently [20].

AM, as can be understood by its name too is a manufacturing technique that creates 3D objects by adding layer upon layer. It uses computer-aided design (CAD) or 3D object scanners that is later converted to stereolithography (STL) file to create parts that are very precise in geometry. In this process, the drawing created in the CAD software is approximated by triangles and sliced into very thin layers that contain the information of each layer to be printed [21]. This technique of manufacturing also helps reduce the excessive amounts of material wasting thanks to the layer-by-layer technology as opposed to the conventional manufacturing techniques that usually need machining or other methods to remove extra material from the final part [20]. As AM has evolved rapidly in

¹ Stereolithography is an additive manufacturing technology that transforms thermoset polymers in liquid form to physical objects by solidification using light as an energy source.

recent years, new industries have begun to embrace this technology in their applications. The top industries that use AM are aerospace, automotive, medical, pharmaceutical, infrastructure and, energy industries. Also, there are fields that adopted AM lately such as edible goods, sports and, consumer products industries. The aerospace industry uses the advantage of AM thanks to the possibility of manufacturing lighter structures to reduce weight. Architects can work more flexibly and easier since AM is able to create very complex parts precisely reducing the possibility of infrastructure accidents from construction mistakes and poor design. The medical industry has entered a new era thanks to AM which allows for 3D printed dental appliances and custom-made devices, such as dentures, crowns, and even Invisalign to be constructed from a variety of substrates and prints customized to anybody [21], [22].

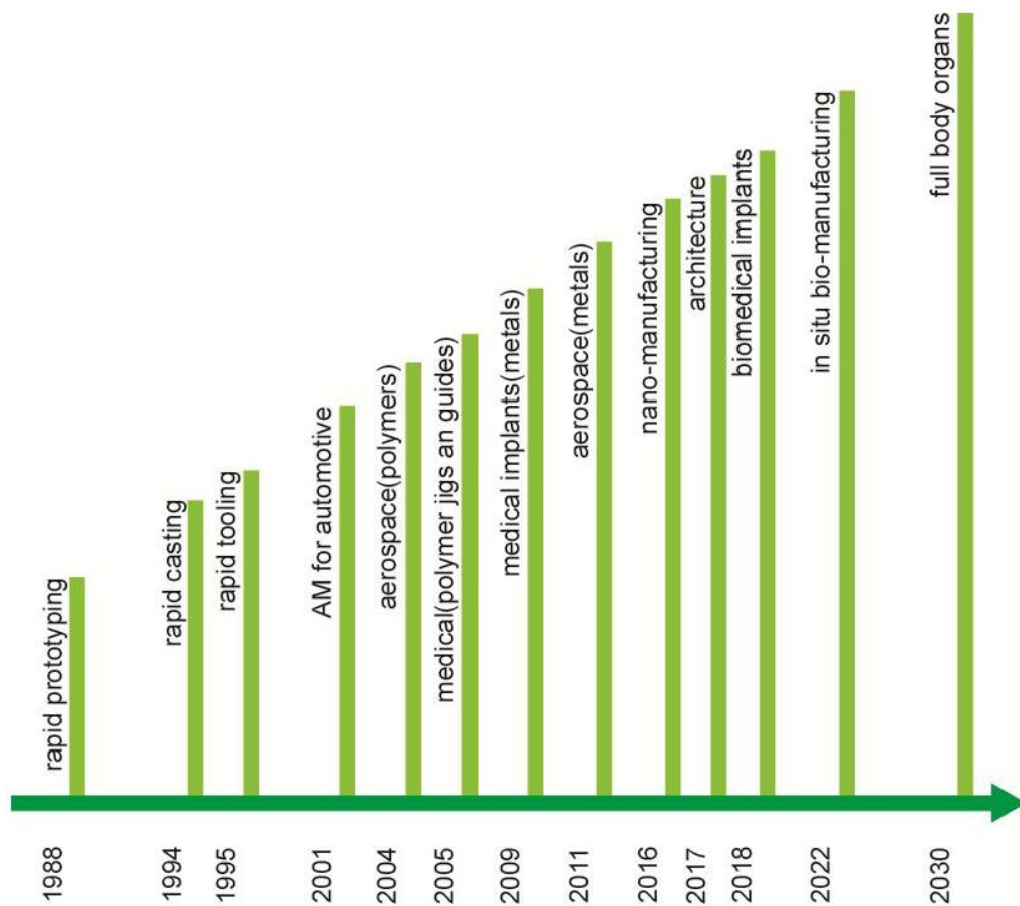


Figure 2. 1: Additive Manufacturing Evolution Timeline [23]

As seen from the figure above, AM technology has grown immensely. It is even foreseen that it will be possible to print full body organs and will be largely utilized substitute for donor organs by 2030 according to Delphi projections for 2030. However, while experts acknowledge that full-body organ bioprinting is very likely to be realized in the future, their unanimous idea states that printing simpler body organs such as tooth implants or

tissue should be possible to achieve by 2030 but there might be additional 10 years for reaching the point where human organs can be accessible by 3D printing [24].

As AM technology evolves, different classes of materials are now associated with specific AM techniques. Materials such as polymers, ceramics, composites, and metals are manufactured by various AM techniques. A specific committee formed by ASTM² which is known as ASTM F42 Committee standardized the common AM techniques that are commonly embraced in the worldwide. ASTM F2792 – 12a Standard Terminology suggests the AM processes as follows Powder Bed Fusion (PBF), Binder Jetting, Directed Energy Deposition, Material Extrusion, Material Jetting, Sheet Lamination, and Vat Photopolymerization.

PBF methods utilize metal, polymer, and ceramic as material. In this thesis, the material used for printing samples is metal. More specifically a maraging class steel 1.2709 (also known as X3NiCoMoTi18-9-5) metal powder. Generally, maraging steels are known to be high alloy steels with a very low carbon percentage which use substitutional elements to produce precipitation hardening in iron-nickel martensite. Maraging steels can usually achieve very high strength and toughness with proper heat-treatments (aging) [25]. There are various methods to print metals by AM. Powder Bed Fusion (PBF) processes are widely used for this purpose. Electron Beam Melting (EBM), Selective Laser Sintering (SLS) -or Direct Metal Laser Sintering (DMLS) in other name- and Selective Laser Melting (SLM) are known to be the three processes of PBF type AM [26].

2.1.1. Powder Bed Fusion

Powder Bed Fusion is one the fundamental categories of 3D printing. PBF processes use a laser or electron beam to selectively fuse and sinter metallic powder in regions of the powder bed, layer upon layer. When the energy source is a laser beam, the process is called Laser Powder Bed Fusion (LPBF). PBF techniques share the basic principles of all AM processes (layer by layer printing directly from 3D model). Similarly, to other AM techniques, PBF has advantages such as being cost-effective and reduced assembly. Because of their higher cooling rate and good surface finish when compared to other AM processes, they have received a significant attention in the engineering applications. Hence, PBF processes were among the first commercialized AM processes [27].

Despite the significant development and utilization of PBF processes, there are certain and unique process-based flaws for each PBF method. One of which is known as porosity, and it may occur inside or at the outer surface of the printed parts. These naturally occurring

² ASTM: ASTM is one of the world's largest international standards developing organizations. Their standards are used and accepted worldwide and cover areas such as metals, paints, plastics, textiles, petroleum, construction, energy, the environment, consumer products, medical services, devices and electronics, advanced materials, and much more [100].

defects are unique in shape, size, and location [28]. Each of these features affect certain mechanical behavior of the material, and they will be examined in the next chapters.

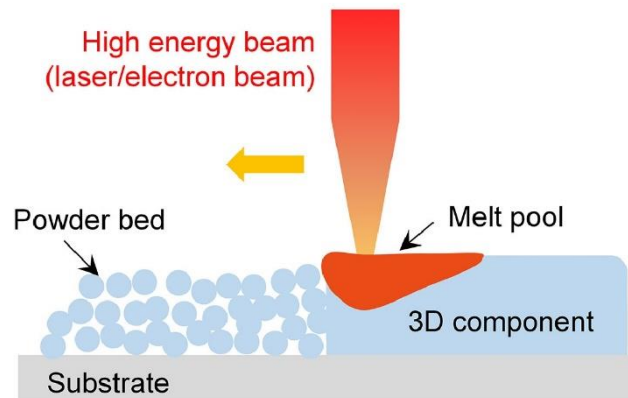


Figure 2. 2: Powder Bed Fusion Process [29]

Additional to the above figure, usually, a coater blade or a roller spreads a thin layer of powder across a build surface. That is how the energy source melts/sinters the material required for that layer which is on the build plate. Then the build plate descends to make way for the next layer. Extra unused material can be recycled [26].

Another essential aspect of LPBF processes is that the part that is being printed is welded to the build plate as it is being built. It is supported and secured by support structures attached to the build plate. Support structures hold the incomplete part against distorting from the thermal effects of the heat that the laser beam is introducing. Support structures are sacrificial materials, and they are dumped after the part is complete. After the print, the post-processing step must be carried out. Such steps are removing the unused powder, heating the entire build platform to relieve any of the stresses that might have been built up, cutting the parts off the build plate, and removing the support structures [26]. Moreover, the LPBF process will leave a rough surface finish on the parts. Therefore, some surface treatment should be done. An example of this surface roughness fixation can be achieved by a rotary surface grinding machine as it is an available source of surface treatment machine available at the IPeG workshop.

Although conventional subtractive manufacturing methods are dominated the industry, LPBF is a promising technology for some of the advantages it has such as giving flexibility for designers to create very complex geometries, lightweight construction by lattice structures without using excessive material, getting in the near-net shape and functional integrity for the desired components [30], [31]. It is also good for working with generative design and topology optimization [32]. However, it must be noted that to utilize all these advantages, the component designed should have a high complexity with a significant number of thin-walled parts. As opposed to the conventional manufacturing

methods, the dimensional accuracy often poses a challenge in LPBF [33]. Some of the good applications of LPBF processes include medical implants, complex metal parts for instance aircraft engine components, components for spacecrafts, automotive sector, and producing brackets to connect two members in an assembly [34], [35].

Despite having lots of advantages, PBF methods have some process-based flaws too. Characteristic flaws of PBF processes include gas porosity, lack-of-fusion, and melt pool instabilities and each flaw formation mechanism can be considered as being either systematic or stochastic in nature [28]. It is commonly accepted that these defects can degrade mechanical properties of additively manufactured components. They not only affect the static mechanical performance, but dynamic properties as well such as fatigue behavior under cyclic loading. However, the mechanisms by which these flaws form are still discussed, and their role on dynamic material properties are yet to be explored [28]. This master’s thesis tries to make a step in understanding the impacts of these stochastic flaws, more specifically porosity, on the fatigue life. PBF processes can usually achieve part densities above 99.5% depending on several parameters like material powder composition, layer thickness of the 3D printer, laser power, build orientation etc. This 99.5+% density ratio is also confirmed by this work by printing twenty-five samples with an LPBF 3D printer and detecting their porosity percentages with the help of a micro-CT scanner that is available in the laboratory of IPeG. However, even with parameter optimization, these flaws are still capable of degrading the static and dynamic mechanical properties of an additively manufactured part. It is especially important to understand how the porosity distribution inside or on the surface of a part will affect the fatigue life.

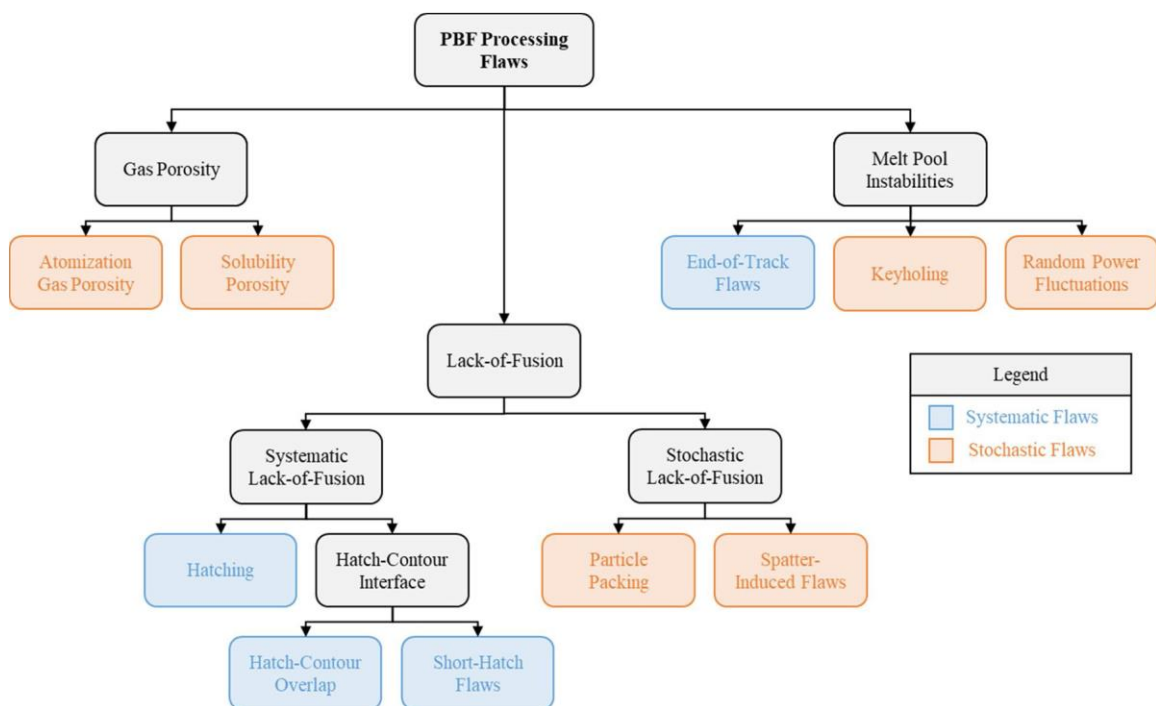


Figure 2. 3: Characteristic flaws of PBF processes [28]

Gas pores defined as porosity arising from trapped gas within the melt pool, are thought to originate from two sources as shown in Fig 2.3: the release of gas trapped in the powder during the gas atomization process [36], [37] and gas bubble nucleation in the melt pool due to the high solubility of interstitial elements in the liquid phase coupled with rapid solidification. [28], [36], [38]. They are usually small and typically spherical [28]. Previous research has found that PBF feedstock usually contains porosity due to the inert gas used during atomization. This porosity is the source of gas pores in the final PBF component [36], [37]. Most of the powder feedstock used in PBF processes is gas atomized including the metal powder used in this work. The powder feedstock used for our LPBF printer OERLIKON MetcoAdd™ C300-A is manufactured gas atomized with the inert gas argon. During gas atomization, a tundish of molten metal is fed through a small aperture, and the resulting stream is exposed to a high-velocity inert gas [28], in this case argon.

Lack-of-fusion is another type of typical flaws of PBF systems. Differently from gas pores, they are usually irregular and large which make them detrimental for static and dynamic loading conditions. These types of flaws can be systematic or stochastic. Systematic lack-of-fusion flaws arise because of the non-optimal choices of hatching process parameters such as layer thickness, hatch spacing, hatch overlap, hatch overlap, etc., when the laser power and scan speed parameters are chosen optimally. Consequently, the fusion zone is inadequate to provide complete melting or sintering. When the lack-of-fusion flaws are still in present even with the optimal energy and hatching process parameters, it can be a sign of stochastic lack-of-fusion flaws related to localized deviations from nominal processing conditions [28], [39].

Melt pool instabilities (systematic) occur in an irregular and/or discontinuous track, which lead to a high surface roughness and material porosity due to balling in the parts. The stability of a melt pool increases with the increase in laser power. However, the stable zone becomes narrower for the materials with a high thermal conductivity at a given laser power and layer thickness [40], [41]. Similar to lack-of-fusion flaws, they can be systematic or stochastic. Random power fluctuations and keyholing can cause stochastic melt pool instabilities resulting material voids [28]. Keyholing is known as the depression formed within the melt pool when the material evaporation generates an evaporation pressure [42].

2.1.2. Laser Powder Bed Fusion

Laser Powder Bed Fusion (LPBF) also commonly known as Selective Laser Melting (SLM), Selective Laser Sintering (SLS) and/or Direct Metal Laser Sintering (DMLS) are essentially of the same type of PBF methods. These methods use the same principle when operating, yet they differ in technicalities and materials used. SLS was initially done

mainly on polymers and nylons to create prototypes for auto-visual help and fit-to-form tests. Gradually, it was expanded to include metals and alloys to manufacture functional prototypes and develop rapid tooling. The growth gained momentum with the entry of commercial entities such as EOS GmbH. SLS is used to manufacture 3D objects by using a variety of materials including wax, cermet, ceramics nylon-glass composites, metal-polymer powders, metals, alloys, steels, polymers, nylon, and carbonate [43], whereas DMLS solely uses metallic powders. Some of the most widely used materials for DMLS are Ti based alloys, Nickel based super alloys, Al based alloys, stainless steels (316L and 17-4PH), precious metals (Au, Ag), refractory metals (W, Ta), Cu based alloys, intermetallic and low alloy steels [44].

Laser sintering differs from the laser melting AM technologies mainly with the way it fuses the material powder. A high-temperature laser heats up the layers of fine powder until the temperature reaches a certain number below the melting point of the printing material. Hence, the laser sinters the spread powder to form the 3D object layer by layer and this process is repeated until the completion of the part. The final part is generally expected to be precise in shape and size, to have a controlled porosity and a high-density ratio (99.5+%) with excellent mechanical properties [45].

Apart from the many advantages LPBF offers, it also may introduce several disadvantages depending on different material powder and printing parameters. Such disadvantages include porosity, low strength etc. leading to bad mechanical properties, poor surface quality, geometry and dimension inaccuracy, residual stress, microstructural defects, and non-uniform temperature distribution [46]. Common defects in the SLS processes can be seen in the Fig 2.4.

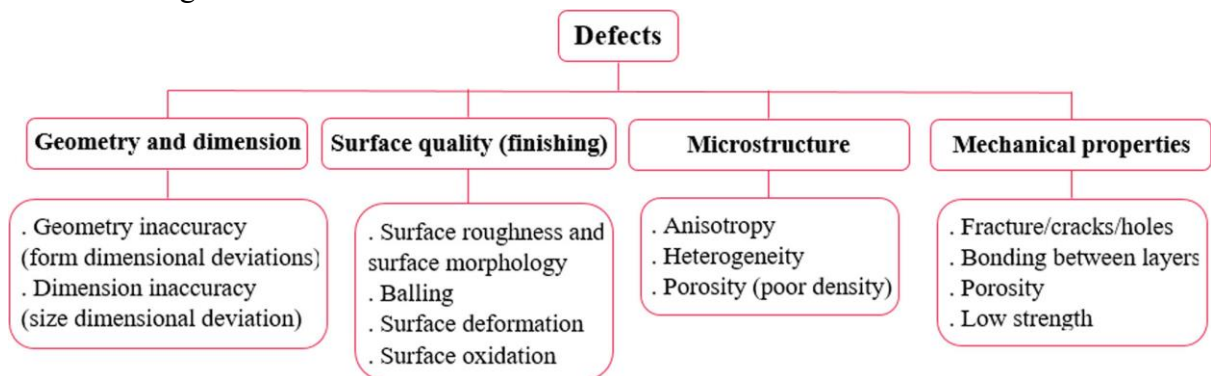


Figure 2. 4: Common defects in the SLS process [46]

Therefore, those process and powder parameters must be carefully controlled throughout the process to achieve excellent mechanical properties and high-density objects. The process and material parameters that affect the final part are input laser power, layer-thickness, scanning speed, hatch spacing, laser beam diameter, chemical composition, and particle size of the powder used [47] [48].

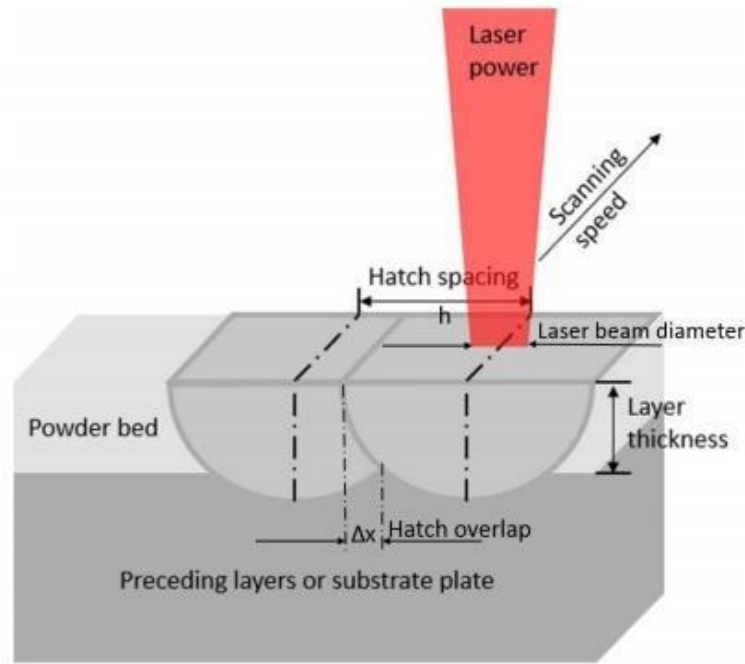


Figure 2. 5: Schematic diagram of process parameters of LPBF processes [49]

As the main concern of this work is porosity, the parameters affecting it can be seen in Fig. 2.5, and additionally to the figure; scan strategy, balling³, powder size, powder morphology are some of the parameters that affect the final part porosity. In the next subsections, how these parameters affect the porosity of the 3D part is explained.

2.1.2.1 Laser Specification:

Higher laser power and/or lower scan speeds cause less porosity in the object. The reason according to [46] is at higher laser powers and lower scan speeds, powders can absorb more energy, and this leads to an increase in sintering. Therefore, larger inter-agglomerate sintering necks⁴, which leads to less porosity generation, are formed. Fig. 2.6 shows the stages of sintering, and how larger sintering neck leads to lower porosity at the end. It underlines the importance of the laser power and scan speed parameters on the porosity formation.

³ Balling: is an issue that frequently occurs in SLS processes and severely affects the surface quality of sintered parts.

⁴ Sintering neck: is used to describe the junction connected by two powder particles.

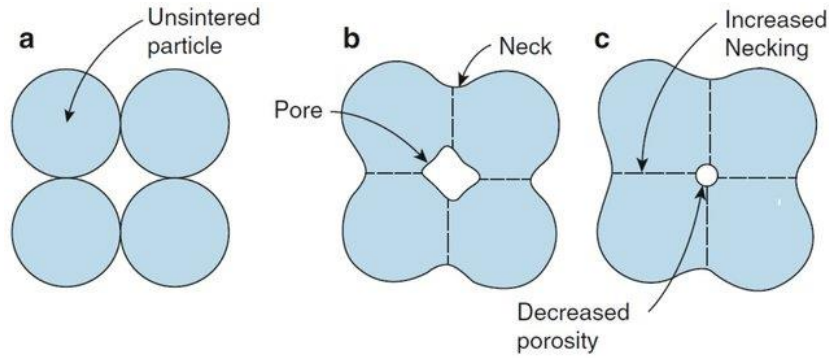


Figure 2. 6: Sintering neck process [50]

In the figure above, (a) represents packed particles before the sintering process starts, (b) particles agglomerate; creating necks to decrease the free surface areas, (c) increase the dimensions of the necks' sizes and consequent decrease of inner pores in the middle [51]. Sintering merges different particles at temperatures between half the melting point and melting point. The driving mechanism of the sintering process is the minimization of the total free energy. This initiates solid-state diffusion. Therefore, surface energy and surface area associated with it decrease.

Also, Gu D. et al in this research [52] showed in detail the correlation between the laser power and scan speed on the final part porosity. In order to find a suitable process window, they created this process map in Fig. 2.7 by using a wide range of laser power and scan speed combinations, as indicated by four sets of symbols, on a single layer of 316L stainless-steel powder to see the resulting sintering mechanism of a DMLS process. They found four different zones showing different behaviors on the resultant sintering structures, mainly affecting the porosity/density of the part's surface. Here it depicts that in Zone I, powder is unsintered and there is no sign of melting; in Zone II, the surface is sintered but has a porous structure; in Zone III, improved results but balling is present and there are coarsened metallic balls; in Zone IV, the part's surface is fully dense and complete. Laser power and scan speed combinations denoted by the same symbols exhibited a similar sintering mechanism.

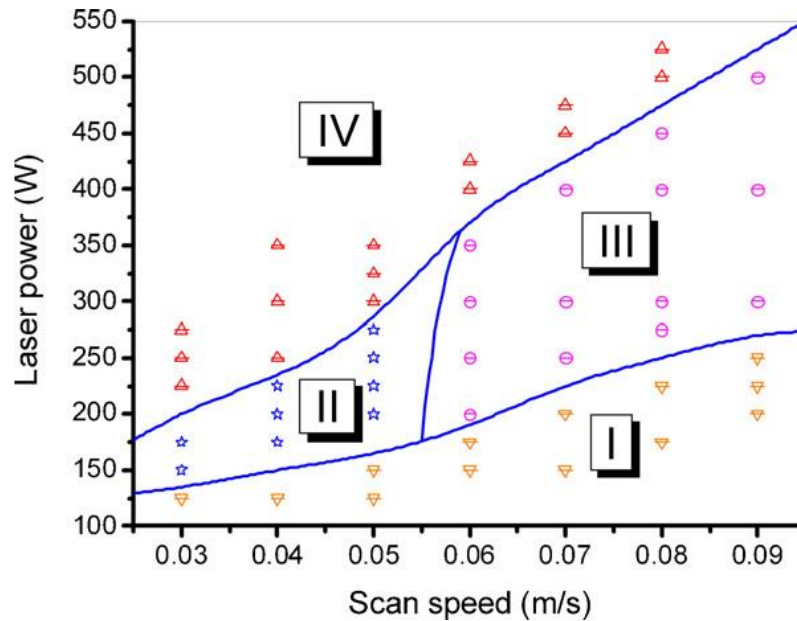


Figure 2. 7: Correlation between laser power and scan speed with porosity [52]

In addition to this research, even though it will be further included in the next sections, the porosity and surface quality we have found seem to be in accordance with this research as our final part quality lies in the Zone III of this process map with 305W and 1010 mm/s, laser power and scan speed, respectively.

Laser input energy density is another parameter that controls the porosity level. In fact, previous research found an optimum value for laser energy density in which the porosity level is at its minimum, around the bottom of the curve, as seen in Fig. 2.8. Numbers below the optimal energy density value cause discontinuous tracks with some gaps in between and generate balling. In contrast, numbers above the optimal value lead to changing the composition of the material and increasing surface tension, causing even bigger size balling (around $100 \mu m$) [46], [53].

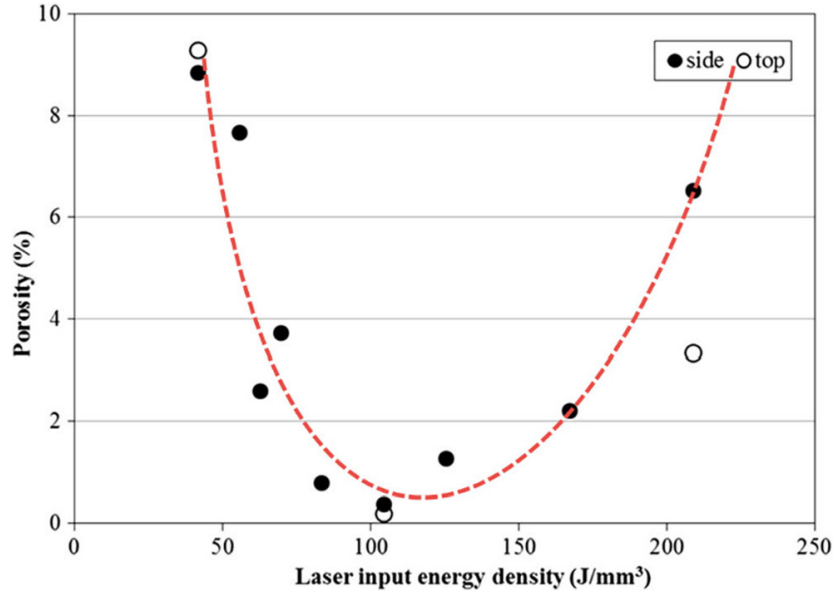


Figure 2. 8: Laser input energy density against porosity [46] [53]

The laser input energy density (Q) is a function of laser power, hatch space, layer thickness, point distance, and exposure time [53].

$$Q = \frac{\text{laser power} \left(\frac{\text{exposure time}}{\text{hatch space} \times \text{point distance}} \right)}{\text{layer thickness}} \quad (1)$$

The process parameters of our EOSINT M 280 Printer were obtained from the IPeG workshop and confirmed with the EOS technical catalogue as such laser power is 305 W, the layer thickness is $50 \mu\text{m}$, hatch space is $110 \mu\text{m}$. Exposure time and point distance are chosen to be $100 \mu\text{s}$ and $50 \mu\text{m}$, respectively as these numbers are the mean values from the experiment of the same research. Therefore, the laser input energy density of our printing configuration is found to be $Q \cong 110 \text{ J/mm}^3$ from Eq. 1. This value lies on the edge of the curve, meaning that the porosity dependence on the laser input energy density is at the minimum. Our micro-CT porosity analysis showing that the average density of our 3D parts is 99.97% is in good agreement with the correlation found in Fig. 2.8.

2.1.2.2 Layer Thickness:

Layer thickness is an important parameter that affect the porosity level. It is found by many researchers that when other process parameters kept constant, the porosity level tends to decrease as powder layer thickness decreases. The reason is found to be that lower powder layer thickness leads to a deeper laser penetration, resulting a better bonding between consecutive layers; hence, higher density and lower porosity components [52], [54], [55], [56]. Fig. 2.9 shows the tendency of the porosity percentage variation by the

change of powder layer thickness of SLS printed components. It is seen that higher layer thickness causes larger amounts of porosity due to insufficient laser penetration depth resulting in poor adhesion between the two consecutive layers [56].

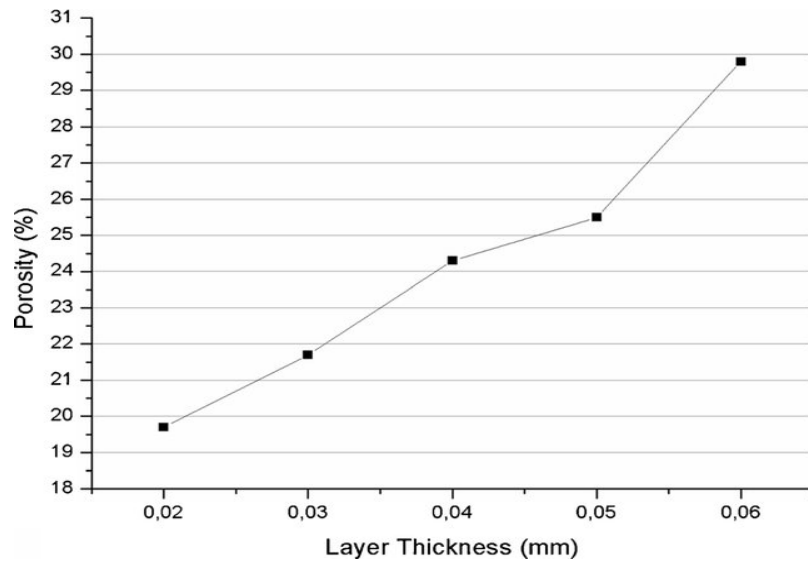


Figure 2. 9: Influence of layer thickness on porosity of SLS printed samples [56]

2.1.2.3 Hatch Space and Overlap:

Hatch space is the distance between the center lines of two consecutive laser scans [57]. Hatch space affects the printing speed. If it is high, it will take the laser less time to scan the layer. To have larger hatch space, larger laser spot size is required. Otherwise, a gap will form between two consecutive scans resulting in porous 3D objects [58]. A correlation between scan line spacing (hatch space) and porosity can be seen in Fig. 2.10.

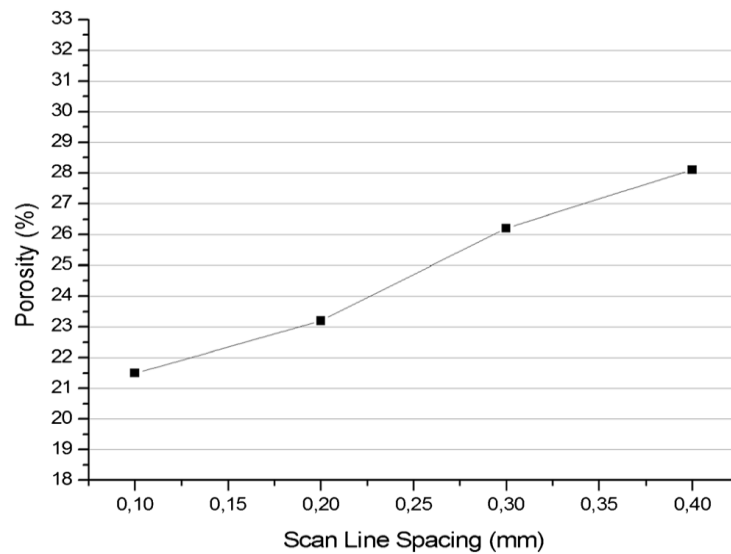


Figure 2. 10: Influence of hatch space on porosity of SLS printed samples [56]

Overlap is a necessary parameter to avoid porosity that may have been introduced at the boundaries of the powder particles. In a typical laser beam, the laser power is higher at the center than at the boundary. The result of this is when there is melting in the center, the boundary would still be heating. Hence, introducing some overlap will avoid this less heat generation at the boundary, and moreover inter-run porosity [46], [58].

2.1.2.4 Building Orientation

Many researchers have investigated the effect of building orientation on the porosity of AM parts. Different studies found some similar and some contradicting results on the impact of building orientation on the final part porosity. One research found in their experiment that horizontally built SLS specimens have higher fatigue strength despite having more elevated levels of porosity compared to the vertically built and 45° (with respect to the build plate during fabrication) oriented built specimens. This conclusion was attributed to horizontal specimens having smaller voids while vertical specimens containing lower porosity but larger voids causing higher stress concentrations formed during printing and such that the defects for these specimens were more damaging [59].

Also, Ziólkowski et al. [13] found that horizontally SLS printed samples resulted with higher porosity percentage when compared to 45° orientation and vertically printed samples: having 2.97%, 0.15%, and 1.61% volumetric porosity, respectively. In addition, they noted that the CT system that they used had a limitation such that it did not detect defects smaller than 70 μ m due to the voxel size of 37 μ m used during the reconstruction of the CT images. This constraint misled the global porosity ratio calculated for the vertically built specimen because it had many uniformly distributed smaller pores which were detected by the microscopic cross-sectional porosity measurement method. In fact, the porosity percentages found by the microscopic method are 2.58%, 0.14%, and 4.74%, respectively for the horizontal, 45°, and vertical specimens. Meaning, for the horizontal and 45° specimens, similar results were obtained but for the vertical one, the difference is significant between the two methods.

Malekipour et al. [46] reported an experimental result where five different building orientations, 0°, 30°, 45°, 60°, and 90°, respectively, were examined and it revealed that the 90° building orientation was resulted with the lowest amount of porosity among the other directions whereas 0° and 45° specimens were found to have the weakest compressive strength due to higher porosity ratios.

Consequently, most previous research stated that the vertical building orientation generates the least amount of porosity. However, despite this finding, the vertical building direction may trigger other defects (regardless of porosity) to initiate a fatigue crack (at least for SLM). In addition to that, an appropriate voxel size must be selected for the XCT method

to capture all the pores including the smaller ones to obtain correct porosity analysis results.

2.1.2.5 Powder Size

Larger size powder (usually bigger than 100 μm) requires higher laser energy density to make bonds between powder particles, causing an increase in porosity levels for a given energy density. Therefore, smaller powder induces less porosity [46], [52].

2.1.2.6 Powder Morphology

Powder particles with spherical morphology and fewer irregularities are found to form less porosity because of their better flowability and less surface contamination [46], [60].

2.1.2.7 Powder Apparent Density

Powder Apparent density -also named powder packing density- is determined by the ratio of the mass to a given volume of packed powder in a layer. Parameters that affect the apparent density are the powder size, shape, and size distribution. Also, how the powder is mixed affects the apparent density as mixing different-sized particles can enhance it. Zhu et al. [61] found that the final density of the DMLS printed parts is directly proportional to the apparent density of the powder. They used different apparent densities with varying process parameters and observed that the final part's density increased with the powder apparent density.

2.2. Fatigue

Fatigue phenomenon has been investigated by many researchers since 1830s when they observed failures of the conveyor chains which had been used under repetitive loading in the Clausthal mines in Germany. In 1837, the German mining administrator Julius Albert published the first fatigue test results from the machine that he invented for the failing conveyor chains in the mines [62], [63].

2.2.1 Wöhler Curve

With the development of industries and increasing use of metals in their applications, fatigue failures started to be more remarkable as they appear to happen more frequently and dangerous. Hence, after mid-19th century, a German engineer August Wöhler investigated the fatigue behavior of the axles of carriages for the railways. He performed torsion, bending, and axial fatigue tests under cyclic loading for those components. Wöhler himself depicted his test results in a table form but later, his successors used curves to describe the fatigue behavior which was later called S-N (cyclic stress against the cycles to failure) Curve or Wöhler Curve [63], [64]. Wöhler Curve describes the lower load levels as High Cycle Fatigue (HCF), and higher load levels as Low Cycle Fatigue (LCF) in which plastic strain has a relevant role in the latter and elastic stresses are present in the former. Hence, LCF regime is strain-controlled whereas HCF is stress-controlled.

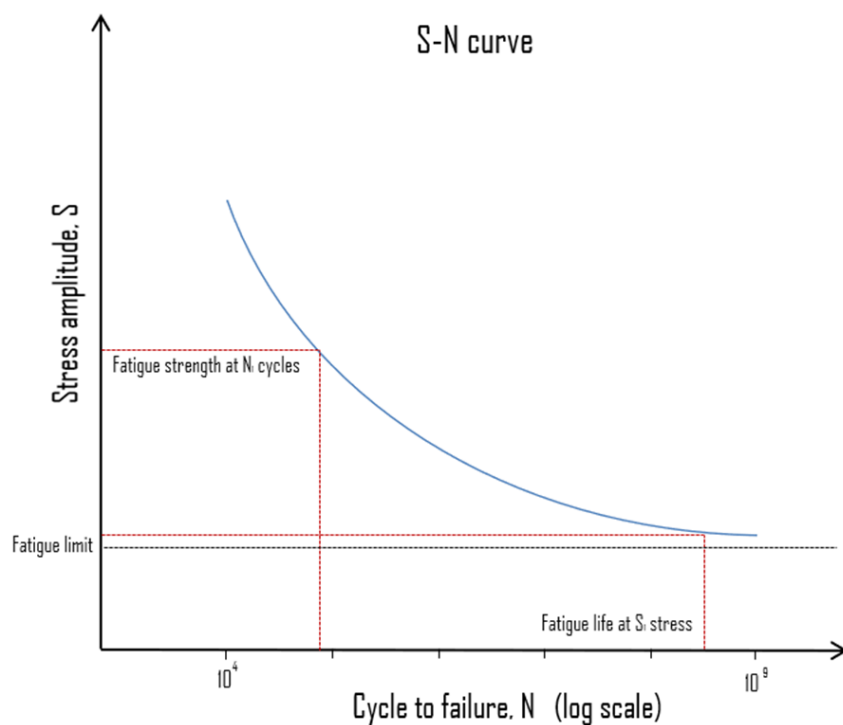


Figure 2. 11: Representative Wöhler/SN Curve [65]

2.2.2 Fatigue Life Prediction

Basquin described the finite life region of the S-N curve that lies in the HCF regime, which is between 10^3 or 10^4 and 10^6 or 10^7 number of cycles, depending on the material type. He represented the curve in the form of log-log coordinates in which $\log \sigma_a$ on the ordinate and $\log N$ on the abscissa and found the following formula eq. (2) which we still use today:

$$N \cdot \sigma_a^k = A \quad (2)$$

Where σ_a is alternating stress amplitude, N is the number of cycles to failure, k and A are material coefficient and constant respectively at given conditions. This curve is represented in logarithm scale by a straight line instead of the blue line that is in the Fig. 2.11. The equation of the straight-line eq. (3) can be found as,

$$\log(\sigma_a) = -\frac{1}{k}\log(N) + \frac{1}{k}\log(A) \quad (3)$$

Typically for steel and aluminum, with this formula of Basquin Model, one can build a simplified Wöhler Curve by using the σ_a and N at the transition points of the curve for HCF region ($N = 10^{3\sim 4}$ and $N' = 10^{7\sim 8}$ for the number of cycles, $\sigma_a = 0.9 \cdot R_m$ and G_D : endurance limit) if the tensile strength and the endurance limit of the material are already known beforehand. However, for materials with unknown endurance limit and tensile strength, a proper fatigue test procedure must be followed to build the S-N curve. Usually, between 15 and 25 samples are enough for determining a full S-N curve although the reliability of the test results increases with the number of tests [66]. There are different standards and methods suggesting different numbers of specimens for building the curve. This number is related to the probability of failure and confidence level of different applications. According to the ISO 12107 Standard, for tests to obtain the fatigue limit, a set of seven specimens is recommended whereas for fatigue testing to obtain the S-N curve, a minimum of eight specimens is suggested in which two specimens be tested at each four different stress levels.

2.2.3 Cyclic Loading in Fatigue Testing

During fatigue testing, tests specimens are subjected to cyclic (or alternating) loads. These loads are defined by either a stress range ($\Delta\sigma$ or σ_r) or a stress amplitude (σ_a). The stress range is defined as the difference between the maximum stress (σ_{\max}) and minimum stress (σ_{\min}) in one loading cycle [67]. Eq. (4) shows the stress range.

$$\Delta\sigma = \sigma_{\max} - \sigma_{\min} \quad (4)$$

The stress amplitude is defined as half of the stress range or half of the difference between the maximum and minimum stress, and it always has a positive value. Eq. (5) demonstrates the stress amplitude.

$$\sigma_a = \frac{\Delta\sigma}{2} = \frac{\sigma_{\max} - \sigma_{\min}}{2} \quad (5)$$

Usually, components in real life are subjected to cyclic loads together with a mean stress (σ_m). Most of the time, fatigue tests that aim to build an S-N/Wöhler Curve use fully reversed loading. Fully reversed means the mean stress is zero throughout the fatigue testing. In this case, σ_{\max} and σ_{\min} are equal in absolute value.

$$\sigma_m = \frac{\sigma_{\max} + \sigma_{\min}}{2} \quad (6)$$

Stress ratio (R) is often used as a representation of the mean stress applied to the test piece and it is among the most important parameters in cyclic loading case. Stress ratio is defined as the ratio between the minimum stress and maximum stress in a cycle.

$$R = \frac{\sigma_{\min}}{\sigma_{\max}} \quad (7)$$

In case of a fully reversed cycle, the stress ratio is $R = -1$. When the cyclic load is repeated which means it is applied and then removed, the stress ratio is $R = 0$. There are also other cases in which the stress is fluctuating, and stress ratio has values like $R = 0.1$. Fig. 2.12 shows these cases graphically.

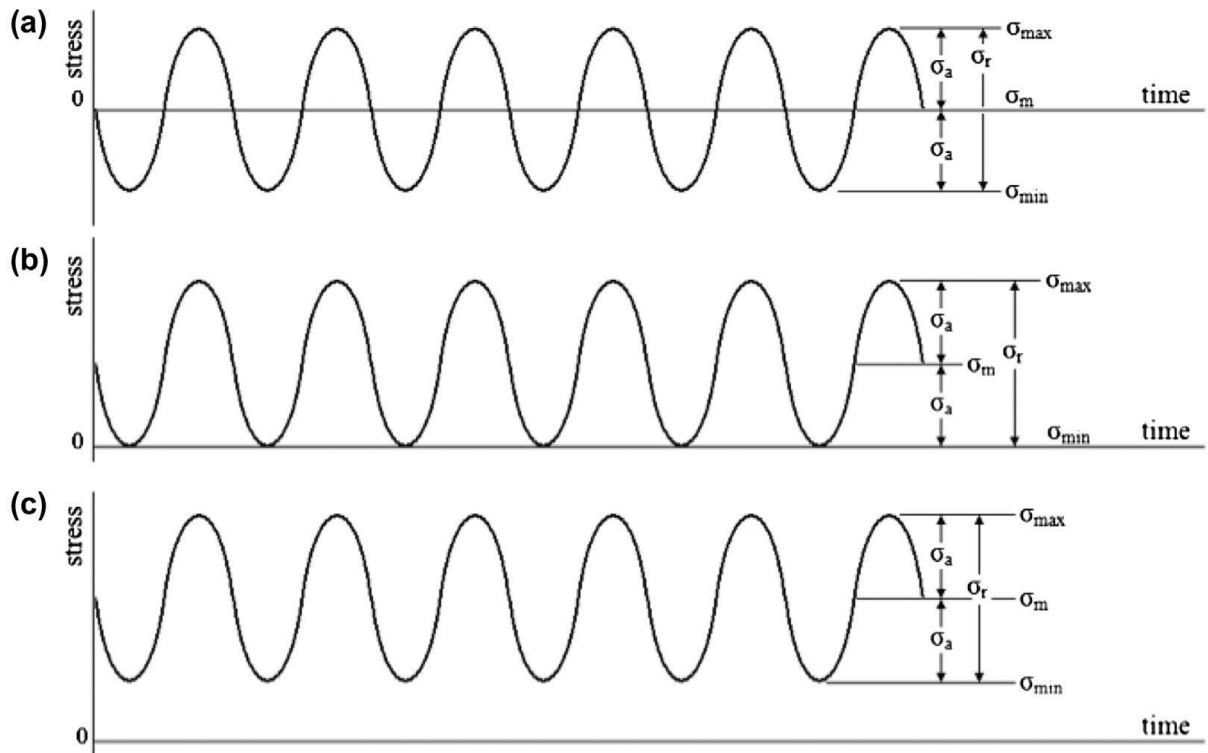


Figure 2. 12: Examples of (a) fully reversed sinusoidal loading, (b) repeated stress, and (c) fluctuating stress [68]

2.2.3 Fatigue Beach Marks

It is possible to recognize the fatigue failure by inspecting the rupture surface of a material. Some peculiarities of the broken section will expose that the damage done was caused by cyclic loading. Some rounded marks and radial lines on the broken section allow us to detect the initiation and progressive propagation of the fatigue crack. Their shape makes it possible to detect the crack nucleation [69].

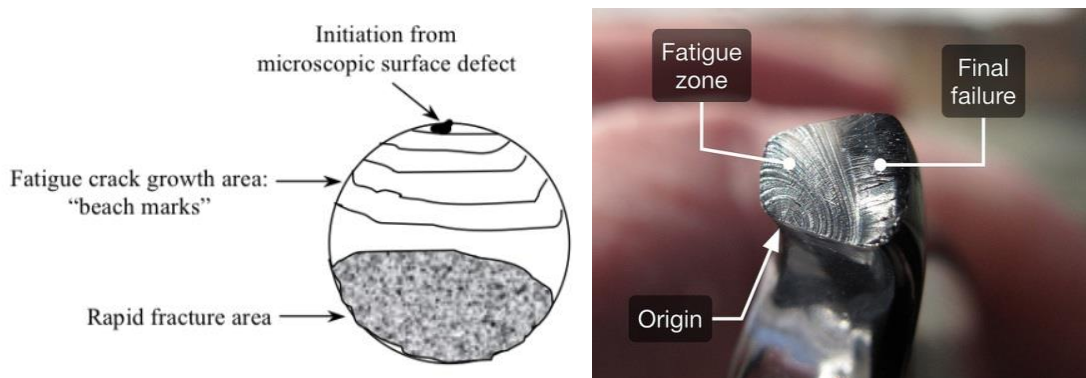


Figure 2. 13: Beach marks showing the fatigue crack initiation, nucleation, and final fracture [70]

Fig. 2.13 shows how beach marks help recognize the loads that caused the fatigue crack initiation, nucleation, and final fracture. It is also possible to distinguish between the high and low loads depending on the shapes of the beach marks they caused as in Fig. 2.14. Generally, higher loads induce fewer number of beach marks, but a large area of evident forced final fracture is visible. On the contrary, lower loads cause many beach marks until the final fatigue fracture happens [71].

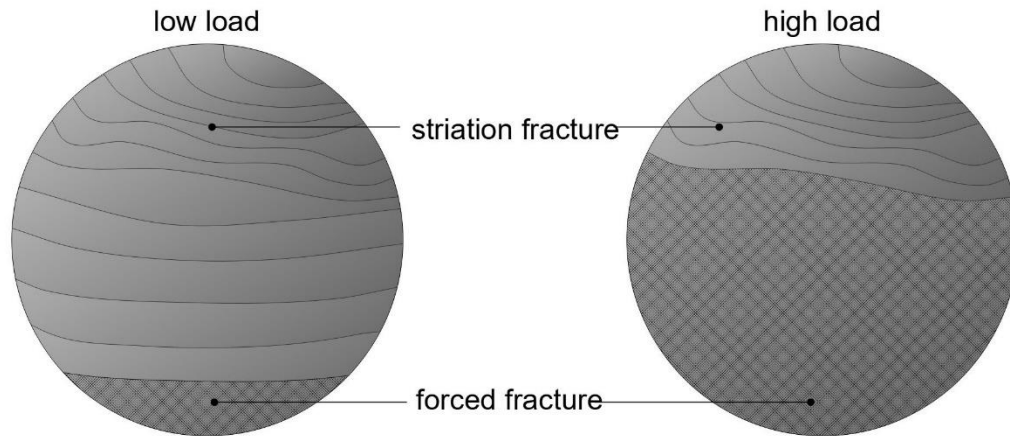


Figure 2. 14: Beach marks caused by different magnitudes of loads [71]

2.3. X-ray Computed Tomography

X-ray computed tomography (XCT) can display the internal structure and possible defects of objects in detail in 3D non-destructively. It is widely used in medical and heavy industry as well as in engineering and science applications nowadays. Considering X-ray CT applications across the engineering, materials, manufacturing, metrology, food, biological and paleontological sciences are becoming more prominent lately [72].

CT takes 2D radiographic images and exploits them for computationally reconstructing 3D images and segmenting these 3D images for subsequent visualization and quantification. The application of high-resolution X-ray CT across engineering solutions is a very useful and fast tool to examine the structural evolution of materials in 3D in real time or in a time-lapse manner. It allows us to evaluate the final quality of our component and give a lead to further improving of the part [72]. Unlike other common methods such as SEM which is not capable of analyzing the whole object without cutting it into several layers, CT can scan any surface, shape, color, or material up to a certain density and thickness penetrable by X-rays [73].

The origin of X-ray CT technology is based on the Radon transform⁵ which was introduced by Johann Radon in 1917 [74]. The basic working principle of X-ray CT technology is to obtain the radiation attenuation information when X-ray passes through the sample at different directions. Basically, X-ray CT forms 3D representations of an object by taking many X-ray images around an axis of rotation and using algorithms to reconstruct a 3D model [75]. Fig 2.15 shows a representation of how an X-ray CT device works. The figure shows that some radial projections are captured at different angles on a sample by the X-ray to obtain 2D slice images. These projections are taken by rotating the object in small increments, and the process is repeated until complete data is acquired from a 360° rotation. Hence, a 3D image is being produced by reconstructing scanned numerous slice images of the sample.

X-ray is generated by a speeding electron impact on a sample, where the energy of X-ray photon is equal to the total kinetic energy of the electron. X-ray photon energy E can be defined as follows:

$$E = hv = \frac{hc}{\lambda} \quad (8)$$

⁵ The Radon transform is an integral transform whose inverse is used to reconstruct images from medical CT scans [102].

The unit used for E is eV and $1 eV = 1.62 \cdot 10^{-34} J$. Most X-rays have a wavelength ranging from 0.1 nm to 0.01 nm corresponding to energies in the range of 10 eV to 450 keV [74].

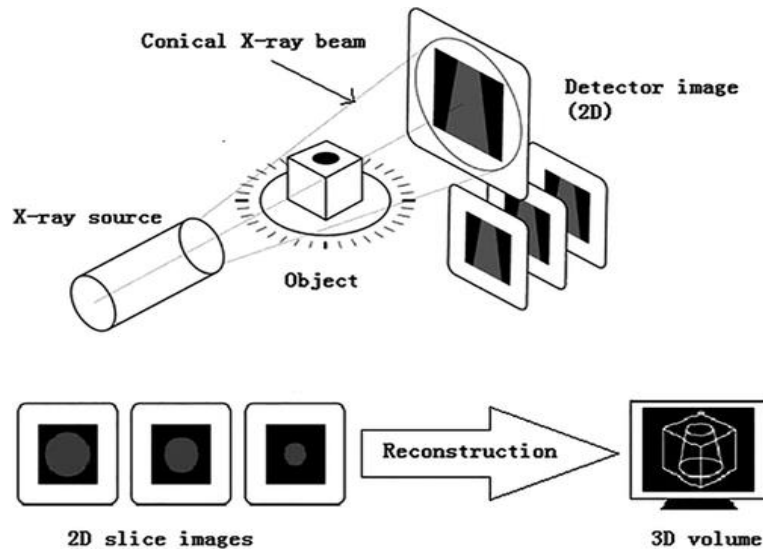


Figure 2. 15: Working principle of X-ray CT technology [74]

In traditional CT processes, an X-ray tube (X-ray source) rotates around a sample and then the attenuation is recorded on a detector. X-ray tubes come in a variety of types and different source voltage powers. A simple X-ray tube consists of a filament (cathode), which generates thermal electrons, and an anode, which generates X-rays when electrons collide, fixed in a tube, and vacuumed. Fig. 2.16 shows a schematic and representative picture of an X-ray tube. Many of these tubes are relatively small and are used at voltages ranging from 10 kV to 130 kV [74], [76].

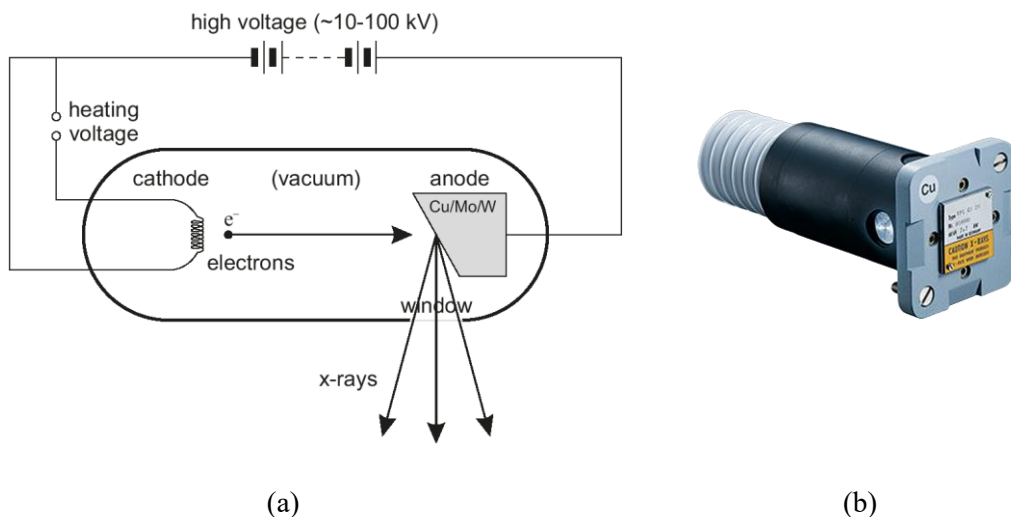


Figure 2. 16: X-ray tube (a) an X-ray tube schematic [77], (b) Bruker metal-ceramic sealed tube [78]

X-ray sources use filters for different applications depending on the energy need. One of the most common practical methods in XCT is physical filtration. This method is applied by placing a filter where the X-ray is supposed to come out. This filtration allows the low energy X-rays to be absorbed by the filter placed and lets the high energy X-rays to pass through the sample. Therefore, the use of a filter reduces the noise and makes sure to produce a clearer image by this absorption. Common materials used for filters are Copper (Cu), Iron (Fe), Aluminum (Al), Tungsten (W), and some other high atomic number materials [79], [80]. For small samples and for the samples with very low absorption, the scanning can be done without the filters. For dense or large samples, the use of filters is recommended [81].

Once, all the 2D images are collected, the data are processed by a computer software that can perform the reconstruction process of the acquired 2D images to create a 3D model. Then, the 3D reconstruction can be used for a variety of applications such as defect or porosity analysis, measurement of geometries, creating an STL file, etc. [75].

Lately, XCT technology is also widely used in AM. It has been used in AM for the first time in a medical manner to study a model of a skull in 1990 [82]. After this first experience, many developments have been made. From 2005 on, the use of XCT has been increasing for measurement of AM parts, specifically as a pore measurement instrument. Between then and now, many researchers studied and compared XCT with other methods for porosity measurements such as SEM and Archimedes method. Among these methods, Archimedes method is found to be the most accurate and precise one although it was reported that the porosity results are systematically higher than of XCT's [83]. However, Archimedes method is not capable of giving any information about the internal part geometry beyond an overall porosity. Hence, XCT is a better option for dimensional pore measurement and internal defect detection. In addition to the measurement of pore morphology, XCT also allows visualization of pore distribution within parts [75], [83], [84], [85]. As of now, XCT is used as a well-trusted technique to quantify and analyze the porosity of parts, specifically AM manufactured parts.

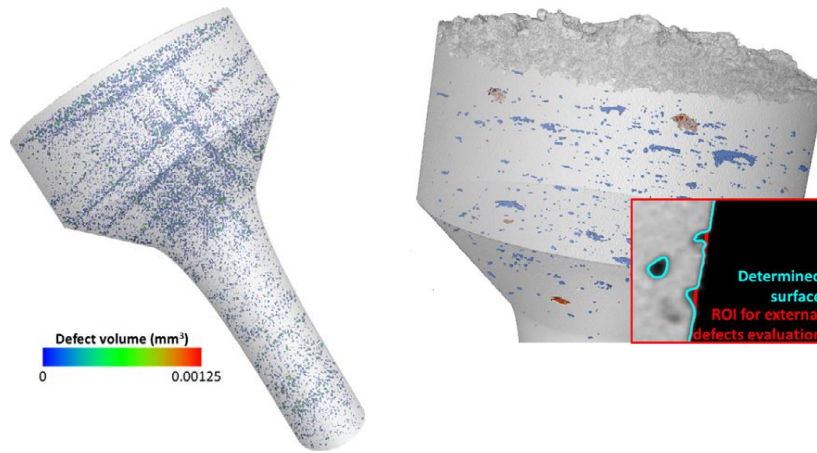


Figure 2. 17: Two 3D CT constructed volumes showing the porosity/defects [86]

Fig. 2.17 shows two 3D models constructed by CT for porosity analysis. On the picture to right side, the blue colored defects are the internal pores and others are the external surface pores. The picture to the left represents a typical spiral staircase porosity distribution due to hatching errors in the 3D printing process. As seen from the above figure, these kind of visualizations and whole geometry porosity analyses are possible with CT unlike other porosity quantification techniques.

3. METHODS

3.1. Research Problem

The main concern of this research is investigating the effect of porosity caused by the LPBF processes on the fatigue behavior of additively manufactured metal parts. According to the literature, higher amount of porosity causes a decreased fatigue life of components. Especially, pores on the surface and near the surface are the most detrimental ones that may initiate and propagate the crack caused by the cyclic loading and consequently, lead to the final fracture of the part.

The uncertainty of the printing process causes variations in the porosity levels of the printed parts. This leads to different fatigue behavior for the identical specimens manufactured by the same LPBF machine. This stochastic process can be modelled with a statistical correlation between the amount and/or location of porosity and fatigue life of the printed specimens. From here, the statistical model developed may be used for the larger parts in which measuring the porosity is not possible with standard non-destructive methods.

The expectation of this work is that the fatigue lives are significantly lower for the samples with a higher amount of porosity and possessing more pores on the surface and sub-surface area. Therefore, a statistical model can be derived based on the XCT measurements and printed samples.

To validate this hypothesis, a non-destructive material inspection method, 3D X-ray Computed Tomography (3D XCT) was used to analyze the specimens for porosity. With these measurements noted, torsion fatigue tests were applied to the samples to find the fatigue lives. With this information, coherence was sought between the XCT scans and the model's fatigue behavior.

3.2 Previous Research

There are several common non-destructive material inspection methods in the literature to analyze the porosity of a given part. Scanning Electron Microscope (SEM) and XCT are two common techniques. SEM allows gathering information about the surface features and composition of a sample as it scans a focused electron beam over a surface to create an image. Although SEM images look very three-dimensional, SEM is not capable of analyzing the whole 3D printed sample without cutting it into several layers [87]. On the other hand, XCT can analyze the full volume for porosity without giving any damage to the structure.

Researchers used XCT and fatigue testing to validate their hypotheses. Koch et al. [88] examined the specimens by XCT before fatigue testing for defect analysis. To ensure the comparability of the results, they used the same scanning parameters to analyze every specimen. For the fatigue tests, they used a stress ratio of $R = -1$ with a test frequency of 10 Hz. They considered specimens which exceeded $N_f = 2 \cdot 10^6$ cycles as run outs in the fatigue tests. The specimen geometry used was of an hourglass type of fatigue testing specimen which is suitable for their tension-compression fatigue tests.

Another research conducted by Szalva et al [89] aimed to develop a relationship between the XCT results and fatigue failure for their specimens. XCT was used prior to the fatigue tests for porosity analysis. They chose four different stress levels for the fatigue tests with two different stress ratios fully reversed $R = -1$ and pulsating load $R = 0.1$ at 20 Hz frequency, for a total of twenty specimens each. They stopped the fatigue tests after $N_f = 2 \cdot 10^6$ cycles even though the specimens aren't failed. The fatigue tests are load-controlled which means that they are within the HCF regime. They found out that the specimens that failed by porosity, the cracks were initiated from the pores that were close to the surface instead of the ones at surface. They also classified the types of porosity defects such as gas porosity, shrinkage porosity, etc. that caused the fatigue failure. However, this is not the concern of this master's thesis.

Also, Plessis et al. [16] published a review paper in which they gathered different research where XCT scanning was exploited for the LPBF printed parts to investigate the effects of porosity on mechanical properties, especially on fatigue properties. Brandão et al. [90] investigated AlSi10Mg LPBF produced parts using XCT and fatigue tests. Due to process parameters variation, some samples exhibited total porosity levels around 0.4-0.8% whereas others were found around $<0.05\%$. Furthermore, they used two types of test specimens: machined and in as-built condition. They concluded that the poor surface roughness of the as-built specimens resulted in poor fatigue properties regardless of the porosity levels found. This outcome points out the importance of surface roughness on fatigue behavior. Machined specimens that have been resulted in poor fatigue properties are the ones with the porosity levels around 0.4-0.8% due to the lack-of-fusion defects caused by the process parameters variation. The best fatigue results achieved by the machined specimens that have low porosity levels. Liu et al. [91] indicated that the pores located just under the surface caused the fatigue crack initiation even though the total porosity levels are as low as 0.02%. Fig. 3.1 shows an XCT analysis prior to the fatigue test of the LPBF produced Ti6Al4V parts where the fracture surface was analyzed, and the crack initiating "killer pore" was identified. The crack initiating pore was the one near surface and larger than the other ones in the 2 mm near the failure location.

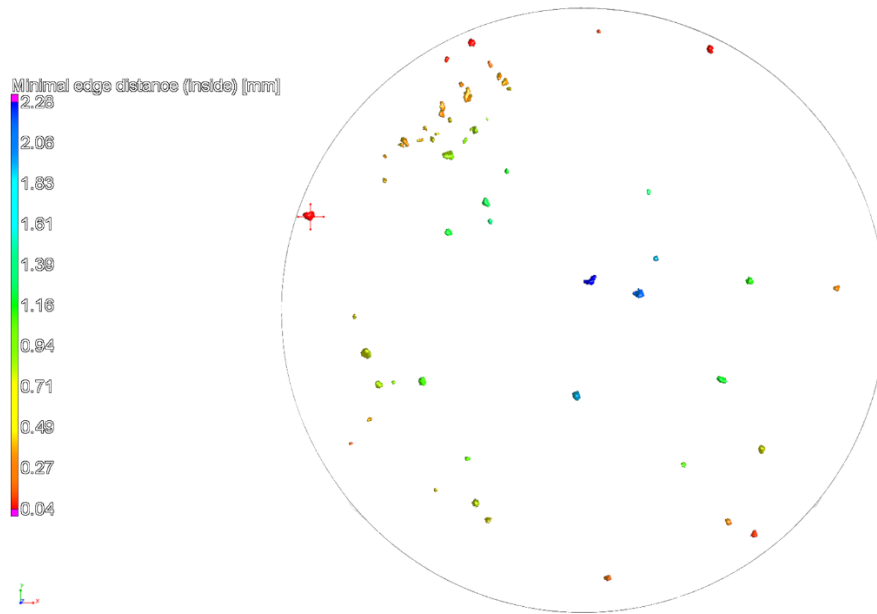


Figure 3. 1: Fracture surface analysis and X-ray tomography prior to fatigue tests, allowing visualization of all pores in region of failure – highlighting the “killer pore” [91]

A recent work by Andreau et al. [92] showed the importance of near-surface pores as critical points that can initiate the fatigue induced cracks. Fatigue test samples were produced with high density contours and porous interiors using modified process parameters that lead to lack-of-fusion pores. In HCF regime, crack initiation was observed on the pores within 0.1 mm of the surface although higher values of porosity and much larger pores found towards the interiors of the specimens.

Moreover, models about the prediction of fatigue lives based on the porosity data by XCT: Zhao et al. [93] developed a statistical analysis from the CT data for the prediction of fatigue properties. Fatigue lives were predicted based on the average pore size and it was concluded that fatigue life decreases with an increase in pore size. Romano et al. [94] conducted research in which LBPf produced parts were analyzed by XCT and fatigue tested for the HCF and LCF regimes. Their statistical analysis found that it is possible to predict the fatigue limit of the material by the XCT data. They developed a method to predict the fatigue limit of a homogenous volume of material without the need of a full volumetric XCT scan. They used witness specimens⁶ for the XCT scans and fatigue behavior prediction was successfully achieved.

⁶ Witness specimen is a sacrificial test piece of a material which allows testing without handling the actual part.

3.3 Experimental Methodology

The beginning point of this research would be to start the printing process as soon as possible. Therefore, an appropriate 3D geometry must be designed. To do that, the type of fatigue testing must be decided beforehand because different specimen geometries exist for different types of fatigue tests. Hence, starting from the selection of fatigue testing, specimen geometry, LPBF printing details, CT scans, fatigue testing procedures, and other methods used will be explained in the following chapters. Fig. 3.2 shows the steps followed for the methodological approach.



Figure 3. 2: Methodological approach steps

3.2.1 Fatigue Testing Bench

The available test benches that can apply dynamic loading on the specimens in the IPeG institute were a bending fatigue test machine and a torsional fatigue test machine. Prior to the beginning of the print job, both machines were investigated to understand which test bench is more suitable for our purpose to conduct proper fatigue testing and that is mostly in compliance with the existing standards for fatigue testing. Further investigation found that the bending test bench diverges from the DIN⁷ Standard for the rotary bending tests of metallic materials (DIN 50113). DIN suggests two types of applications for bending loading for rotary test benches as can be seen in Fig. 3.3.

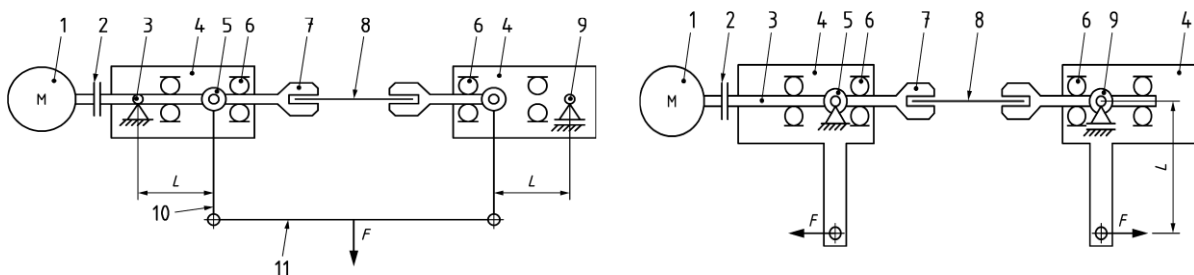


Figure 3. 3: Standard rotary bending fatigue testing machine setups according to DIN 50113

In the contrary of Fig. 3.1, the bending test bench at IPeG was designed to apply the bending load by providing a small tilting angle that gives the testing specimen a tiny eccentricity. This is not only following the standard fatigue testing procedure but also

⁷ DIN: Deutsches Institut für Normung, German Institute for Standardization

difficult to apply the same amount of force (N) every time when a new specimen is loaded on the test bench. Therefore, despite the vast usage of rotary bending fatigue testing and many available data in the literature, this testing machine wasn't easy to operate when compared to the torsion test bench.

On the other hand, the torsional fatigue testing bench was in good agreement with the ISO 1352 Standard except a few variations on the gripping adaptors which basically have the same functionality. It should be noted that no DIN or other institution's standards that is used today are found in the literature due to the fact that torsional fatigue testing is not commonly used among the researchers when compared to rotating bending and tension-compression fatigue tests. Fig. 3.4 simply represents the torsion testing mechanism proposed by the ISO standard.

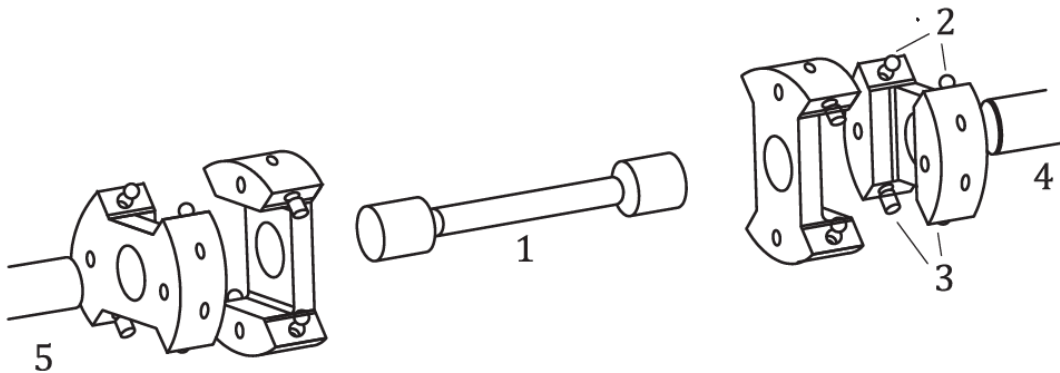


Figure 3. 4: Example of Morrison torsion grip in compliance with ISO 1352 [95]

The procedure for torsion testing is rather simple. The testing machine shall apply a clockwise and anticlockwise torsional loading and should have the capability to start smoothly as well as no backlash when passing through zero. It should be capable of controlling and measuring torque/position (degree) when the recommended wave cycle is applied. The specimen should not be constrained axially to prevent irrelevant forces from being introduced. The gripping system must transmit the cyclic loading to the specimen without backlash along its circumferential axis during the fatigue testing. The grips must also ensure an easy and repeatable assembly of themselves and the specimens every time another fatigue test wanted to be conducted. According to the ISO guidelines, collet, chuck style, socket style, wedge or Morrison grips can be chosen appropriately for the specimen ends. To qualify these mentioned features, a custom adaptor was designed to hold the specimen since the existing gripping system wasn't qualified for the fatigue testing standard. Obviously, before designing the adaptors, the specimen geometry had to be chosen.

3.2.2 Specimen Material

The material 1.2709 / X3Ni-CoMoTi 18-9-5 is optimized for producing additive manufacturing components using LPBF technology. It is an ultra-high-strength tooling grade maraging steel that is used for transmission shafts, aircraft landing gears, motorsport components, rocket motors, tools, automotive industry, etc. However, a FeNiCo-based powder material Oerlikon MetcoAdd C300-A which is similar to 18 Ni maraging steel (M300 type) was used in our LPBF printer. The chemical composition is similar to 1.2709 / X3Ni-CoMoTi 18-9-5. Material data from the manufacturer can be seen in the tables below.

Product	Weight Percent (nominal)					
	Fe	Ni	Co	Mo	Ti	C
MetcoAdd C300-A	Balance	17.0 – 19.0	8.0 – 10.0	4.5 – 5.5	0.8 – 1.2	< 0.03

Table 3. 1: Chemical composition of MetcoAdd C300-A

Product	Nominal Range [μm]	D90 [μm]	D50 [μm]	D10 [μm]	Hall Flow [s/50 g]
MetcoAdd C300-A	-45 +15	42 – 54	30 – 38	18 – 25	< 18

Table 3. 2: Particle size distribution and hall flow of MetcoAdd C300-A

Quick Facts	
Classification	Alloy, Fe-based
Chemistry	Fe 18Ni 9Co 5Mo 1Ti
Manufacture	Gas atomized (Argon)
Morphology	Spheroidal
Apparent Density	4 to 4.2 g/cm ³ (typical)
Solidus	1450 ± 10 °C (2641 ± 18 °F)
Liquidus	1490 ± 10 °C (2691 ± 18 °F)
Purpose	Additive Manufacturing
Process	Laser Powder Bed Fusion (PBF-LB)

Table 3. 3: Material specifications of MetcoAdd C300-A

Specification		Concept Laser M2 Cusing	EOS M290
Ultimate Tensile Strength (MPa), XY/Z		2064 ± 25 / 2104 ± 15	2050 ± 17 / 2027 ± 9
Yield Strength (MPa), XY/Z	ASTM E8	1982 ± 30 / 2023 ± 15	1996 ± 18 / 1980 ± 7
Elongation at break %, XY/Z		5 ± 2 / 5 ± 3	9 ± 1 / 8 ± 1
Hardness (VHN ₃₀₀)	ASTM E384-17	594 ± 15	599 ± 10
Relative Density %	Internal Specification	> 99.9	> 99.8

Table 3. 4: Typical post heat treatment properties of MetcoAdd C300-A

To obtain such high ultimate tensile strength and yield strength as shown in Table 3.4, a heat treatment procedure must be done. Therefore, the torsion test specimens after the printing have undergone an aging heat treatment process at 490°C for 6 hours.

3.2.3 Specimen Geometry

A proper specimen geometry for the torsion fatigue testing was chosen according to the ISO 1352. Generally, there are many types of specimen geometries for this kind of rotary destructive material test. However, ISO suggests two types of geometries depending on the goals of the test. One type is a tubular cross-section, and the other is a circular cross-section specimen. Tubular one is rather complex than the latter since there are a few details that might complicate the geometry such as the possibility of bending or buckling, wall thickness effects, surface finish issues in the interiors, and different definitions of failures [96]. Since our goal in this experiment is not only to conduct a proper fatigue test but also to see the effect of porosity on it, the circular cross-section type of specimen was chosen for our specimen geometry.

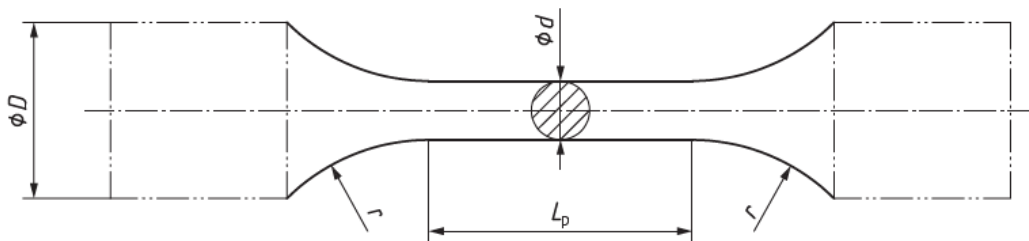


Figure 3. 5: Specimen with circular cross-section

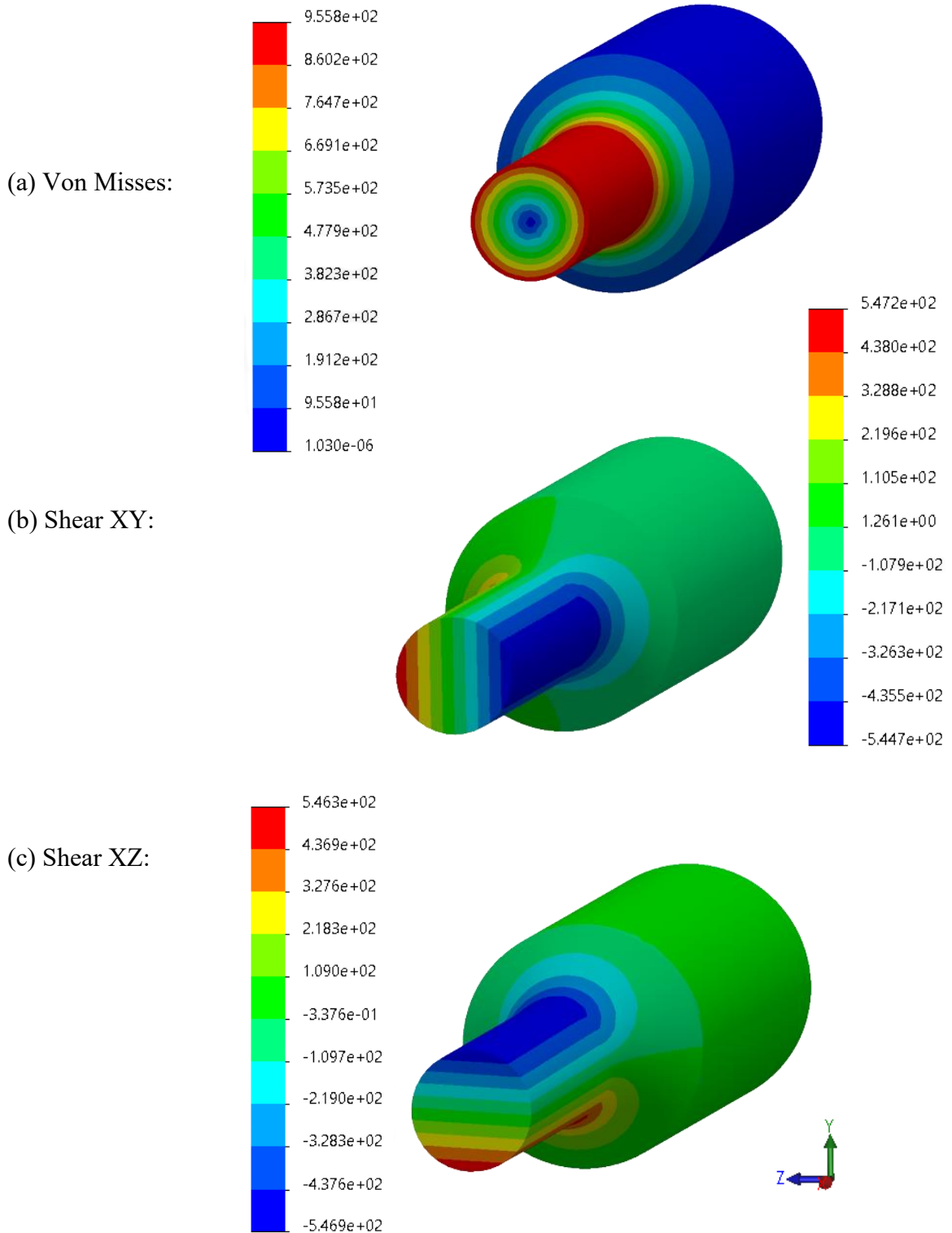
There are different considerations and limitations about the circular cross-section geometry as can be seen in Fig. 3.5, such as the outer diameter (D), gauge section diameter (d) and length (L_p), transition radius (r), and tolerances. Also, a proper specimen end must be chosen considering the type of gripping system used. Among many typical specimen ends, a circular specimens end was chosen as in Fig. 3.6.



Figure 3. 6: Circular specimen end

After deciding on the specimen shape, now dimensions shall be given according to the recommendations of the standard. Each of these dimensions shall be in a suggested range. Once all the dimensions were given, the adaptor for the gripping system can be designed. Different considerations have been made for the specimen dimensions in the given range to eliminate the stress concentration factors that may have been introduced if the geometry wasn't designed properly. Hence, after creating the specimen CAD model, static analysis

was done to expose where the maximum and minimum stresses occur and understand where the critical regions are in case of a high torque applied.



Diameter of cylindrical parallel length	$d = 4 \text{ mm}$
Parallel length	$L_p = 18 \text{ mm}$
Transition radius (from parallel section to grip end)	$r = 10 \text{ mm}$
External diameter (grip end)	$D = 8 \text{ mm}$
The tolerance on d	$\pm 0.05 \text{ mm}$

Table 3. 5: Dimensions chosen for the specimen

Fig. 3.7 shows the stress contours in the case of a pure shear loading caused by a torque of 6.75 Nm on the torsion specimen. It confirms the theoretical knowledge about the stresses due to torque on a circular cross-section in which stress is at maximum at the outer surface and decreased towards the center. The simulation also revealed whether a stress concentration is present outside the gauge section. As can be seen in Fig 3.8 the maximum and minimum shear stresses are occurring in the gauge section just after the transition section, which means the specimen geometry dimensions were given properly so that unnecessary stress concentrations are avoided.

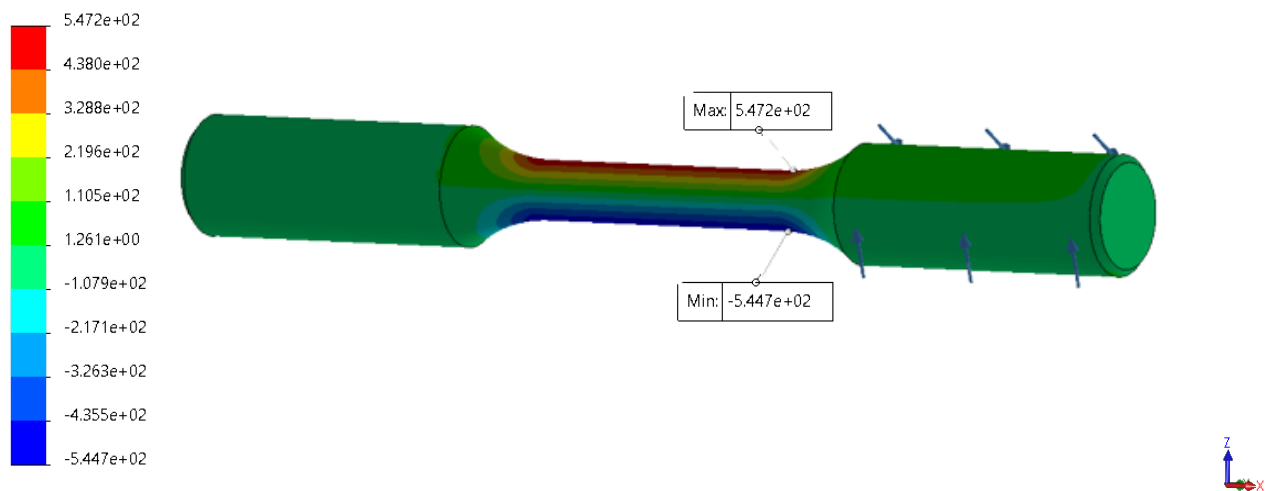


Figure 3. 8: Maximum and minimum shear stresses

3.2.4 Surface Treatment

Specimens after the 3D printing process have a very rough surface for fatigue testing. To minimize the surface roughness effect on the fatigue strength of the test samples, a surface treatment process was done by a rotary surface grinding machine that is available at the IPeG workshop (Fig. 3.9). The specimens (after the proper heat treatment process) were put inside the turning chamber that is full of vibrating small pieces touching the printed objects to remove excessive material on the surface for a better surface finish. The specimens were left inside the grinding machine for 28 hours until a better surface finish was achieved compared to the former state after the printing process.



Figure 3. 9: Rotary surface grinding machine

Fig. 3.10 shows the samples before the surface treatment process. The difference in the appearance between the surface treated samples and as-built ones can be noticed in the figure.



Figure 3. 10: As built specimens and a surface grinded specimen mounted on the machine

3.2.5 Torsion Fatigue Test Machine

The torsion fatigue test rig was initially constructed by IPeG to apply high cyclic loads to experimentally characterize the fatigue behavior of a torsion spring that is to be used in deep drilling technology for the industry. After defining our torsion test specimen shape and dimensions, the machine is adjusted for our purpose by designing a modified adaptor to clamp the specimen. The machine must have enough torsional stiffness, a motor that can apply adequate torque and has torsional loading capability for clockwise/counterclockwise motion, ensured correct alignment of the specimen, and a properly working cycle counter. It shall be capable of controlling and measuring the torque and/or degree of twist.

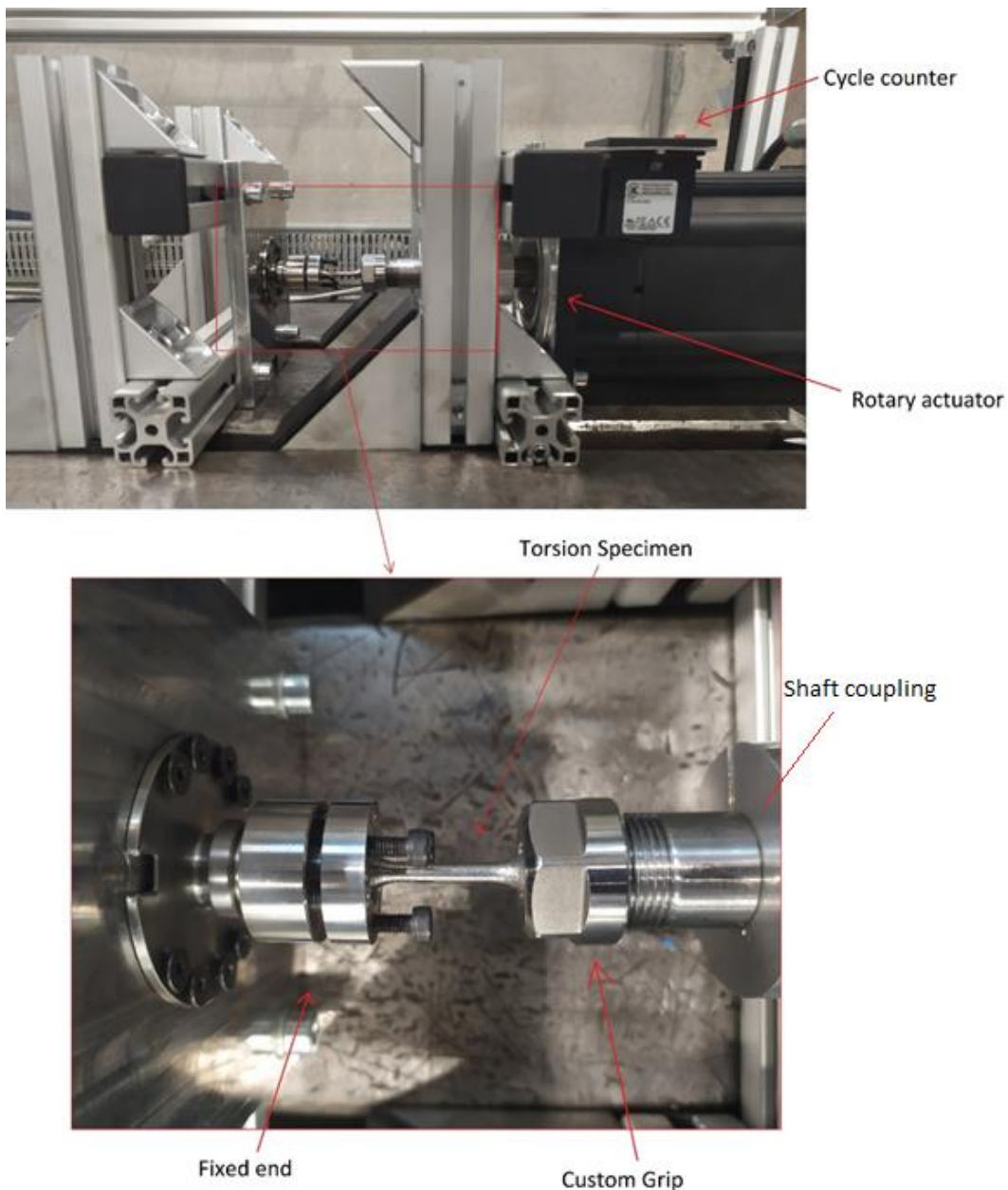


Figure 3. 11: Torsion Test Rig

The fatigue test rig depicted in Fig. 3.11 comprises a Lenze MCS synchronous servo motor which is capable to apply a maximum of 23 Nm torque and can give enough angular displacement to the test specimen. Torsion testing requires twist loading by the motor at the right end and fixing the other end such that the specimen cross-section is under pure shear loading. A suitable gripping is necessary for accurate transmission of torque and motion at the motor side and withstands the same torque at the fixed end. Given the CAD model assembly of the test rig in Fig. 3.12, a custom adaptor was designed to clamp the specimen at the motor side. Whereas the existing gripping system at the fixed end side was able to clamp our test specimen of 8mm external diameter without needing any change.

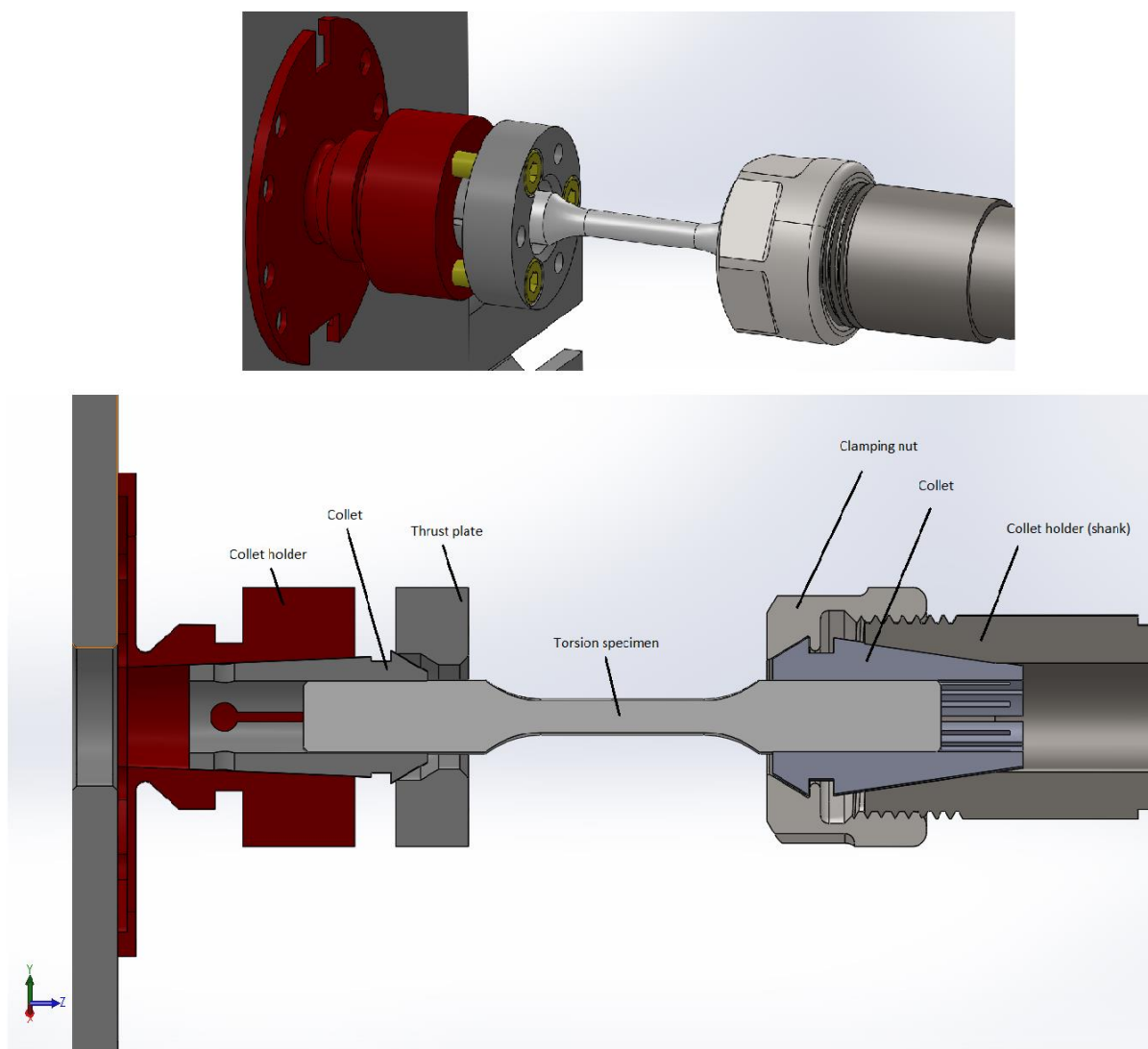


Figure 3. 12: Test rig CAD model

In order to apply pure shear stress to the specimen, the two sides of the test bench must be aligned perfectly on a straight platform to prevent any possible redundant bending stress

which can lead to wrong fatigue life assessment of the specimens. The existing test bench configuration had some amount of tilting on the fixed end side due to the misalignment of the blocks with the track of the fixing platform. Therefore, two thin straight sheets were designed and manufactured as shown in Fig. 3.13 to assure a perfect alignment between the two sides of the test rig. The two thin plates were placed under the two fixing blocks of the fixed end side. The dimensions can be seen in the technical drawing in Appendix A.

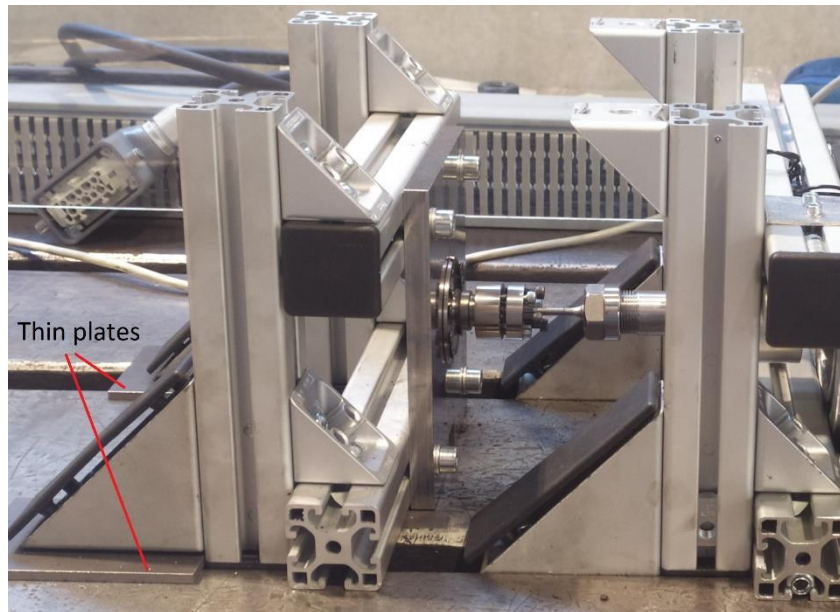


Figure 3. 13: Thin plates

3.2.6 Custom Grip Design

To ensure a strong holding of the specimen to prevent any backlash while rotating, a custom mechanical collet type of grip was chosen and a proper collet holder (shank) for it was designed for the motor side of the test bench. The left side which is the fixed side of the test bench had already an ER16 type of collet of grip which can hold our 8mm specimen end, therefore, the custom adaptor was designed only for the moving side. ER16 is the standard name notation for collects and represents the size of the workpiece that it can clamp. The number 16 is the opening diameter of the tapered receptacle, in millimeters. Clamps have been standardized with DIN 6499 B (also ISO 15488 B). Hence, a similar type of standard ER16 collet that can be seen in Fig. 3.14 was chosen to clamp the specimen from the other side. The collet must be tightened with an ER16 clamping nut of the same size.



Figure 3. 14: ER16 clamping nut and collet

The ER16 collet and the clamping nut in Fig. 3.14 were chosen according to the ISO 15488 Standard and bought from a machine component shop (Kemmler) that manufactures those components in compliance with the standards. The collet can clamp round specimens with a diameter range between 7 and 8 mm such that it can clamp our specimen which has an 8mm diameter.

For the collet to be assembled on the testing bench, a collet holder must be used. The collet holders don't come with a standard length and size. Therefore, it was designed on SOLIDWORKS according to the collet dimensions determined by the standard. Fig. 3.16 shows the collet holder that the IPeG workshop manufactured for us. The geometrical details of the shank were carefully considered since any possible wrong dimension would cause misalignment with the collet and clamping nut.

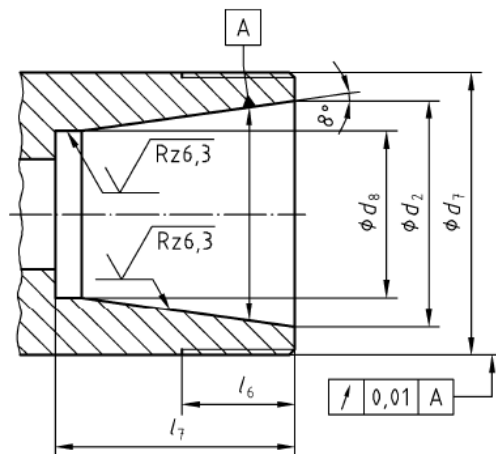


Figure 3. 15: Collet Holder design guidelines according to DIN 15488

The dimensions that must be considered for the collet holder as in Fig 3.15 were given and can be seen in the technical drawing in Fig A.1 in the Appendix section.



Figure 3. 16: Collet holder

To transmit the rotary motion, a split muff coupling was used between the motor shaft and collet holder. It assures a rigid type of clamping.



Figure 3. 17: Split muff coupling

3.2.7 Alignment Check

It is essential that uniform stress distribution be obtained for each fatigue test. Axial alignment of the torsional fatigue test machine has a critical role in this uniform pure shear loading. According to the ISO 23788 Standard, a split bar that is geometrically similar to the specimens being tested as in Fig. 3.18 or an axial alignment specimen with strain gauges shall be used. With the same logic of the former method, axial alignment was assured by using directly one of our test specimens that was broken during one of the test runs of the torsion test rig.

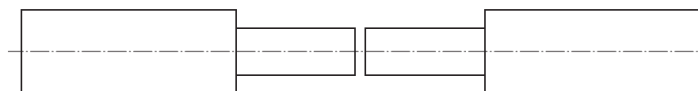


Figure 3. 18: Split bar for axial alignment

The two sides of the split test specimen were mounted on the clamps and since they have identical failure paths, they fit each other's broken area perfectly. In this way, the alignment was checked both qualitatively and relatively quickly.

3.2.8 Instrumentation for Monitoring

A cycle counter is necessary for recording the number of cycles to failure of each test. It shall either stop automatically when a specimen fails or record at which number of cycles the specimen failed. The device used in our test machine is the Kübler Codix Pulse Counter which is a type of digital magnetic cycle counter (Fig. 3.19). It composes of an 8-digit LCD screen that displays the number of cycles and a small round magnet that is stuck on the surface of the adaptor. It can count movements as fast as 12kHz.



Figure 3. 19: Cycle counter

Computerized data collection ensures that collection rates are fast enough to qualify for the standard. The software for controlling and monitoring all the relevant data is Lenze Engineer. The instantaneous actual position (angle), actual torque, power of the motor, etc. can be monitored and saved in a log file by this software.

3.2.9 Motor

The motor on the fatigue testing rig is a Lenze MCS 14 type 14L15 model synchronous servo motor. They are particularly suitable for applications that require high precision, compact dimensions, and high dynamics.

M_r [Nm]	n_r [rpm]	P_r [kW]	I_r [A]	M_0 [Nm]	I_0 [A]	M_{max} [Nm]	I_{max} [A]	J_{mot} [kgcm ²]
23.0	1500	3.6	9.7	28	12	77	37	23.4

Table 3. 6: Lenze MCS 14L15 synchronous servo motor data

3.2.10 X-ray Computed Tomography Scans

An available CT device in the mechatronics laboratory at IPeG, Bruker SkyScan 1275 3D X-ray Microtomograph (Fig. 3.20) was used for scanning our samples prior to the torsion fatigue testing.



Figure 3. 20: Bruker SkyScan 1275 3D X-ray Micro-CT Setup

SkyScan 1275 Micro-CT is a desktop laboratory system that allows for imaging and 3D reconstruction of the internal microstructure for different types of objects non-destructively. It consists of a combination of the micro-CT scanner and a computer with system control software, reconstruction software, and application software. The scanner contains a micro-focus X-ray source with high-voltage power supply, a two-dimensional X-ray, and a precision object manipulator. The object manipulator performs sample positioning under operator commands through control software and allows changing image magnification by moving the object between the X-ray source and the detector. It also rotates the object during scanning to acquire multiple angular views, which will be used for topographical 3D reconstruction. The scanner also includes all necessary control systems and associated electronics. The micro-CT setup is supplied with different softwares for a variety of applications. For our purpose of porosity analysis, the softwares used are “NRecon” for reconstruction of 2D images to a 3D model; “Data Viewer” for viewing the reconstructed set of slices of the images; “CTAn (CT-analyzer)” for building the 3D model from the micro-CT scans and measuring the morphometric parameters such as porosity analysis which is the main matter of this research; “CTvol (CT-volume)” for intuitive viewing of the 3D model created by CTAn; and finally an external software which is called “GOM Inspect Pro” for creating/modifying the STL files for further analysis of porosity in the critical region of the torsion fatigue test specimens.

Table 3.7 shows the specifications of the SkyScan 1275 micro-CT scanner. It allows the user to change these parameters prior to the scanning. Depending on the settings and parameters set such as image pixel size, resolution, single or partial scan, object height, etc., the scanning time will be shorter or longer. Due to the height of our specimen and the

minimum possible pixel size that can be chosen for scanning it for the most detailed porosity analysis, single scan was not possible. Hence, 3 partial scans have been made for each sample and it took 30 minutes per one partial scan. Therefore, approximately 1 hour and 30 minutes were needed for one sample to be scanned completely. Also, reconstruction time is longer when the scans are partial. Reconstruction processing time were approximately 40 minutes for each specimen.

Feature	Specification
X-ray Source	20 – 100 <i>kV</i> 10 W < 5 μm spot size at 4 W
X-ray Detector	Active Pixel CMOS flat panel 3 MP (1944x1536) 75 μm pixel size
Max Object Size	96 mm diameter 120 mm height
Dimensions	W 1040 mm x D665 mm x H 400 mm
Power Supply	100 – 240V AC, 50-60 Hz, 3A max
Energy Filters	1 mm Al and 1 mm Cu

Table 3. 7: SkyScan 1275 micro-CT Specifications

Below, Table 3.8 are the parameters used for the scans.

Parameter	Value
Image Pixel Size	9 μm
Source Voltage	100 <i>kV</i>
Source Current	100 μA
Rotation Step	0.25 deg
Energy Filter	1mm Cu
Rotation	360 deg
Frame Averaging	5

Table 3. 8: Scanning Parameters

Prior to the scanning, the scanner must be heated in order to reach 100 *kV* source voltage and 100 μA source current. Also, a waiting time after reaching the desired voltage is suggested by the Bruker micro-CT tutorials until the brightness⁸ level has stabilized. Fig. 3.21 shows the brightness level is starting to become stabilized when the X-ray source is on for 20 minutes. However, if the device is older, much more time is needed until the image brightness is stable. Usually, higher values of brightness are better. It also depends on the energy filter used. 1 mm Cu filter gives the highest amount of brightness for our samples.

⁸ Brightness is the indicator how well we can see the internal structure of the object being scanned.

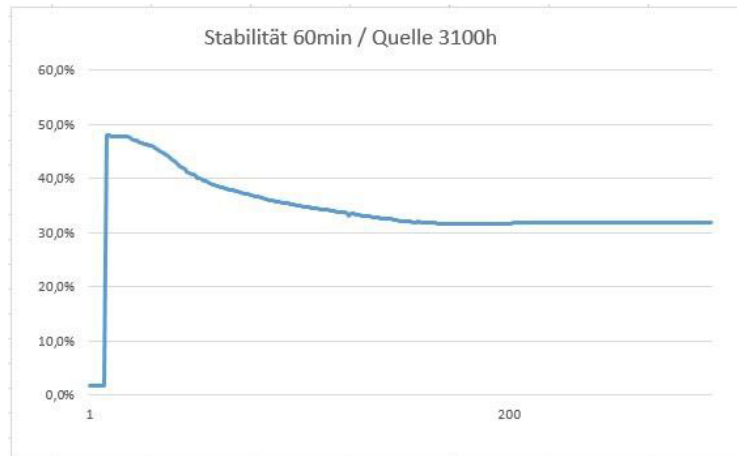


Figure 3. 21: Brightness level stabilization by time

Around 90% average and 15% minimum brightness level is recommended for a good scan. Fig. 3.22 shows the image brightness level on the gauge section of our sample. The average and minimum values seem to be good enough to start the scanning process. However, for the two ends that have 8 mm diameter, the minimum brightness level fell below 7%. Therefore, they are not selected for the desired scanning region. Only the gauge section and until 5 mm diameter were considered for the reconstruction of the images.

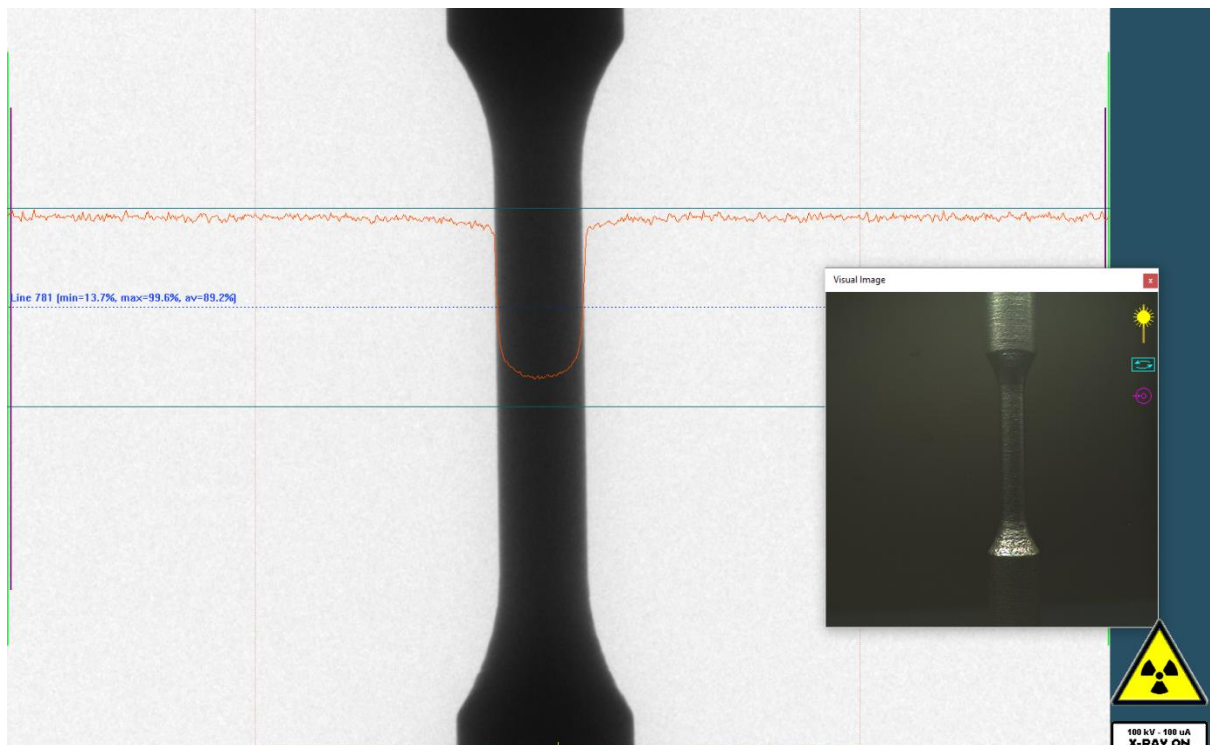


Figure 3. 22: Brightness level for the torsion specimen

After the stability of the brightness line, the scanning parameters must be selected. Settings that have been modified prior to the scanning are as follows:

- Image pixel size: it is set to $9\ \mu\text{m}$. The lower the pixel size, the closer the image to the X-ray source. Therefore, a more detailed visualization of the internal structure of objects.
- Rotation step: it is set to 0.25 deg. This parameter is the distance between the individual images. Thus every 0.25 degrees an image is taken.
- Frame averaging: this value is set to 5. This parameter minimizes the image noise. By higher averaging, the noise is lower. Typical values are 2-8.
- 360° scanning: 360-degree scanning is required for a full scan. The specimen must not rotate out the image during scanning. Hence, care must be taken to ensure a rotation in the camera's view.
- Energy filter: 1mm Cu filter is chosen. The best brightness level was acquired with this filter.

These parameters are chosen as a compromise between the best scan quality and scanning time.

After the scanning completed, reconstruction process must be done. As indicated above, the two ends were not included in the scans. Fig. 3.23 shows the region (where the diameter is $<5\ \text{mm}$) selected for reconstruction of the images.

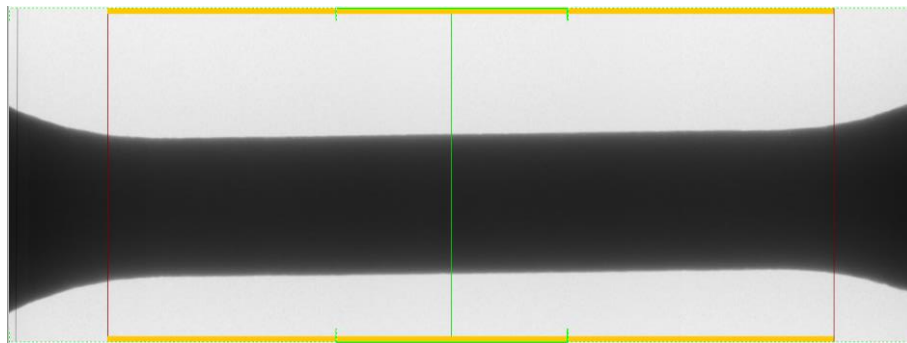


Figure 3. 23: Area of interest for reconstruction

Moreover, to realize how poor the scan quality is in the regions where the diameter is larger than 5 mm, reconstruction has been completed for the full size of the specimen. Fig 3.24 shows the binary images acquired by CTAn. It can be seen that noise is dominant in the image of the 8mm end grip section (b) whereas the pores are clearly seen without the presence of noise in the image of the gauge section of 4mm diameter (a). Hence, it has been confirmed by these images that scanning the whole geometry will cause noise therefore a wrong analysis of porosity because CTAn will recognize those noises as they are porosity. It is possible to get rid of them by some functions in the software, however, it will also cause losing some of the real porosity. Consequently, the grip sections were discarded from the porosity analysis.

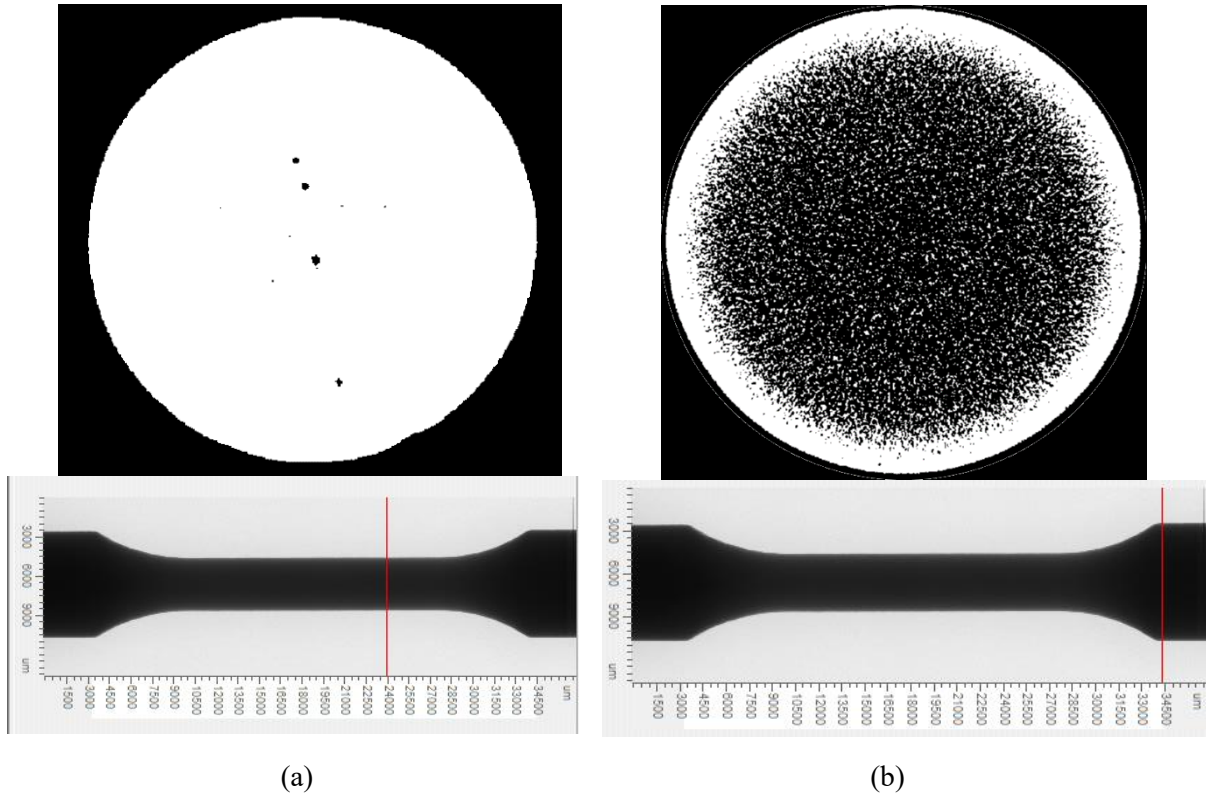


Figure 3. 24: Binary CT scan images (a) gauge section, (b) grip section

Reconstruction process requires modifying some parameters such as “post alignment”, “beam-hardening correction”, “ring-artifacts reduction, and “smoothing”. Also, the “greyscale area” should be appropriately set to visualize the slices in a more apparent shape for the pores.

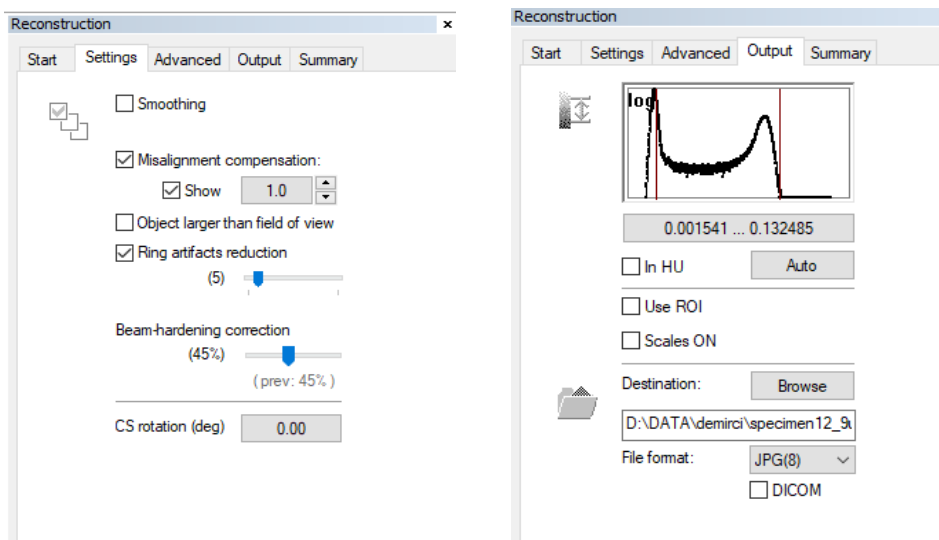


Figure 3. 25: NRecon parameters settings

Fig. 3.25 shows the parameter settings of NRecon. How they are chosen is explained below:

- The greyscale range was chosen between the two peaks for a good balance of the white and black. Below, Fig. 3.26 shows how this range can affect the image. When the right vertical line on the range curve is on the right side of the second peak, the image is too dark (a), conversely, when it is on too much left of the second peak, the image is too white (b) and so the voids (pores) aren't visible anymore. Therefore, the range is set in a way that includes the two peaks. Hence, the black and white balance is optimal (c).

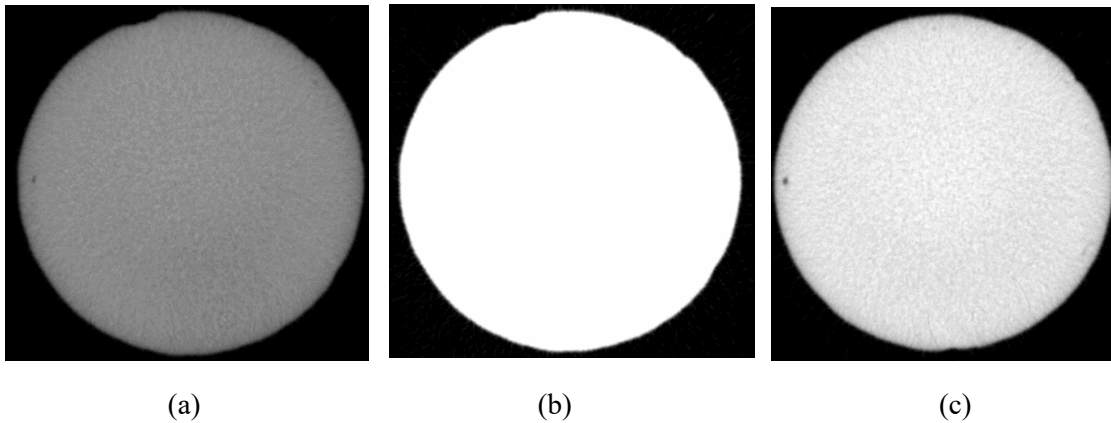


Figure 3. 26: Greyscale area difference (a) too black (b) too white (c) optimal range

- Smoothing wasn't necessary for our goal. It is effective in many cases as it can improve the image quality; however, they apply a blur not only on noisy areas but also important boundaries such as pores. Hence it can cause inconsistencies.
- Ring artifacts reduction is a function for removing the unwanted ring artifacts caused by dust or irregularities on the camera or X-ray beam of the CT when the regular maintenance hasn't been done for a while. Fig 3.27, (a) displays how the ring artifacts look like; and (b) depicts an image after the ring artifacts reduction filter.

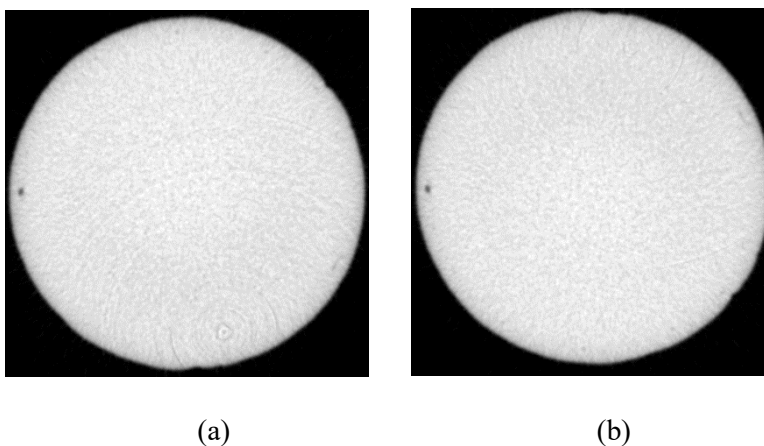


Figure 3. 27: Ring artifacts (a) ring artifacts are visible (b) no ring artifacts

- Beam hardening correction compensates for the X-ray attenuation inside the sample. If the material of the specimen is the same, the brightness (density) should

be the same inside throughout the specimen. Fig. 3.28 illustrates the effect of the beam hardening correction filter. In image (a) some dark areas are present towards the center of the sample. Image (b) shows a better-balanced brightness along the slice.

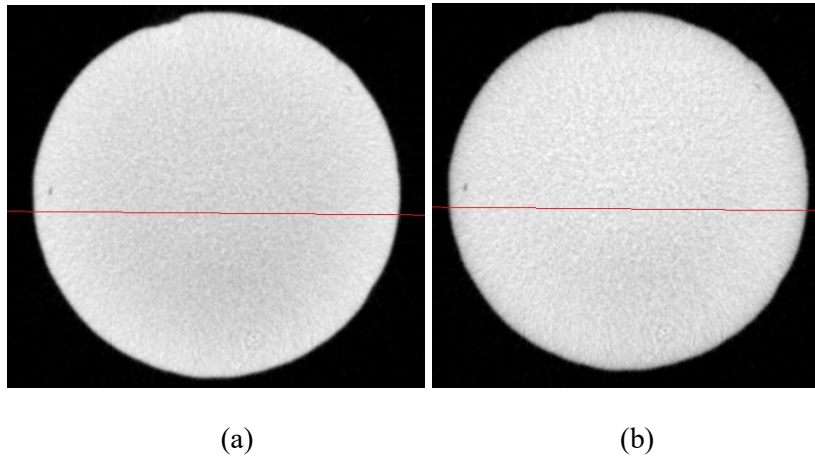


Figure 3. 28: Beam hardening correction (a) 30% correction, (b) 45% correction

- Misalignment compensation compensates for mechanical alignment. It is used for instance for irregularities such as open shapes that should actually be closed. Fig. 3.29 shows how this parameter can improve the image quality.

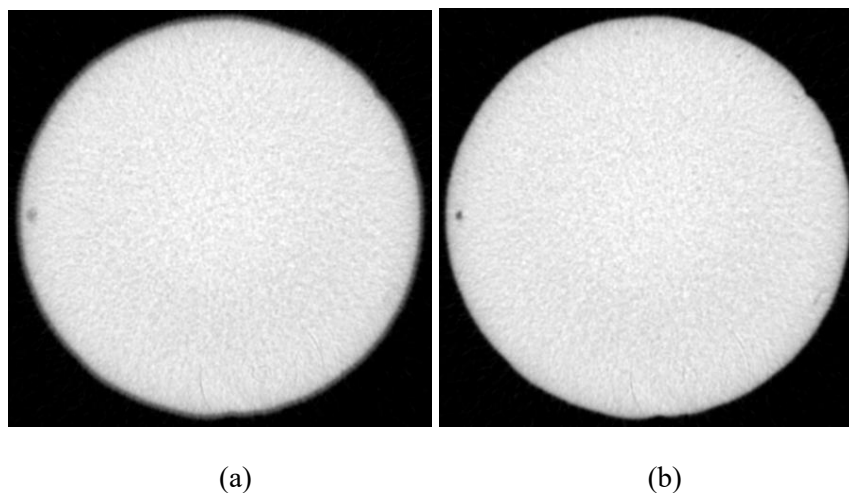


Figure 3. 29: Misalignment compensation (a) -1, (b) 2

After setting all the parameters, the reconstruction process can start. Once the reconstruction finishes, the dataset of the reconstructed images will be used by CTAn for the porosity analysis. Like NRecon, CTAn has filters and features that allow users to do desired applications. For porosity analysis by CTAn, there are more than one method. Among those, an advanced automated porosity analysis method which is called “Bitwise Operations” which can perform individual object analysis in the automatic protocol has been used. This operation will provide analytical results for the following parameters:

- Porosity calculation
- Pore size distribution
- Open versus closed porosity calculation

The first step to begin the porosity analysis is defining a threshold value for the grayscale. This value should be chosen in a way that it is not too low to lose internal porosity and not too high to cause too much noise to appear on the image. Considering that the grayscale from NRecon is chosen correctly, we can compare those images with the binary images of CTAn for realizing where the pores are so that we can eliminate the noise mixing with the real pores that are in the volume. Fig. 3.30 (a) shows the internal pores of a layer, and (b) is the binary image of that layer. It is seen that (b) represents all the internal pores correctly and has no noise, whereas (c) and (d) are two misleading images in which the former contains too much noise. Hence, it is difficult to distinguish between the pores and noise. The latter cannot display the pores due to its very low grayscale threshold value. The threshold values are 193, 210, and 141 for (b), (c), and (d), respectively.

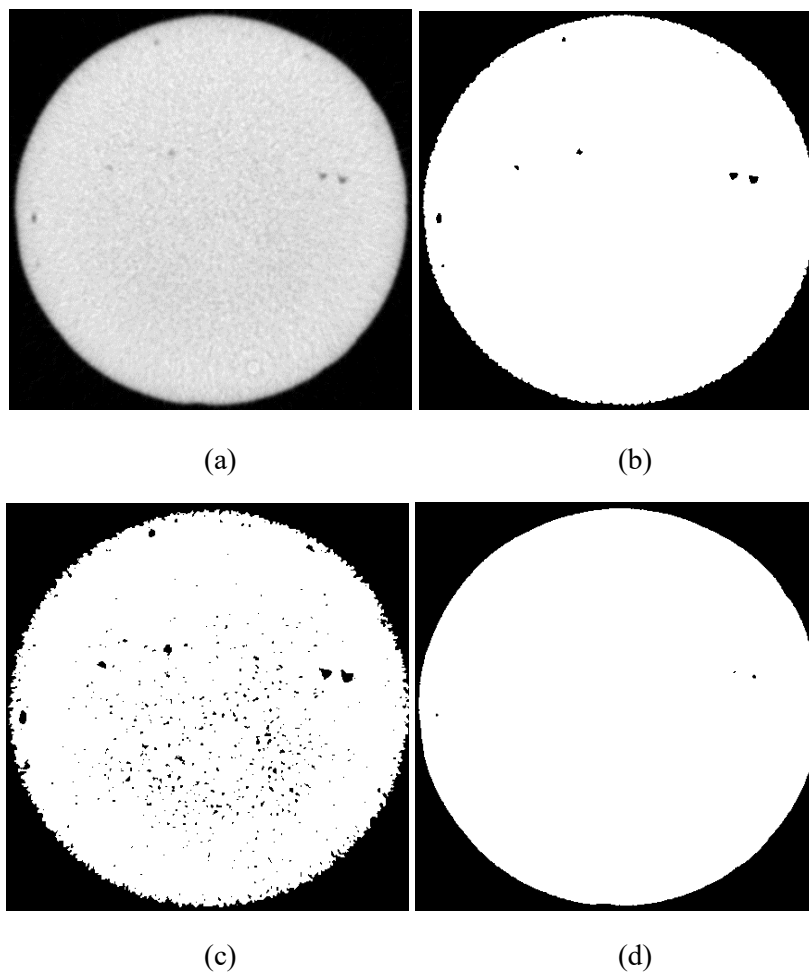


Figure 3. 30: Binary images showing the grayscale threshold difference (a) CT image of a layer showing pores, (b) a good binary image, (c) a binary image containing noise, (d) a binary image missing some pores

Generally, there are a couple of important basic concepts for porosity analysis in CTAn. Any white pixel is considered as an object, whereas black pixels surrounded by white pixels are considered as porosity (closed). Black pixels outside the object are discarded from the porosity analysis automatically by the software. Open porosity is considered as any black pixel located within a solid object that has any connection to the space outside the object. Knowing these concepts, different filters and features have been applied to the dataset of images. The features applied are as follows:

- **Thresholding:** it is related to the greyscale area of the binary images. It should be chosen according to the threshold value selected that allows us to see the real porosity without too much noise. As stated above, 193 is a good value for the low limit; and the high limit should be kept as it is: 255.
- **Despeckle:** it removes the undesirable speckles that might appear on the image. Both white and black pixels can be removed with this function. It is also useful to remove noise from the image. For our case, black speckles that have a volume less than 20 voxels were considered as noise. Hence, they are removed.
- **Bitwise operations:** it is used to perform the 3D porosity analysis by defining and manipulating the ROI (region of interest) and the image.
- **Morphological operations:** it is used to fix and smooth some of the sharp borders of the scanned images comprising the boundaries of the object.
- **3D analysis:** basically, it does all the analysis and calculations.
- **3D model:** creates 3D models such as STL.

Finally, the porosity analysis and a 3D model can be obtained. The 3D model is to visualize the open, closed, and total porosity. Also, the STL file extracted will be used for defining the critical region and porosity in it. Fig. 3.31 illustrates 3D models of two specimens visualized by CTvol. Green dots represent the closed porosity whereas red ones stand for open porosity. Specimen 14 (a) has an open porosity of 0.008% while specimen 15 (b) has only 0.001%. It can be clearly seen from two 3D models that (a) has more open pores than (b). Besides, the number of closed pores they have are close to each other; 827 and 987, respectively.

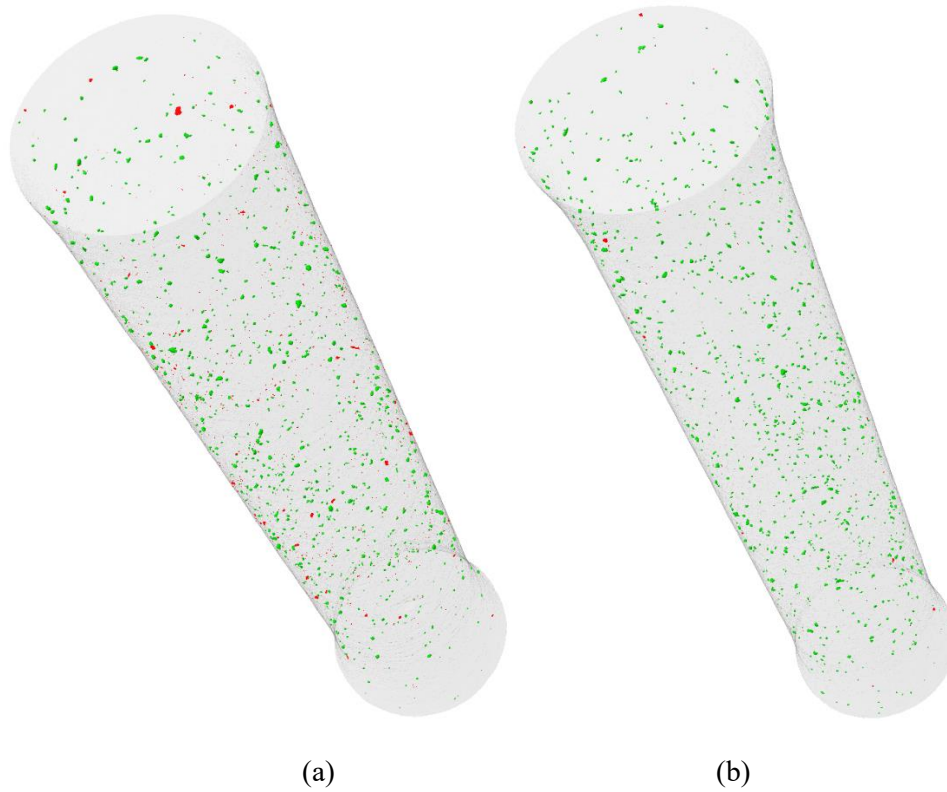


Figure 3.31: 3D models of two specimens showing porosity (a) specimen 14, (b) specimen 15

3D visualization is useful for an initial inspection when the difference in porosity is significantly higher in one of the two different samples. However, they don't provide much numerical information about the porosity. Therefore, 3D analysis feature of CTAn is used for the porosity calculations.

Porosity analysis by CTAn revealed relevant information about the specimens such as: object volume, number of closed pores, closed, open, and total porosity percentages, total object density, porosity size range etc.

3.2.11 Critical Region and Pore Location Effect

A critical region that was considered to influence the fatigue life of specimens was defined. Critical region means that the surface and subsurface area of the geometry where pores are more effective in initiating and propagating the fatigue cracks. The critical region chosen starts at the radius equal to 1.35 mm and ends at the surface where the radius is 2 mm. This conclusion was drawn after an Abaqus simulation was run in which four different sized, randomly shaped (almost spherical) pores were placed on the surface and within the specimen model with gaps of 0.2 mm between each pore. The four different sizes are obtained from the porosity analysis by CTAn, and they are the mid-ranges of the

pore size range outcomes. The sizes of the placed pores in the model are $18\ \mu\text{m}$, $36\ \mu\text{m}$, $54\ \mu\text{m}$, and $72\ \mu\text{m}$. This method has investigated which size of pores and at what distance from the surface is more effective in fatigue failure. Fig. 3.33 shows the stress contours from the Abaqus simulation of the torsion model in the presence of the pores mentioned.

A similar method of placing pores within the model is used by other researchers too. In a recent study, Li et al. [97] found that stress concentration occurs around pores in a specimen when loaded. As the stresses around the pores in the specimen exceeded the maximum stress at the surface, fatigue cracks initiated from the internal pores. Furthermore, like our method determined that near surface pores are more detrimental to fatigue behavior, Li et al. also observed that stress concentration was enlarged greatly with the decreasing distance of the pore to the specimen surface. When the pore was located in the sub-surface area of the specimen, the stress concentration around it increased significantly.

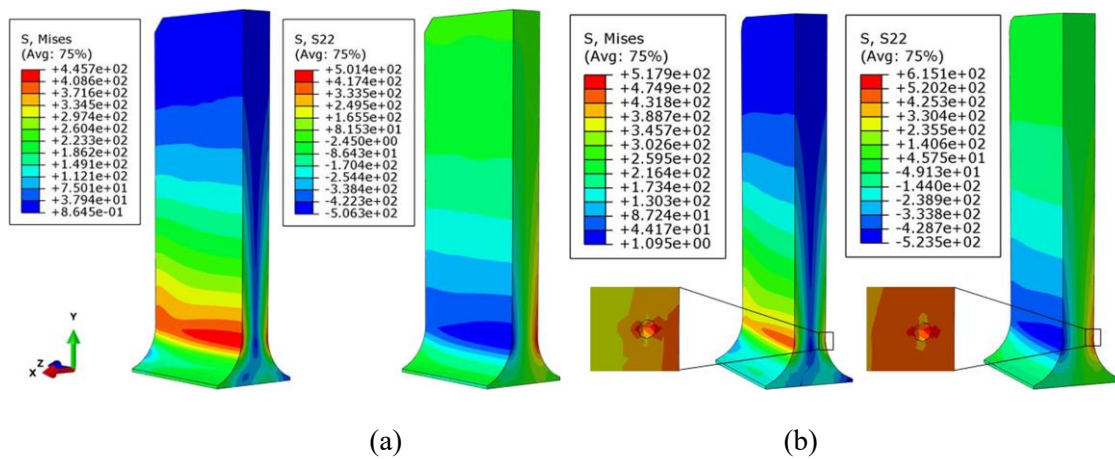


Figure 3.32: Distribution of Misses and S22 stress of FEM models: (a) non-porous model (b) model containing $\text{Ø}0.09\ \text{mm}$ pore and $0.16\ \text{mm}$ distance under specimen [97]

They stated that the model containing the pore had the same vibration stress distribution as the non-porous model except for the pore area as the maximum Misses and S22 shear stress greatly exceeded the stress on the surface of the model. The maximum Misses and S22 shear stress in the non-porous model were $446\ \text{MPa}$ and $501\ \text{MPa}$, respectively, whereas, in the model with pore, they were $518\ \text{MPa}$ and $615\ \text{MPa}$. Therefore, fatigue cracks initiated from the internal location of the specimen due to the high level of stress around the pore as the river-like stress pattern at proximity to the sub-surface pore shown in Fig. 3.32 (b). Also, further information provided by SEM images on how the pores initiated and propagated the fatigue cracks with a river-like crack pattern started from the internal pore can be seen in the same research in [97].

Similar to the method mentioned above, two simulations were run with a torque magnitude of $6.4\ \text{Nm}$. A model without pores and another one containing pores were simulated to

distinguish between different stress levels and understand better the effect of pores with the stress contours of the analyzed model.

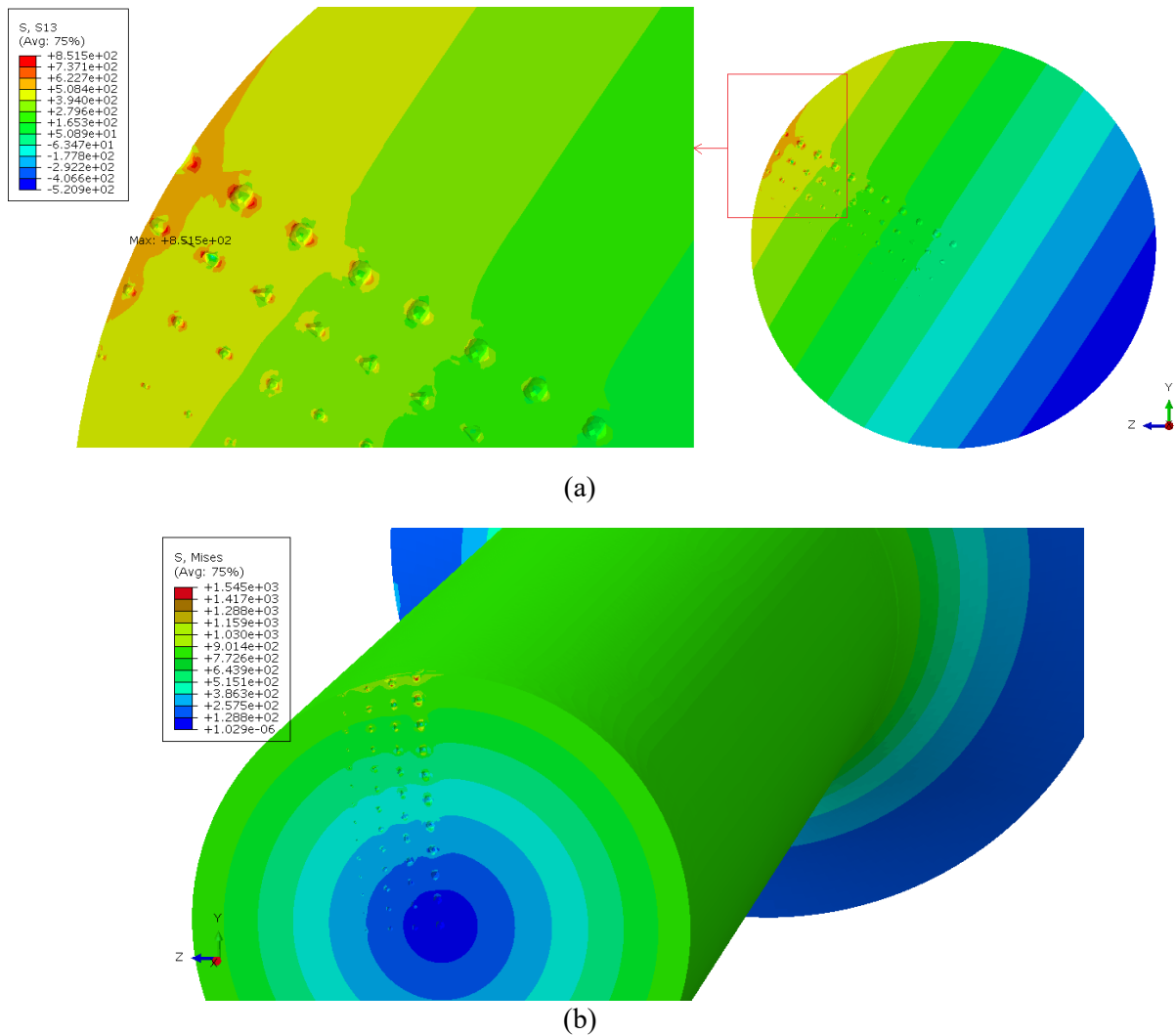


Figure 3.33: Stress contours with the pores: (a) Shear stress S13, (b) von Mises

The influence of the pores in the critical region is crucial regardless of the loading type (static or dynamic), as they are the stress concentration factors. From the stress contours' colors, one can observe that the colors are homogeneous where there are no pores. Also, the pores near the center of the model, regardless of their size, don't change the homogeneous stress distribution as can be understood from the very similar colors of the pores and non-porous sections in Fig. 3.33.

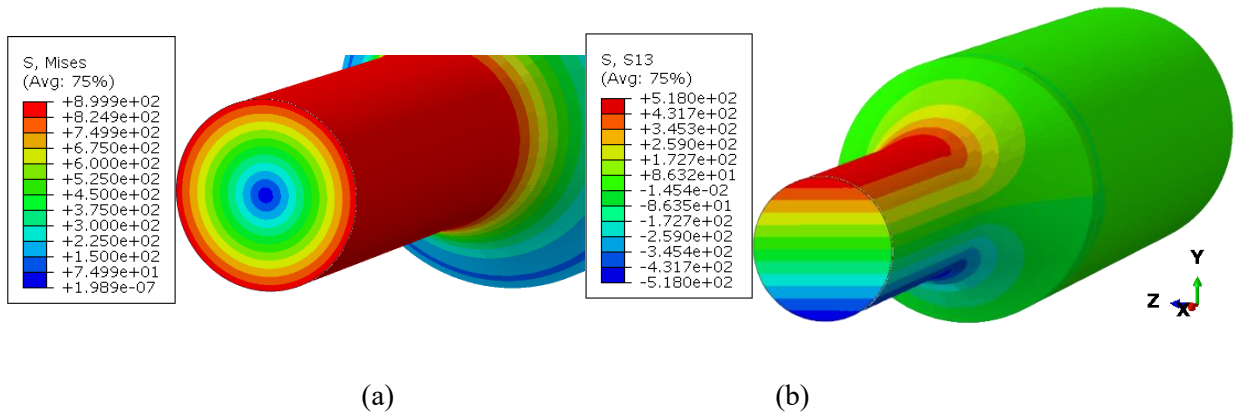


Figure 3. 34: Stress contours of the non-porous model: (a) von Mises, (b) Shear stress S13

The difference between the maximum Misses and S13 shear stresses of the two models shown in Fig 3.33 and Fig 3.34 are very significant. One can easily see that in Fig. 3.33, the maximum stresses are increased around the pores up to 1545 MPa for the Misses and 851 MPa for the S13 shear stress whereas in the model without pores shown in Fig. 3.34 the maximum stresses are 900 MPa and 518 MPa, respectively. Maximum stresses in the sections other the pore area are very similar in both models. The porous model has maximum Misses and S13 shear stress values of 901 MPa and 508 MPa, respectively around the surface where there are no pores. This result underlines the importance of the near surface pores, in our case pores that are present beyond the radius of 1.35 mm as the rest of the pores have no significant difference in terms of maximum stress levels. It can be seen from the Fig. 3.33 that the presence of the pores is increasing both the Misses and S13 shear stress. In this simulation, 6.4 Nm magnitude of torque was applied to the model which is almost the maximum value applied in the real fatigue tests. On the opposite side where there is no pore, the shear stress observed is 520 MPa whereas in the vicinity of the pores, especially until where the radius is at 1.35 mm, the shear stress S13 is increased up to 851 MPa.

After obtaining these results, the pores that aren't in the critical region were removed in order to see whether the number of pores in the critical region is the reason for the earlier fatigue failure for some specimens which have a less number of closed pores but failed before the specimens that have higher number of closed pores. To do that, an external software called GOM Inspect Pro was used to modify and adjust the STL files because the STL export function in CTAn is not very handy [98]. After exporting the STL file from CTAn, a number of operations should be applied by GOM Inspect Pro. Firstly, a smoothing operation is applied because the pixel size in the exported STL file is quite poor. The “surface tolerance factor” value for the smoothing operation should be chosen carefully. In this case the suggested value is twice the pixel size of the dataset. The pixel size we used is 9 μm . Hence, the surface tolerance factor is chosen as 18 μm . The next step is correcting the surface holes and other errors on the surface because an STL file

consists of a completely closed surface. Smoothing function of GOM Inspect Pro can cause some errors on the surface or there can be some errors already included when CTAn exported the STL files. Thus, the “correct mesh errors” function is used. This operation is repeated until there are no more errors. This operation can also cause some errors in the model. Therefore, as a last step, the “repair holes” function is used to eliminate the possible holes on the surface. The modified STL file can now be exported again from GOM Inspect Pro. The last step is removing the pores outside of the critical area. To do that, SolidWorks 2020 was used.

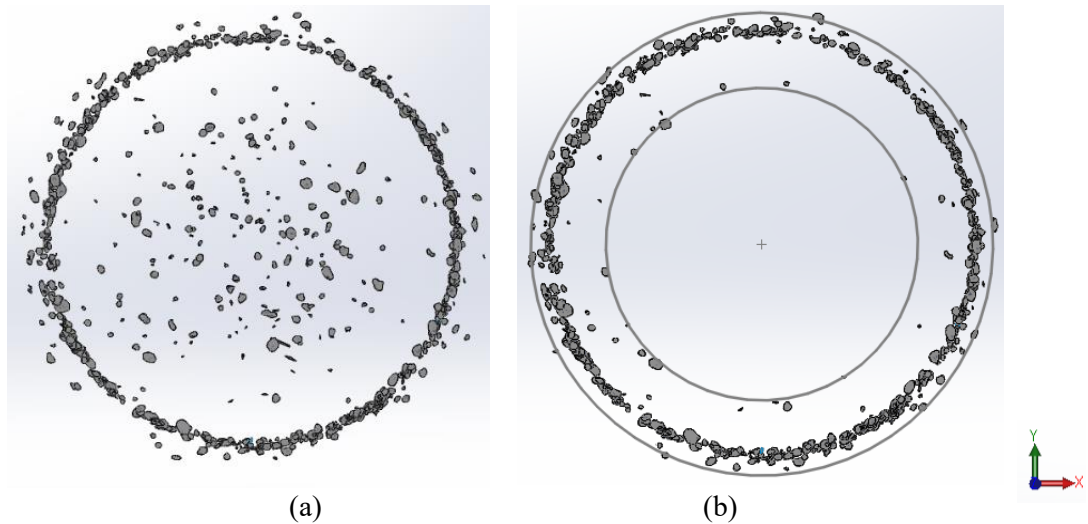


Figure 3. 35: Specimen 16: (a) all pores, (b) pores in the critical area

Fig. 3.35 shows the initial state of specimen 16 and after the pore cleanup operation. The procedure is rather simple. On the perpendicular view to the front plane, two circles with radii of 1.35 mm and 2 mm are drawn. The pores inside the smaller circle and outside the bigger circle are deleted, and then the number of pores between the circles is noted as the number of pores in the critical area.

To emphasize how this method is useful for understanding the fatigue behavior of the specimens, it is important to grasp why the internal pores that aren't in the critical region were removed. They have been eliminated since they are ineffective in initiating or propagating the fatigue cracks as the stresses around these pores aren't increasing with respect to the other non-porous sections. Therefore, they were discarded from the pore population and only the pores in the critical region are counted for the number of pores. In this way, whether the number of pores significantly impacted the fatigue life was investigated.

3.2.12 Fatigue Test Procedure

The mounting of specimens is rather simple. Each specimen is inserted through the hole on a stationary grip and then it is carefully placed inside the driven grip so that the axis of the

specimen lies along the axis of the torsion of the testing machine and the aimed stress pattern is applied. Clamping the specimen on each side was done with extra care to ensure that no/minimal axial stress is applied to the specimen during the mounting of the specimen on the testing machine. The bolts on the stationary side and the clamping nut on the driven side were turned in order so that none of the two sides can impose unwanted axial stress on the specimen mounted.

The frequency of the torque cycle was set to 5 Hz as a compromise for the high and low-stress amplitudes. Generally, it was found that at higher frequencies there is a discrepancy between the position setpoint, and the actual position read on the motor shaft. To avoid this inconsistency, a frequency high enough to maintain all the tests in a reasonable time and not low enough to refrain from excessive time consumption was chosen. Fig 3.36 shows the perfect oscillation alignment between the torque setpoint and the actual motor torque data.

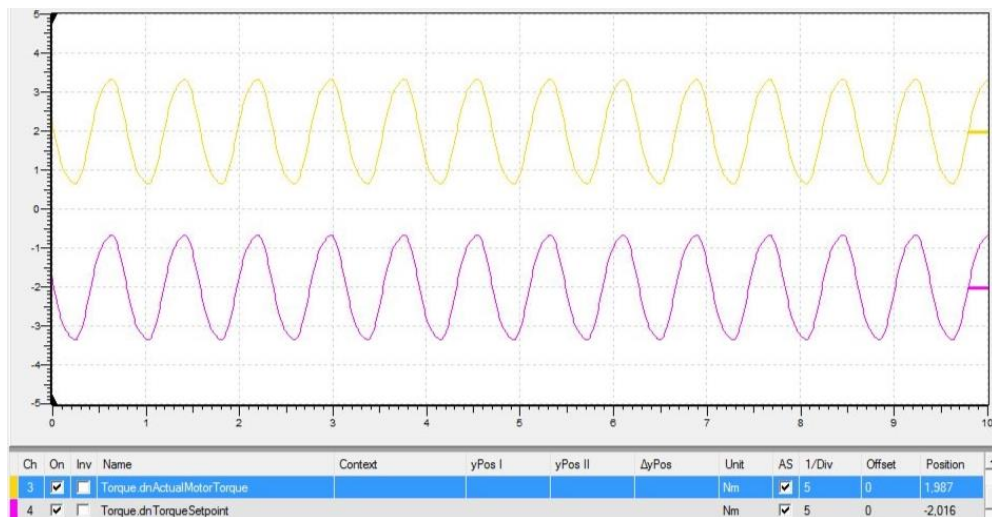


Figure 3. 36: Oscilloscope for torque cycle

As ISO 12107 suggests, four different torsion angles were chosen to apply the fatigue tests in order to build an S-N Curve that is not misleading. Firstly, a twist angle of 5.1° that is large enough to fail the specimen in the LCF regime was chosen to seek a correlation between the porosity and fatigue life. After that, a twist angle of 4.4° was selected for the beginning of the HCF regime to see the tendency. Then, two different angles, 3.6° and 2.7° , were chosen to see the porosity-fatigue life correlation for higher number of cycles in the HCF regime. In this way, the correlation of different intervals in the HCF regime was observed.

Specimen	Maximum Twist Angle (°)	Minimum Twist Angle (°)	Maximum Torque (Nm)	Minimum Torque (Nm)	Maximum Stress [τ_{max}] (MPa)	Minimum Stress [τ_{min}] (MPa)	Stress Amplitude [τ_a] (MPa)
4	5.06	-5.10	6.79	-6.83	540.18	-543.36	541.76
5	5.07	-5.14	6.86	-6.78	545.74	-539.38	542.56
8	5.08	-5.14	6.77	-6.77	538.58	-538.58	538.58
9	5.08	-5.12	6.80	-6.70	540.97	-533.02	536.99
20	5.08	-5.12	6.74	-6.74	536.20	-536.20	536.20
6	4.38	-4.42	5.80	-5.84	461.42	-464.60	463
11	4.37	-4.44	5.78	-5.79	459.82	-460.62	460.2
18	4.43	-4.45	5.72	-5.78	455.05	-459.82	457.44
21	4.38	-4.42	5.73	-5.76	455.85	-458.23	457.04
22	4.38	-4.42	5.73	-5.76	455.85	-458.23	457.04
7	3.66	-3.67	4.90	-4.95	389.82	-393.79	391.8
12	3.64	-3.67	4.93	-4.96	392.20	-394.59	393.4
13	3.67	-3.69	4.91	-4.93	390.61	-392.20	391.41
19	3.69	-3.70	4.92	-4.94	391.41	-393.00	392.20
23	3.67	-3.69	4.91	-4.93	390.61	-392.20	391.41
14	2.77	-2.79	3.83	-3.86	304.69	-307.08	305.9
15	2.75	-2.75	3.81	-3.81	303.10	-303.10	303.1
16	2.77	-2.77	3.80	-3.80	302.31	-302.31	302.31
17	2.75	-2.76	3.80	-3.81	302.31	-303.10	302.70
25	2.76	-2.77	3.79	-3.81	301.51	-303.10	302.31

Table 3. 9: Twist angle, torque, and stress values for the tests

The tests were run in degree-controlled mode. The precision of the twist angle varies between 0.07 and as low as 0.01 degrees and even identical positive and negative values were seen in some cases. The applied torque values are also quite precise such that the difference between the positive and negative torque values vary from 0.1 to 0.01 and even no difference in some cases. Table 3.9 shows the applied maximum and minimum twist

angle, torque, and stress on the samples that were tested with different twist angles. The tests were conducted in a fully reversed stress cycle with a stress ratio of $R = -1$ in which the maximum and minimum stresses are equal in absolute value. In fact, the maximum and minimum stresses aren't exactly equal, but the difference is so small that it can be negligible.

Furthermore, since the diameter in which the torque is applied changes gradually, the twist angle was theoretically calculated according to Eq. (5) where T is the applied torque [Nm], L is the length of the specimen section where torque is effective [m], J is the polar moment of inertia [m^4], and G is the shear modulus of the material [N/m^2].

$$\theta = \int_{L_1}^{L_2} \frac{T(x)}{G(x) \cdot J(x)} dx \quad (9)$$

Four different twist angles were chosen to conduct the fatigue tests as suggested by the ISO. 5.1° , 4.4° , 3.6° , and 2.7° . The first one is to represent the fatigue behavior in the LCF regime and the other three are for the HCF regime. Due to the time limitations of this thesis, none of the specimens were let for a run-out after 10^8 cycles. The HCF regime was kept below $2 \cdot 10^5$ number of cycles. The longest number of cycles to failure experienced by one of the specimens is 126.340 and it took 7 hours to complete the test. Also, the other tests which were performed with a 2.7° twist angle took around 7 hours. The 3.6° twist angle ones took approximately 2 hours each. The other tests which were in higher torque levels took less time until the failure.

The stress levels shown in Table 3.9 were not measured by the testing machine. They are theoretically calculated by using the torque values and section modulus of the specimens' gauge section and then confirmed with the FEM simulations. The formulation for the maximum stress values due to torsion (4) and the section modulus for torsional loading (5) are below:

$$\tau = \frac{M_t}{W_t} [Mpa] \quad (10)$$

$$W_t = \frac{\pi \cdot d^3}{16} [mm^3] \quad (11)$$

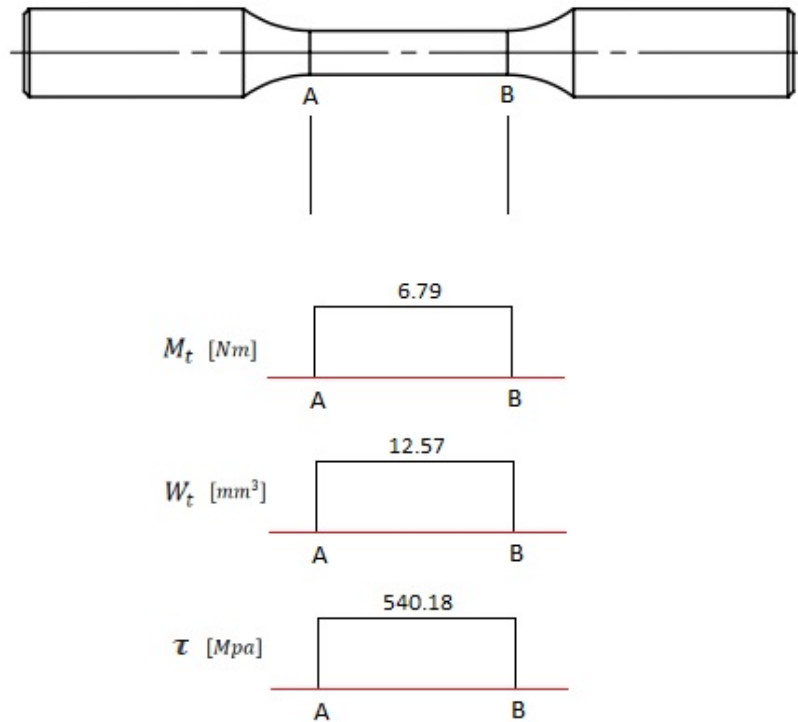


Figure 3.37: Torsional stress, torsional moment, and section modulus diagrams

The torsional shear stress distribution along the gauge section of specimen 4 can be seen in Fig 3.37. The stress level shown is the equivalent amount for the twist angle of 5.06° . This calculation also confirms the suitable specimen geometry and the accurate angle of twist level for the torsional fatigue application, as the shearing stress level caused by the 5.06° twist angle doesn't exceed the materials' ultimate shear strength⁹ or the yield strength and does not cause any plasticity in the specimen. Hence, the fatigue testing is guaranteed to be stress-controlled, and not strain-controlled.

Moreover, since the applied stress is shearing stress due to the torsional loading, the shear strength of the material should be known to prevent exceeding the limit and not cause yielding in the specimen. The von Mises criterion in the case of pure shear stress suggests that the magnitude of shear stress in pure shear is $\sqrt{3}$ times lower than the yield strength. Therefore, Eq. (7) express the theoretical shear strength of our specimen where R_p is the yield strength, and τ_p is the shear strength.

$$R_p = \sqrt{3} \cdot \tau_p \quad (12)$$

⁹ Ultimate shear strength: it is commonly estimated to be 60% of the ultimate tensile strength [101]

From the catalog shown in Fig. 3.4, the yield strength can be considered as $R_p = 1980 \text{ Mpa}$. Hence, the shear strength is found to be $\tau_p = 1143 \text{ Mpa}$. Therefore, the shear stress applied by the maximum twist angle (5.1°) which corresponds to 6.75 Nm torque will not yield the specimen so that a true fatigue behavior can be observed.

3.2.12.1 Fatigue Beach Marks

Microscopic visualization after the fatigue failure allows us to see the fatigue crack initiation and growth direction on the broken surface of the specimens. The “beach marks” are a very useful identification method to understand where the fatigue crack initiated (whether from the surface or internal defect). Therefore, a microscopic visualization was conducted for some specimens after the fatigue failure to understand this concept.

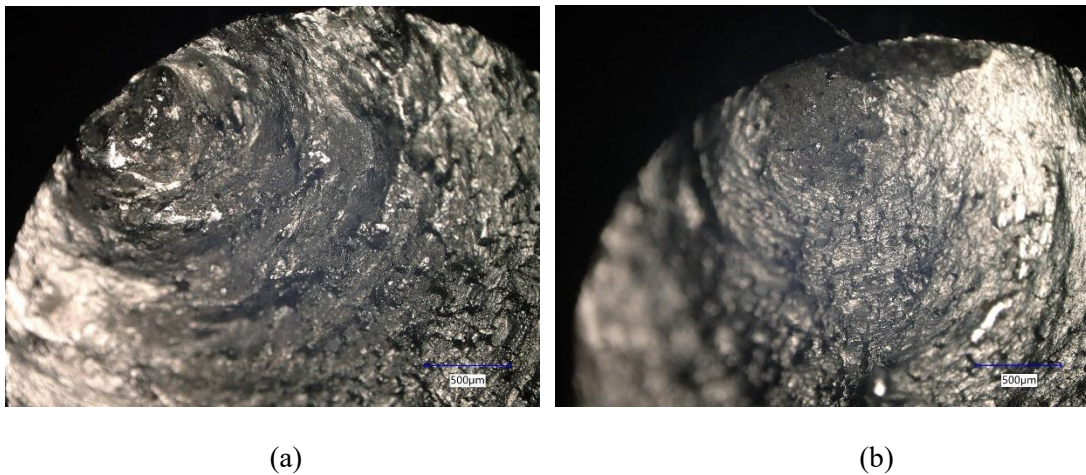


Figure 3. 38: Beach marks captured by the microscope: (a) specimen 5, (b) specimen 23

Fig 3.38 shows how the amount of load (twist angle in our case) affects the fatigue nucleation. Fig. (a) shows specimen 5, which has been tested with 5.1° (corresponding to 540 MPa), is considered as LCF, whereas (b) indicates the beach marks of specimen 23, which was tested with 3.6° (corresponding to 390 MPa) and is considered as HCF regime. One can observe that in (a), the beach marks are fewer, and the fracture area is larger, whereas on the contrary, in (b), there are many beach marks visible, and evidence of a lower load was applied. It seems that in both specimens, the fatigue crack started from a surface defect, as the beach marks shape suggests.

3.4 Obstacles and Solutions

CT scans were performed with a minimum image brightness level between 13.7 and 14.3% after the stabilization process. Generally, the Bruker micro-CT tutorials suggest a minimum brightness level of 15%. However, 14.3% was the highest obtained minimum brightness level with the maximum possible source voltage of 100 kV and a 1mm Cu filter which is the best one possessed. It was possible to increase the brightness level by decreasing the image resolution, but in this case, the presence of excessive image noise would not allow to analyze the object appropriately. Therefore, the scans were run with this brightness value, and it was enough to visualize all the internal porosity and analyze the data.

The torsion fatigue test machine had an axial misalignment due to the different height levels of the two sides. Hence, two thin straight sheets were designed and manufactured to ensure a good axial alignment of the machine. They were placed in between the rigid machine frame and assembly blocks.

Specimens 1, 2, 3, 10, and 24 could not be used in the actual fatigue tests. Specimens 1 and 2 were used while the fatigue testing machine was being tested for whether it could apply enough and precise twisting to the specimens. Specimen 3 was tested before the assembly of the two straight sheets. As a result, it experienced some amount of bending during the test which would mislead the number of cycles and amount of torque applied. Specimen 10 was misused due to a wrong application of torque caused by the user: it experienced a bigger amount of torque (multiple times) than intended at the beginning of the fatigue tests. Hence, continuing the testing with this specimen would mislead the results. Specimen 24 was undergone appropriate fatigue testing, but the cycle counter could not catch the number of cycles due to a displacement of the magnet that stuck on the adaptor. Consequently, it was discarded from the results list.

4. RESULTS

Following the non-destructive CT-based porosity analysis and given the number of specimens printed, a statistical evaluation has been made after acquiring all the possible relevant data that may influence the fatigue life. To relate the porosity ratio and fatigue life, different methods were tried. From the software CTAn, it was possible to collect some quantitative data such as total, open, and closed porosity volumetric percentages, pore volumes, the number of closed pores, and pore sizes (average size and size range) in a .txt file. These collected data have been compared to the number of cycles to failure in the fatigue tests to see whether or to what extent they influence the fatigue behavior. As indicated before, four different twist angles were used for the fatigue tests: 5.1°, 4.4°, 3.6°, and 2.7°, respectively, and the correlation was somehow stronger in the latter two when compared to the former two. From here, one can hypothesize that as the number of cycles increases (or as the load level decreases), the porosity ratios start affecting more the fatigue behavior. Correlation analyses have been conducted to test this hypothesis and confirmed that there is a weak correlation between porosity and fatigue life in the lower twist angles (at higher numbers of cycles) even though the analyses revealed that a larger set of experiments should be done to assure a statistically significant outcome. Nonetheless, more tests with statistically significant sample size are needed in the HCF regime to confirm this hypothesis.

Furthermore, a 3D visualization of the printed specimens was generated in a CTM file format. This file can be executed by another software from Bruker called CTvol. It allows distinguishing the open and closed pores by giving them and the specimen body different colors and transparency/opacity. CTAn also serves the purpose to create an STL file from the constructed CT images that are to be used for another porosity analysis to detect the number of pores that are in the critical region. An STL file consists of a completely closed surface and needs to be error-free for a good analysis. However, the STL export function in CTAn is not very good such that it can cause holes or other errors on the model when the STL is exported from CTAn. Therefore, another software, namely GOM Inspect, was used for this purpose. It can edit the STL after creating it by CTAn and correct the mesh errors. Only then, the pores of the critical region can be counted. The number of pores extracted from GOM Inspect is typically 3 to 7 % less than the pores found by CTAn. For instance, specimen 6 contains 347 pores according to CTAn, whereas GOM Inspect exposed 337 pores. While specimen 22 contains 794 pores according to CTAn, GOM Inspect could find 744 pores. Hence, a small portion of the pores disappeared during the STL creation phase by GOM Inspect.

4.1 CT Scan Results

The scanned area has been chosen prior to the scanning procedure and is not smaller than 5 mm in diameter. However, the reconstructed area was limited to 5 mm in diameter at the reconstruction phase of the scanned images because of the noise introduced in larger diameters, as indicated in the methodology chapter.

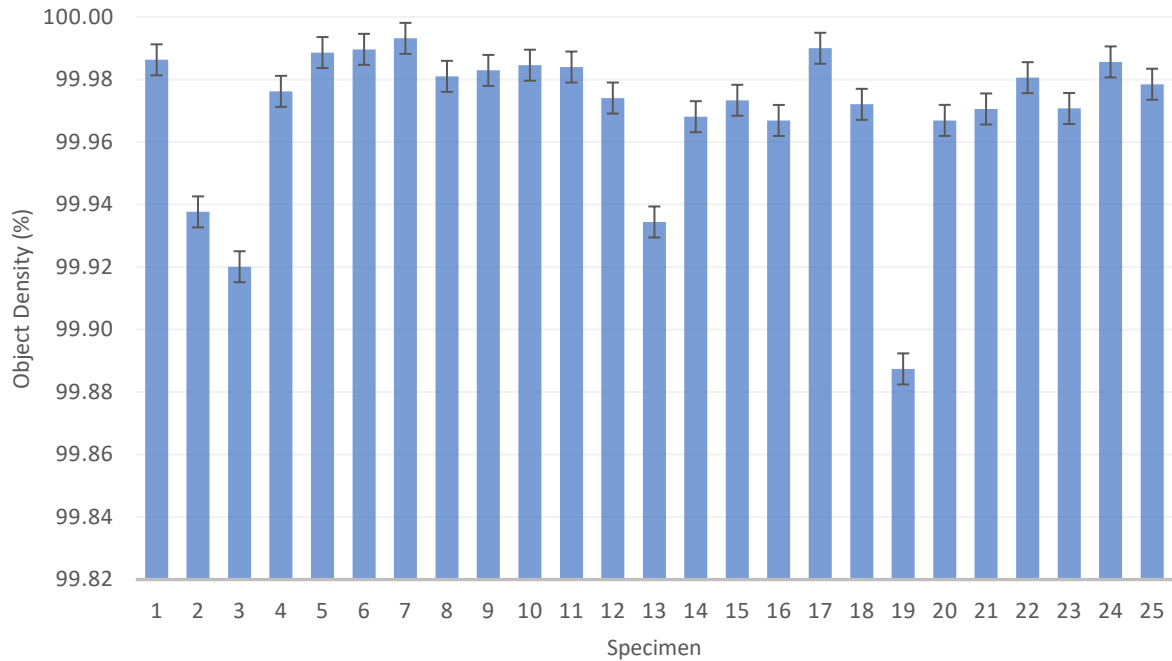


Figure 4. 1: Specimen relative density percentages

Fig 4.1 shows the object density of each sample scanned in the micro-CT. All the specimens except for one achieved the near full density (99.9+%). This is an important quality for a more reliable fatigue life assessment as more defects mean more probability of failure due to a crack initiation from a pore. Exhibiting less porosity is also beneficial for fatigue life prediction. The number of possible crack initiation points increases as the number of pores increases, meaning that more than one fatigue crack might start from different locations in the material, especially in the sub-surface area and from the bigger size pores.

In Table 4.1, the extracted porosity analysis results by CTAn can be seen. The average object density was found to be 99.97%, with a standard deviation of 0.025%. Even higher densities up to 99.99% could be achieved in some cases. Hence, our results confirm the claims of the DMLS printer manufacturer and powder supplier and verify the technology's reliability as the final printing products are supposed to be near fully dense¹⁰. This also proves that the process parameters used for our printing job were chosen correctly.

<i>Specimen</i>	<i>Object Density (%)</i>	<i>Total Porosity (%)</i>	<i>Closed Porosity (%)</i>	<i>Open Porosity (%)</i>	<i>Number of Closed Pores</i>
1	99.99	0.014	0.011	0.003	501
2	99.94	0.062	0.059	0.003	3702
3	99.92	0.080	0.055	0.025	4309
4	99.98	0.024	0.023	0.001	1470
5	99.99	0.011	0.009	0.002	397
6	99.99	0.010	0.009	0.001	347
7	99.99	0.007	0.007	0.000	262
8	99.98	0.019	0.018	0.001	595
9	99.98	0.017	0.014	0.003	516
10	99.98	0.015	0.015	0.000	744
11	99.98	0.016	0.015	0.001	661
12	99.97	0.026	0.017	0.009	640
13	99.93	0.066	0.037	0.029	1374
14	99.97	0.032	0.023	0.008	827
15	99.97	0.027	0.025	0.001	987
16	99.97	0.033	0.027	0.006	977
17	99.99	0.010	0.010	0.000	338
18	99.97	0.028	0.024	0.004	976
19	99.89	0.113	0.045	0.068	1739
20	99.97	0.033	0.030	0.003	1131
21	99.97	0.029	0.028	0.001	1118
22	99.98	0.019	0.018	0.001	794
23	99.97	0.029	0.025	0.004	934
24	99.99	0.014	0.014	0.001	603
25	99.98	0.022	0.020	0.002	709
AVERAGE	<u>99.97</u>	<u>0.030</u>	<u>0.023</u>	<u>0.007</u>	<u>1066</u>

Table 4. 1: CTAn Porosity Results

¹⁰ Near fully dense here means a relative density of 99.95+%

To understand whether the analyzed porosity values fit into a normal distribution, normality tests have been conducted for all the twenty-five samples and shown in Normal QQ (quantile-quantile) plots together with frequency distribution graphs and histograms. D'Agostino & Pearson, Anderson-Darling, Shapiro-Wilk, and Kolmogorov-Smirnov tests have been implemented to realize whether the porosity values are well-fitted in a normal distribution. The results revealed that none of the porosity analysis values passed the normality tests except for closed porosity distribution passing only the Kolmogorov-Smirnov normality test. GraphPad Prism was used to conduct the normality tests and obtain the Gaussian distributions.

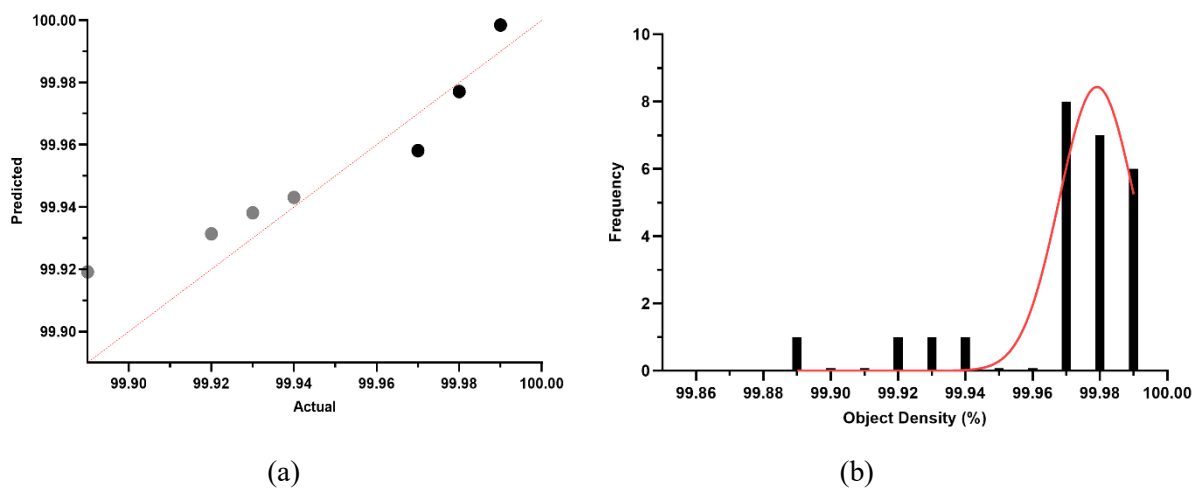


Figure 4. 2: Object Density: (a) Normal QQ plot, (b) Histogram with frequency distribution

Fig. 4.2 shows the normal QQ plot and histogram with a truncated normal distribution of the object density. It is apparent that most of the samples' densities clustered between 99.97% and 99.99%. The truncated normal distribution indicates that most specimens will likely have around 99.98% object density. It is also the median value. The mean value is 99.97% and with a standard deviation of 0.0246. The average density calculated 99.97% is also in good agreement with other research done with the same material 1.2709 and the same LPBF machine. Andronov et al. [99] produced AM samples using $100\ \mu\text{m}$ layer thickness together with other optimized process parameters and obtained an average density of 99.97%, a maximum density of 99.98%, and a minimum density value of 99.96%. Nonetheless, they analyzed the porosity of six samples by the XCT. Therefore, they probably did not find any outliers with this small sample size. The outliers of our data set have been identified by the ROUT method¹¹, which is a method to identify the outliers from nonlinear regression. With the help of GraphPad Prism, two outliers were found. Here, we aimed to find outliers for no more than 1%. Hence, samples exhibiting 99.89% and 99.92% object density were found to be the outliers of this dataset. Another common

¹¹ ROUT method is found by GraphPad and is based on the False Discovery Rate (FDR).

method for finding outliers is Grubbs' method. However, it can only identify one outlier in each dataset. Therefore, we did not prefer that method as we thought that our dataset contained more than one outlier.

To be more precise and present the findings in a more scientific way, an unpaired t-test has been implemented for these two groups of datasets to see the difference in the means. Fig. 4.3 indicates the object density estimation plot of these two groups for the t-test applied. The difference is quite small, 0.005400 ± 0.01039 .

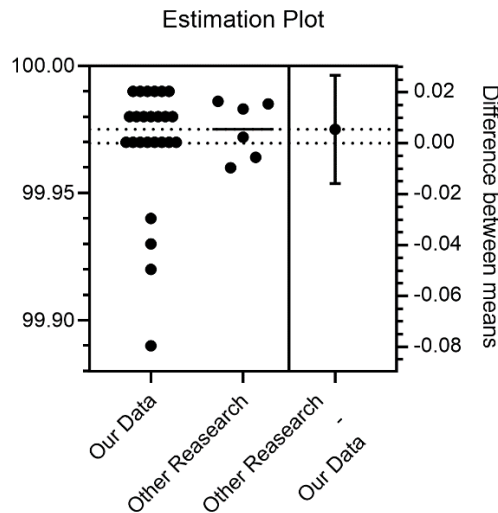


Figure 4. 3: Estimation plot: Unpaired t-test of Object Density of two groups

Table 4.2 represents the unpaired t-test results in detail. Here, it suggests that the two means are not significantly different from each other as the P value is higher than 0.05. However, even if the two means are almost equal, it would not be surprising to find means that are far from each other just by chance due to the small size of experimentation of the column B, resulting in larger P values.

Analyzed Data (Unpaired t-test)	Object Density
P Value	0.6071
Significantly different (P < 0.05)?	No
One- or two-tailed P value?	Two-tailed
t, df	t=0.5199, df=29
<i>How big is the difference?</i>	
Mean of column A (Our Data)	99.97
Mean of column B (Other Research)	99.98
Difference between means (B - A) ± SEM	0.005400 ± 0.01039
95% confidence interval	-0.01584 to 0.02664
R squared (eta squared)	0.009236
Sample size, column A	25
Sample size, column B	6

Table 4. 2: Unpaired t-test of Object Density: Tabular Results

Information about the other porosity ratios is provided following further normality tests and histograms, as shown in the plots below:

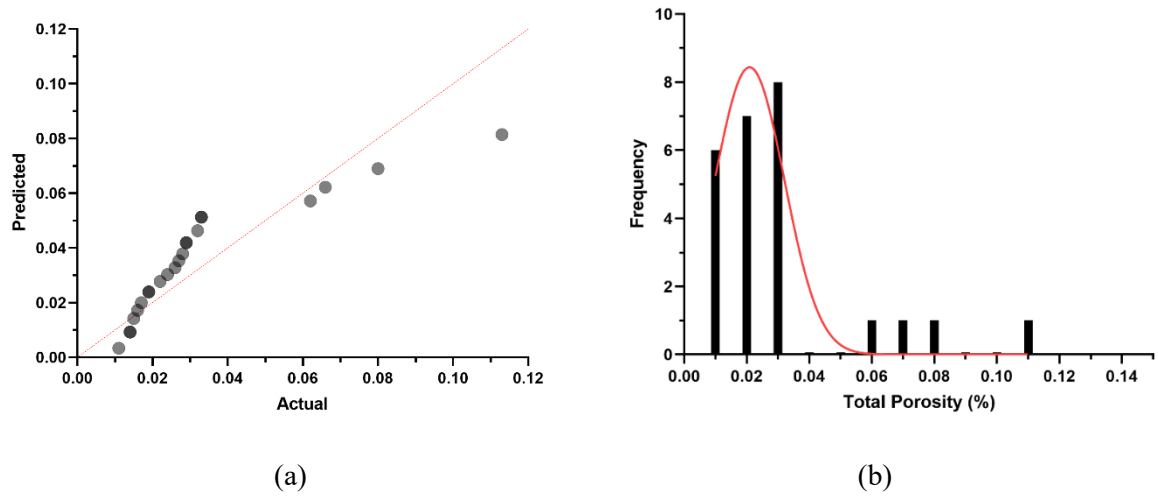


Figure 4. 4: Total Porosity: (a) Normal QQ plot, (b) Histogram with frequency distribution

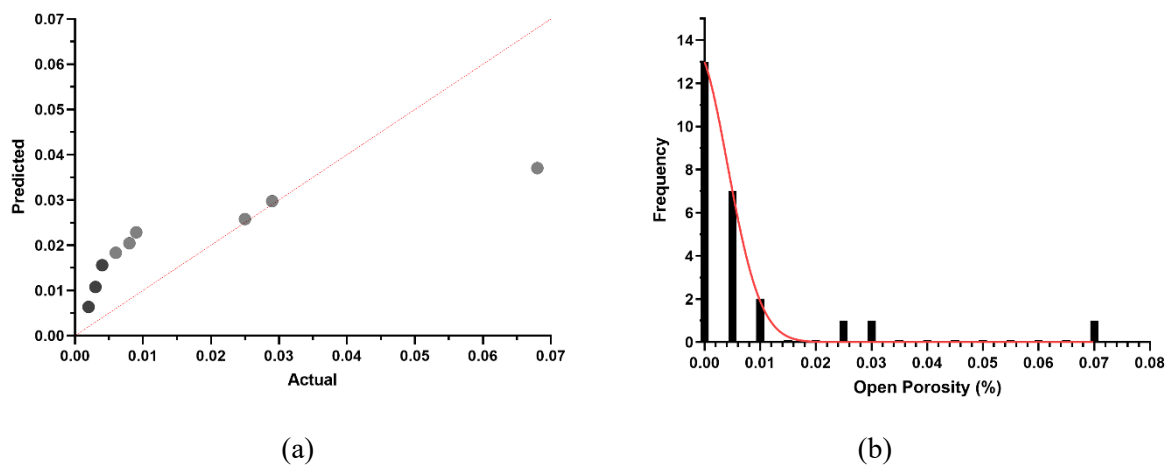


Figure 4. 5: Open Porosity: (a) Normal QQ plot, (b) Histogram with frequency distribution

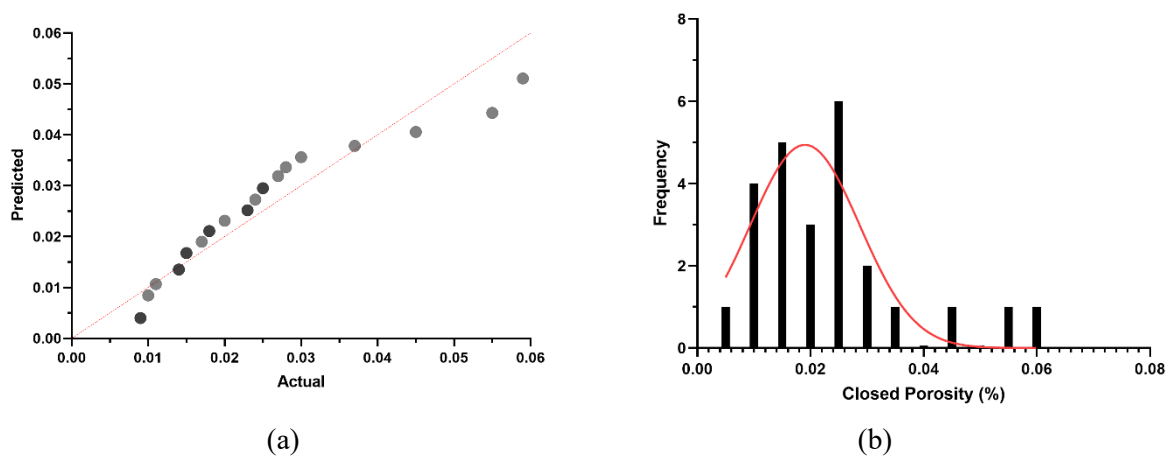


Figure 4. 6: Closed Porosity: (a) Normal QQ plot, (b) Histogram with frequency distribution

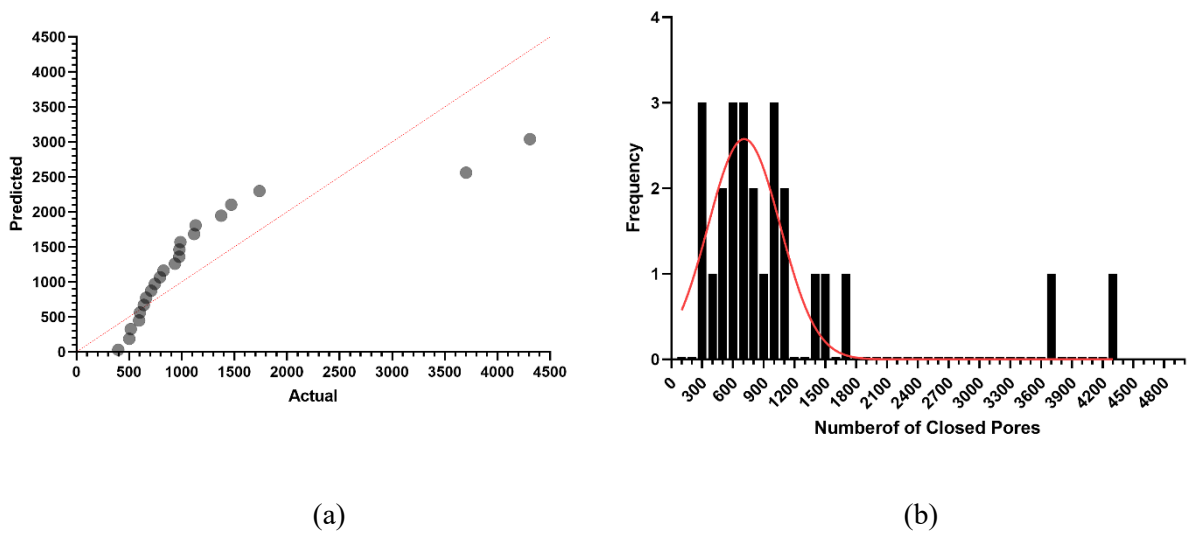


Figure 4. 7: Number of Closed Pores: (a) Normal QQ plot, (b) Histogram with frequency distribution

The contribution made by the closed pores to the total porosity is significantly higher than the open pores such that in some cases, the open porosity percentage drops as low as 0.001% and even 0%, which basically means that the total porosity almost wholly consists of only the closed pores in these specific instances. Fig. 4.8 depicts that closed porosity always has a major role in the total global porosity except for only one sample (specimen 19) which has an open porosity ratio of 0.068% and closed porosity of 0.045% (Each blue and orange dot in a vertical alignment together in Fig. 4.8 represents only one specimen e.g., specimen 19 is the one on the very right side of the graph and has a total porosity of $0.068 + 0.045 = 0.113\%$).

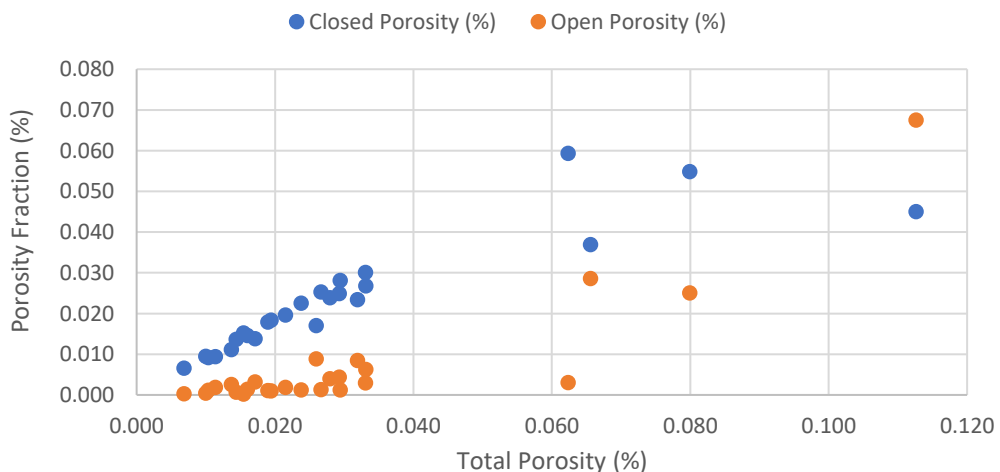


Figure 4. 8: Closed and open porosity scatter of the samples

Another outcome obtained from CTAn is the pore size range. There are six different pore size ranges found for different specimens. Some specimens only have pores of four

different sizes. To mention these ranges easier, numbers from 1 to 6 were given to each range. The size ranges obtained are as follows:

	Range (μm)	Mid-range (μm)
1	9.0014 - < 27.0042	18.0028
2	27.0042 - < 45.0069	36.0055
3	45.0069 - < 63.0097	54.0083
4	63.0097 - < 81.0125	72.0111
5	81.0125 - < 99.0152	90.0139
6	99.0152 - < 117.0180	108.0166

Table 4. 3: Pore size range

As can be seen from the Table 4.3, the largest pores found in one specimen are in the range of 99.0152 μm and 117.018 μm , and the smallest size pores are in the range of 9 μm and 27 μm . The micro-CT did not find pores smaller than 9 μm because of the pixel size choice in the scanning parameters. This parameter could have been larger but not smaller than 9 μm considering our specimen dimensions. It was, in fact, the smallest pixel size that could have been set in the CT scanner for our specimens. For smaller values, the CT scanner encountered an error for a possible collision of the specimen to the camera and the Cu filter due to the 360° rotation of specimens for image taking.

Table 4.4 shows the percent volume of pore sizes in range of each specimen that was analyzed by the CT. The specimens seem not to have pores of the 6th range except specimen 23. In Table 4.4, N_f values of fatigue specimens can be seen. So, even though specimen 23 has 0.9 % of the 6th range pores, it lasted the most among its group of fatigue samples of 3.6° twist angle. This finding may suggest that not always the size of the pore triggers to initiate or propagate the fatigue crack before smaller size pores. It should be the near location to the surface of a smaller pore that initiated the fatigue crack so that other samples that have more pores in the critical region (surface or sub-surface) failed earlier than specimen 23. This theory was also investigated in the next pages.

Fig. 4.9 is a visual representation of the percent volume of pore size ranges for the samples that have been fatigue tested. It can be easily seen which size of pores are the majority so that the pore size effect and the N_f shall be compared.

% Volume in range Specimen	9.0014 - 27.0042 μm (%)	27.0042 - 45.0069 μm (%)	45.0069 - 63.0097 μm (%)	63.0097 - 81.0125 μm (%)	81.0125 - 99.0152 μm (%)	99.0152 - 117.0180 μm (%)
1	40.3	36.1	18.9	3.8	0.9	0
2	71.8	21.6	4.6	1.5	0.5	0
3	77.3	19.9	2.5	0.35	0	0
4	56.2	27.7	11.6	4.5	0	0
5	25.9	47.7	18.2	8.2	0	0
6	22.5	43.8	19.1	11.6	2.9	0
7	20.6	48.9	27.3	3.2	0	0
8	18	43.5	25.8	10.9	1.8	0
9	31.2	41.2	21.2	6.4	0	0
10	40.45	39.7	15.6	4.2	0	0
11	31.7	43.8	20	3.8	0.7	0
12	44.6	32.3	19	3.1	1	0
13	45.9	29.2	15.5	7.8	1.6	0
14	33.2	38.4	21.6	6.2	0.7	0
15	21.6	51.1	21.9	4.5	0.9	0
16	29.5	40.7	22.9	5.9	1	0
17	17.1	49.6	22.2	10	1.1	0
18	26.9	44.6	20.2	5.9	2.4	0
19	62.4	20.4	11.8	5.1	0.3	0
20	23.2	46.7	22.5	6.6	1	0
21	23	46.1	22.3	5.1	1.1	0
22	25.1	50.1	17.9	5.7	1.2	0
23	30.8	41.0	22.1	5	0.3	0.9
24	24.6	52.8	16.7	5.8	0	0
25	19.6	45.3	25	9.1	1	0

Table 4. 4: % Pore size volume in range for all specimens

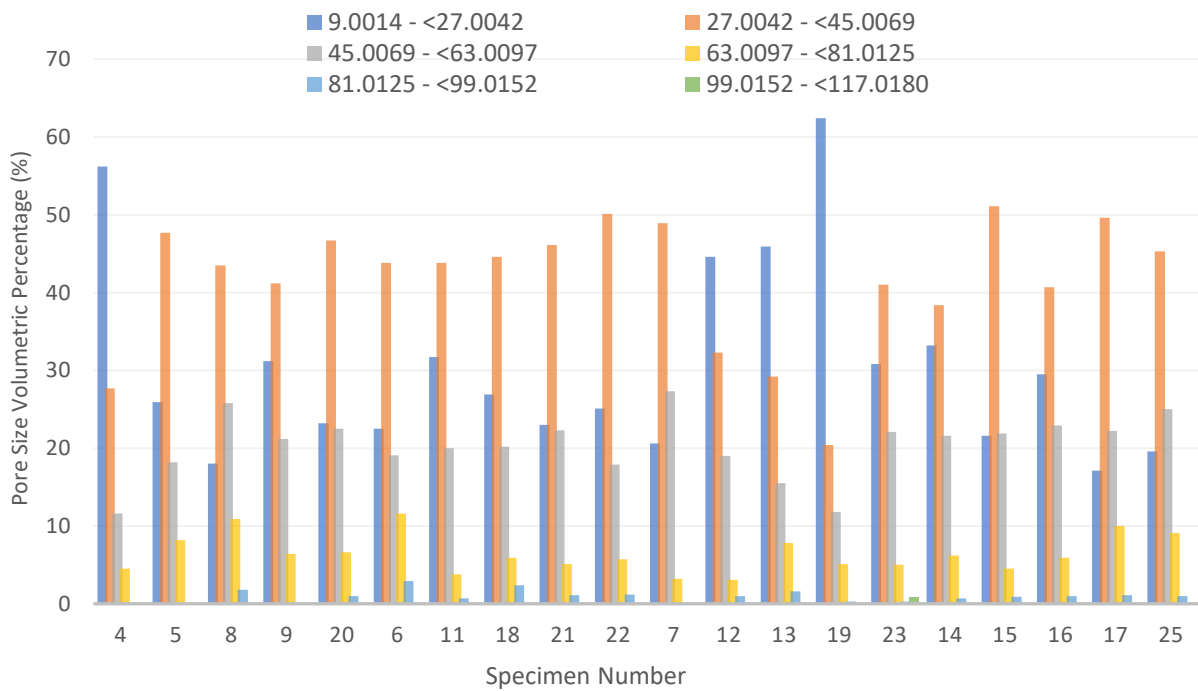


Figure 4. 9: % Pore size volume in range for fatigue specimens

4.2 Fatigue Test Results

Fatigue test results and porosity values were put together in a table to present and compare all the values. In Table 4.5, the four groups of fatigue tests of different twist angles are shown in color-coded rows. From top to bottom, 5.1°, 4.4°, 3.6°, and 2.7° twist angles used are listed as groups, respectively.

Specimen	Object Density (%)	Total Porosity (%)	Closed Porosity (%)	Open Porosity (%)	Number of Closed Pores	Number of pores in critical area	Angle of Twist (°)	Number of cycles to failure (N _f)
4	99.98	0.024	0.023	0.001	1470	353	5.06/-5.10	8584
5	99.99	0.011	0.009	0.002	397	301	5.07/-5.14	4818
8	99.98	0.019	0.018	0.001	595	454	5.08/-5.14	5795
9	99.98	0.017	0.014	0.003	516	373	5.08/-5.12	4560
20	99.97	0.033	0.030	0.003	1131	770	5.08/-5.12	5763
6	99.99	0.010	0.009	0.001	347	216	4.38/-4.42	15760
11	99.98	0.016	0.015	0.001	661	359	4.37/-4.44	19935
18	99.97	0.028	0.024	0.004	976	591	4.43/-4.45	19740
21	99.97	0.029	0.028	0.001	1118	657	4.38/-4.42	14207
22	99.98	0.019	0.018	0.001	794	451	4.38/-4.42	3327
7	99.99	0.007	0.007	0.000	262	174	3.66/-3.67	33765
12	99.97	0.026	0.017	0.009	640	493	3.64/-3.66	32950
13	99.93	0.066	0.037	0.029	1374	930	3.67/-3.69	28860
19	99.89	0.113	0.045	0.068	1739	1153	3.69/-3.70	27151
23	99.97	0.029	0.025	0.004	934	615	3.67/-3.69	43263
14	99.97	0.032	0.023	0.008	827	646	2.77/-2.79	113728
15	99.97	0.027	0.025	0.001	987	682	2.75/-2.75	103565
16	99.97	0.033	0.027	0.006	977	730	2.77/-2.77	81010
17	99.99	0.010	0.010	0.000	338	245	2.75/-2.76	126340
25	99.98	0.022	0.020	0.002	709	549	2.76/-2.77	103515

Table 4. 5: Porosity and N_f values of fatigue specimens

4.2.1 Porosity Ratios and Fatigue Life Comparison

Even though closed porosity is superior to the open porosity by volumetric percentages in almost all the samples, to understand better the effect of porosity on the fatigue life; total, closed, open porosity percentages, the number of closed pores, and the number of pores in the critical region versus the number of cycles to failure affection were investigated.

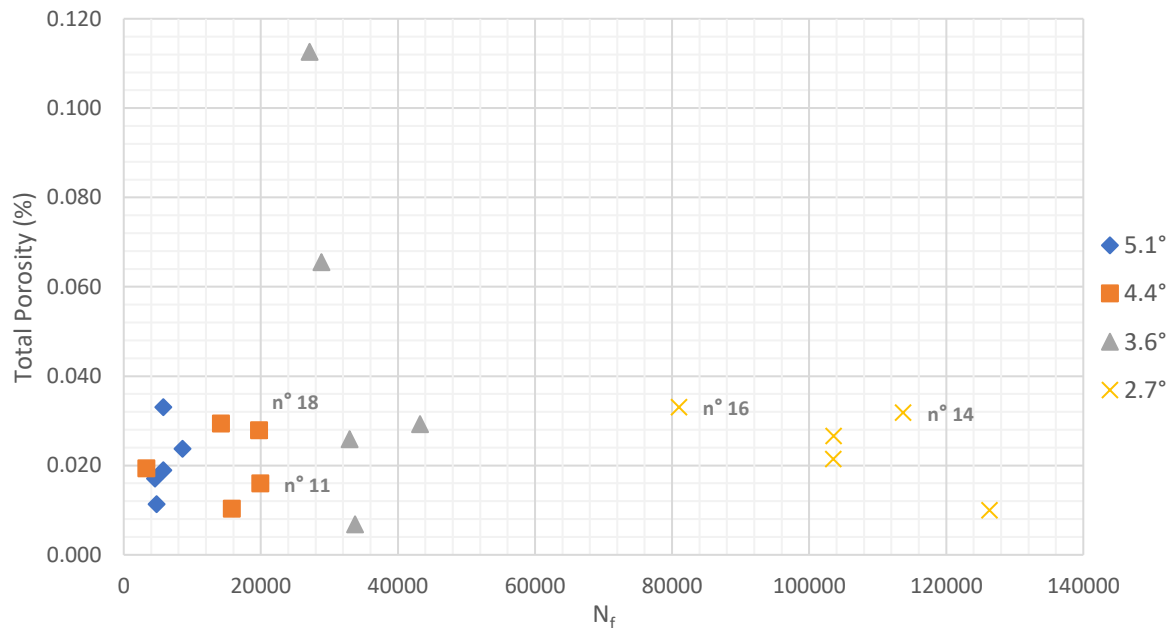


Figure 4. 10: Total porosity vs. number of cycles to failure (N_f)

It is seen in Fig. 4.10 that the total porosity (%) affects N_f for some of the cases but not always. Sometimes, specimens with higher porosity percentages have a higher N_f as opposed to the hypothesis stating that the higher the porosity, the lower the fatigue life. Two specimens (11 and 18) that have a different porosity have almost the same N_f. Another instance is specimens 14 and 16. They have quite different N_f even though their total porosity percentages are almost at the same level at 0.032% and 0.033%, respectively. Therefore, it is understood that even though some relations were found, there is not always a strong correlation between the total porosity percentage and N_f.

However, an investigation has been made to verify the theory: the reason for the diverging number of cycles to failure of the two specimens (14 and 16) that have very close porosity levels is thought to be the number of porosity is higher in the critical area in one of the specimens.

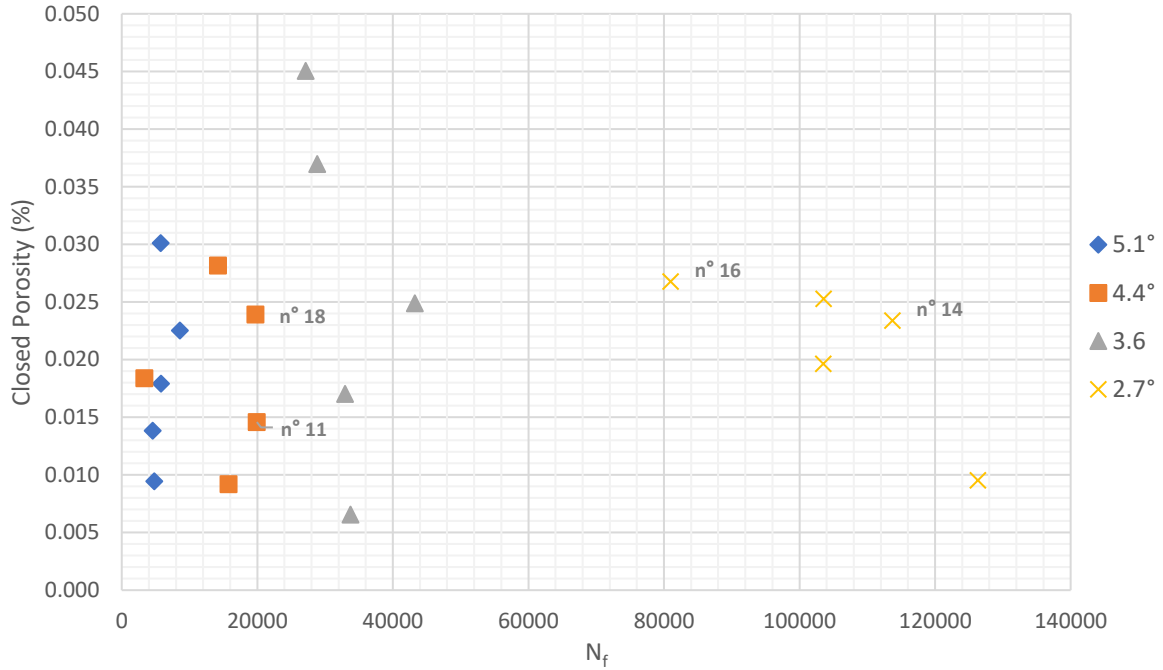


Figure 4. 11: Closed porosity vs. number of cycles to failure (N_f)

In Fig. 4.11, closed porosity % and N_f were put in a scatter chart to see the correlations. Even though a weak correlation was found for the 2.7° specimens, most of the specimens mainly exhibited a random behavior.

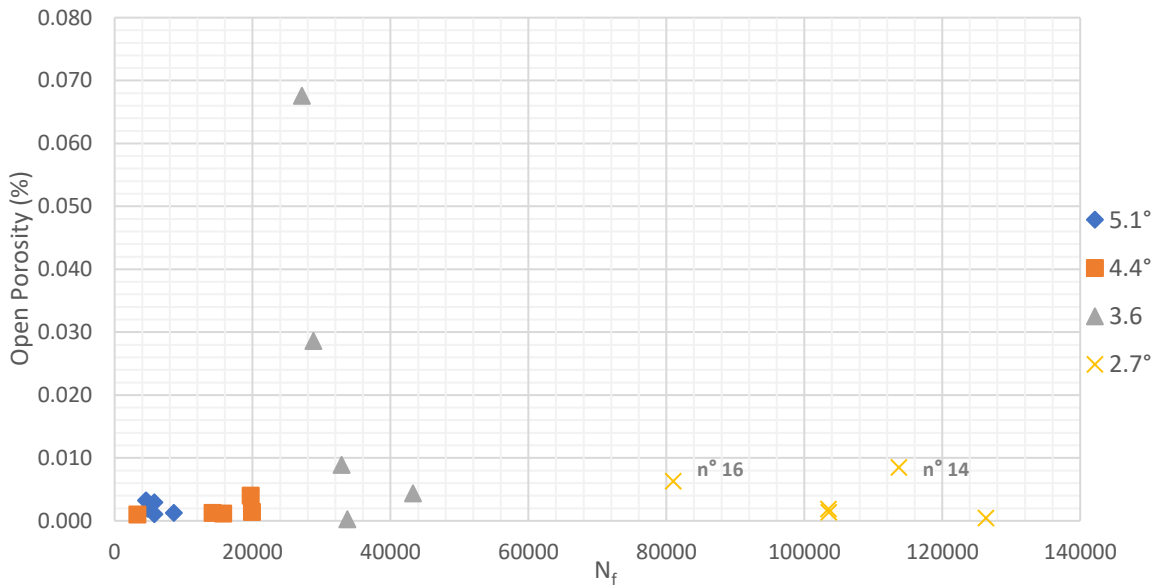


Figure 4. 12: Open porosity vs. number of cycles to failure (N_f)

Open porosity % and N_f relation was shown in Fig. 4.12. Again, there is not an absolute correlation between these variables too. In the 5.1° and 4.4° samples, clustered results were acquired. A reason for that may be the very small open porosity percentages. In the case of gray points, similar results were found as in closed porosity vs. N_f chart.

Another outcome that CTAn gave was the number of closed pores of each specimen. The behavior of N_f against the number of closed pores can be seen in Fig. 4.13. It is quite similar to the closed porosity % vs. N_f as the number of pores increases with the volumetric percentage of the closed porosity. Similarly, a random behavior observed except 2.7° and 3.6° specimens' weak correlation.

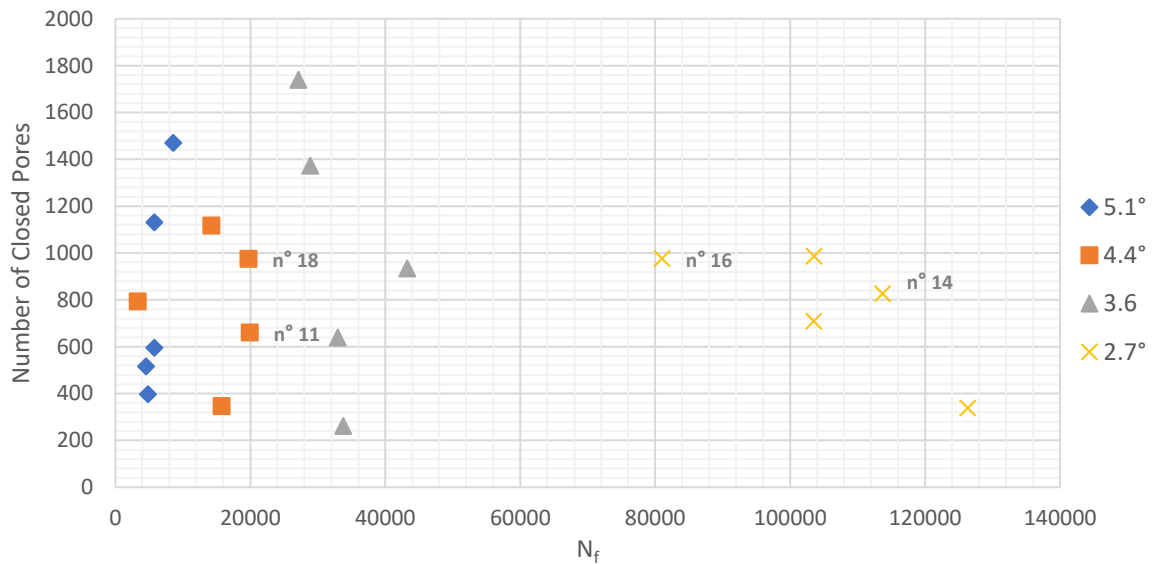


Figure 4. 13: Number of closed pores vs. number of cycles to failure (N_f)

Since these charts above didn't find a strong correlation between the porosity and N_f , another approach was adopted to try to explain these deviations from the hypothesis. For instance, the total porosity vs. N_f chart couldn't explain the high difference in N_f for specimens 14 and 16 even though their same total porosity percentage. Therefore, the number of pores in critical region vs. N_f was tried to explain this behavior.

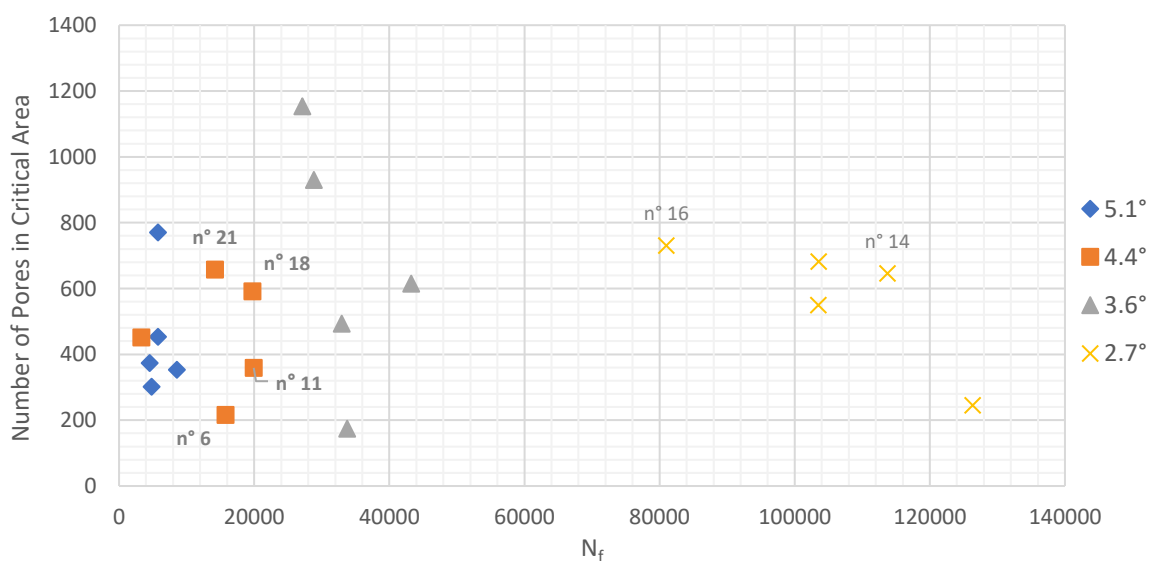


Figure 4. 14: Number of pores in critical area vs. number of cycles to failure (N_f)

The number of pores in the critical region against N_f was able to justify the difference in N_f as specimen 16 has 730 and specimen 14 has 646 pores in the critical region (Fig 4.14). However, this is not always the case for all the other specimens. For instance, specimen 21 has 657 pores whereas specimen 6 has only 216 pores in the critical region, but specimen 21 experienced almost the same N_f as specimen 6 (14.207 and 15760 cycles, respectively). Nevertheless, somehow a correlation is noticeable for 3.6° and 2.7° specimens as the number of pores increase, N_f decreases except for a few samples. Hence, a hypothetical statement may be that the lower the stress level, the more effective the number of pores on the fatigue life. Nonetheless, to confirm this hypothesis, more fatigue tests must be carried out in the HCF region, especially after $2 \cdot 10^5$ number of cycles.

We also compared the pore sizes and fatigue lives. Generally, from the literature, we can say that the bigger the pores, the lower the fatigue life. However, from the diagram, we cannot always observe this behavior. Some specimens that have smaller size pores failed before the specimens that have bigger pores as opposed to the expectation.

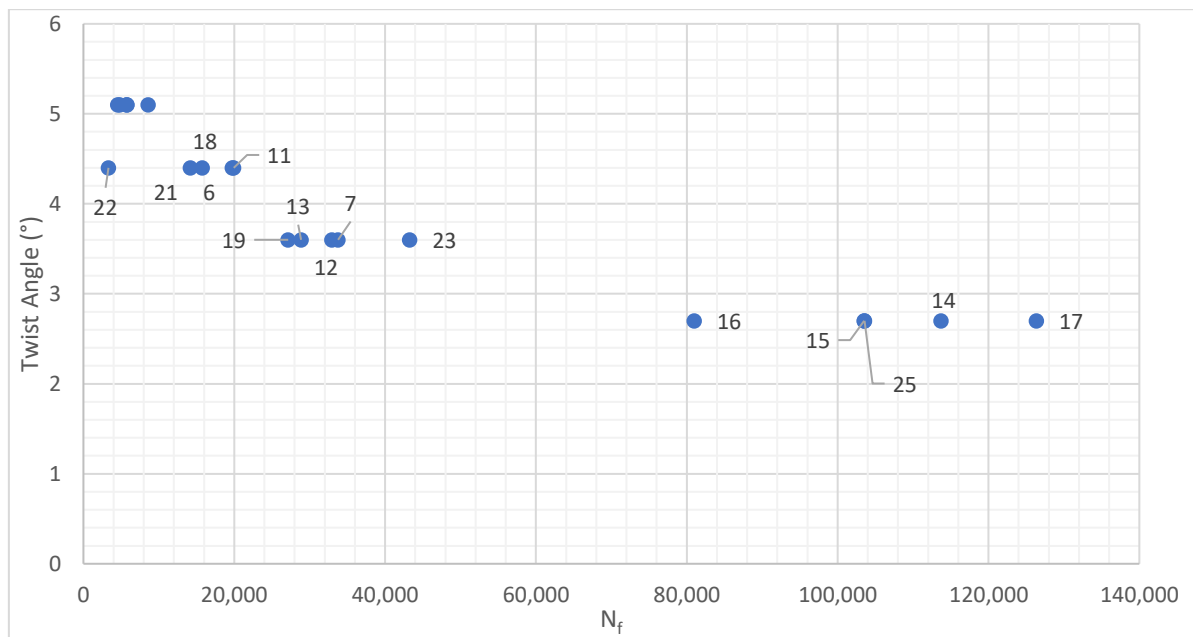


Figure 4. 15: Fatigue life depending on the pore size

Generally, from the literature, we can say that the bigger the pores, the lower the fatigue life. However, from Fig. 4.15, we cannot always observe this behavior. Some specimens that have smaller size pores failed before the specimens that have bigger pores as opposed to the expectation. For example, specimen 16 has a shorter fatigue life than specimen 17 even though specimen 17 has more bigger size pores than specimen 16. If we check also specimens 19 and 23, we will see a similar result. A reason for this, can be the individual locations of the pores. A specimen that has the smallest size pores on the surface or sub-surface may fail before the specimen that has the biggest size pores in the center of it.

4.2.2 Correlation Analysis

Correlation analyses have been conducted to understand to what extent the fatigue life is related to the porosity ratios analyzed. GraphPad Prism was used for the correlation analyses. The correlation analyses provide a value called the correlation coefficient (r) and its confidence intervals. The correlation coefficient r has a value ranging from -1 to 1, which -1 means a perfect inverse relationship; as one of the variables increases, the value of the other variable decreases. This type of correlation is what we are looking for since it is expected that when porosity increases, the fatigue life decreases. $r = 1$ means a perfect positive relationship, and $r = 0$ means there is no correlation at all between these two variables. One of the common correlation methods is Pearson correlation. It is used when the values from both variables are assumed to be sampled from populations with a Gaussian distribution. Hence, normalization tests have been conducted for every variable (porosity values, number of pores, etc.), and they were evaluated as normally distributed according to Shapiro-Wilk and Kolmogorov-Smirnov tests normality tests. Therefore, Pearson correlation was used for the correlation analyses. Pearson correlation allows us to interpret the r value by squaring it to calculate the R^2 (“ r squared”). It is a value that ranges from 0 to 1, indicating how one variable changes by the variation of the other. Another value that helps us understand more about the correlation is the P value. If the P value is small (usually smaller than 0.05), we can reject the hypothesis that the correlation is due to random sampling. Hence, we can say that a correlation exists. If the P value is large, the data doesn’t justify that the correlation is real (if found). This is not the same as saying there is no correlation at all; instead, we are not sure whether the correlation is true or occurred by chance. One should also look at the confidence interval to be more confident about the results. If the values in that range consist of near-zero numbers, we would have evidence that there is no correlation, or the correlation is weak. Otherwise, if the confidence interval values consist of correlation coefficients that would typically be associated with a strong correlation (like $r = -1$ or 1), then we cannot make strong conclusions from this experiment, meaning that we will need more data from a larger experiment.

Five different correlation analyses were done: The total, closed, and open porosity vs. N_f , the number of closed pores and number of pores in the critical region vs. N_f .

Value of r	Interpretation
1	Perfect correlation
0 to 1	The two variables tend to increase or decrease together
0	The two variables do not vary together at all
-1 to 0	One variable increase as the other decreases
-1	Perfect negative or inverse correlation

Table 4. 6: Interpretation of the correlation coefficient r

4.2.1.1 Total Porosity vs. N_f

Twist Angle	Pearson r	95% confidence interval	R ²	P value (two-tailed)
5.1°	0.4323	-0.7274 to 0.9516	0.1869	0.4673
4.4°	0.07276	-0.8650 to 0.8974	0.005294	0.9074
3.6°	-0.6452	-0.9734 to 0.5503	0.4163	0.2397
2.7°	-0.7193	-0.9798 to 0.4460	0.5174	0.1708

Table 4. 7: Correlation results of total porosity vs. N_f

Table 4.7 depicts the correlation analysis results of the total porosity vs. N_f . The highest correlation was found for the 2.7° twist angle as its correlation coefficient is the highest (inverse) among the others, with $r = 0.5174$. It simply means that 51.74% of the variance in N_f can be explained by variation in the total porosity. Also, twist angle 3.6° contains a correlation with $r = 0.4163$. Twist angles 4.4° and 5.1° are not even on the negative side of the correlation coefficient. The r value of 4.4° is almost zero, which indicates that there is no correlation at all. Also, the r value of 5.1° is near-zero. Hence, no evidence of a correlation between the total porosity and N_f found for these two test groups. However, the P values of all the test groups are significantly far from zero. This means we cannot state that the correlations found (even for 5.1° twist angle) are definitely real and not by chance. Also, the r confidence intervals are supportive of this conclusion as they are mostly extending from important negative correlation values to important positive values; for example, for 4.4°, the confidence interval is between -0.8650 and 0.8974, which means that both sides of the interval might be valid. On the contrary, a good correlation would have a tight confidence interval which is clustered on one side of the correlation coefficient. For instance, the confidence interval of the total porosity vs. closed porosity correlation was found to be between 0.7327 and 0.9436, with $r = 0.8746$ and $r^2 = 0.7650$.

4.2.1.2 Closed Porosity vs. N_f

Similar to the total porosity vs. N_f correlation, this analysis has also found a weak correlation for the 2.7° twist angle test group and no evident correlation results for the rest. Nonetheless, even though the P value of the 2.7° group is very close to 0.05, it is not smaller than that. Therefore, we still cannot say that the correlation is real and not due to random sampling.

Twist Angle	Pearson r	95% confidence interval	R ²	P value (two-tailed)
5.1°	0.5188	-0.6703 to 0.9611	0.2691	0.3705
4.4°	0.002423	-0.8817 to 0.8828	5.869e-006	0.9969
3.6°	-0.4755	-0.9565 to 0.7008	0.2261	0.4183
2.7°	-0.8225	-0.9879 to 0.2180	0.6764	0.0874

Table 4. 8: Correlation results of total porosity vs. N_f

4.2.1.3 Open Porosity vs. N_f

No good correlation was found for open porosity vs. N_f . It is thought that the reason for this is mainly the open porosity values found are highly similar to each other and such small difference does not really affect the fatigue behavior. Also, by looking at the confidence intervals, we can say that more tests are needed to verify the correlation reliability.

Twist Angle	Pearson r	95% confidence interval	R ²	P value (two-tailed)
5.1°	-0.6350	-0.9725 to 0.5623	0.4032	0.2497
4.4°	0.4248	-0.7317 to 0.9507	0.1804	0.4759
3.6°	-0.7102	-0.9790 to 0.4607	0.5044	0.1789
2.7°	-0.3901	-0.9466 to 0.7505	0.1522	0.1522

Table 4. 9: Correlation results of total porosity vs. N_f

4.2.1.4 Number of Closed Pores vs. N_f

The results found for this comparison are very similar to the closed porosity vs. N_f correlation as the volumetric closed porosity percentage, and the number of closed pores are highly correlated. For the 5.1° group, the positive r value of 0.8844 is misleading, and due to random sampling because we never expect an increase in fatigue life when the number of closed pores increases. On the contrary, we would expect to see the opposite

behavior and r having a value close to -1 . Another reason for this wrong interpretation could be a possible noise inclusion or an actual high-intensity smaller size porosity cluster around the internal regions of specimen 4 when analyzed for the porosity by the CT. If looked at the number of closed pores and number of pores in the critical area, the values are 1470 and 353, respectively. Usually, the difference between the number of closed pores and number of pores in critical region is not so high. Thus, this high number of closed pores might have caused misleading information from the correlation analysis.

Twist Angle	Pearson r	95% confidence interval	R^2	P value (two-tailed)
5.1°	0.8844	0.009854 to 0.9924	0.7822	0.0463
4.4°	-0.05213	-0.8933 to 0.8702	0.002717	0.9337
3.6°	-0.4840	-0.9574 to 0.6951	0.2343	0.4087
2.7°	-0.7838	-0.9850 to 0.3192	0.6144	0.1167

Table 4. 10: Correlation results of total porosity vs. N_f

4.2.1.4 Number of Pores in the Critical Region vs. N_f

As can be seen from the values on the Table 4.11, we cannot talk about an absolute correlation in this comparison too.

Twist Angle	Pearson r	95% confidence interval	R^2	P value (two-tailed)
5.1°	-0.03357	-0.8895 to 0.8746	0.001127	0.9573
4.4°	-0.02596	-0.8879 to 0.8764	0.0006741	0.9669
3.6°	-0.5065	-0.9598 to 0.6793	0.2565	0.3838
2.7°	-0.7940	-0.9857 to 0.2948	0.6304	0.1087

Table 4. 11: Correlation results of total porosity vs. N_f

4.2.3 S-N Curve

Fig. 4.16 is the log-log diagram obtained from the fatigue tests. It depicts the twist angle versus the number of cycles to failure. The equivalent stress amplitudes of the corresponding twist angles are also shown in the diagram. Furthermore, one can also obtain the stress levels of a chosen twist angle by using equations Eq. (9), (10), and (11) in section 3.2.12. The log-log straight regression line (tendency line) was placed to show the fatigue behavior of the material under the given fatigue test parameters.

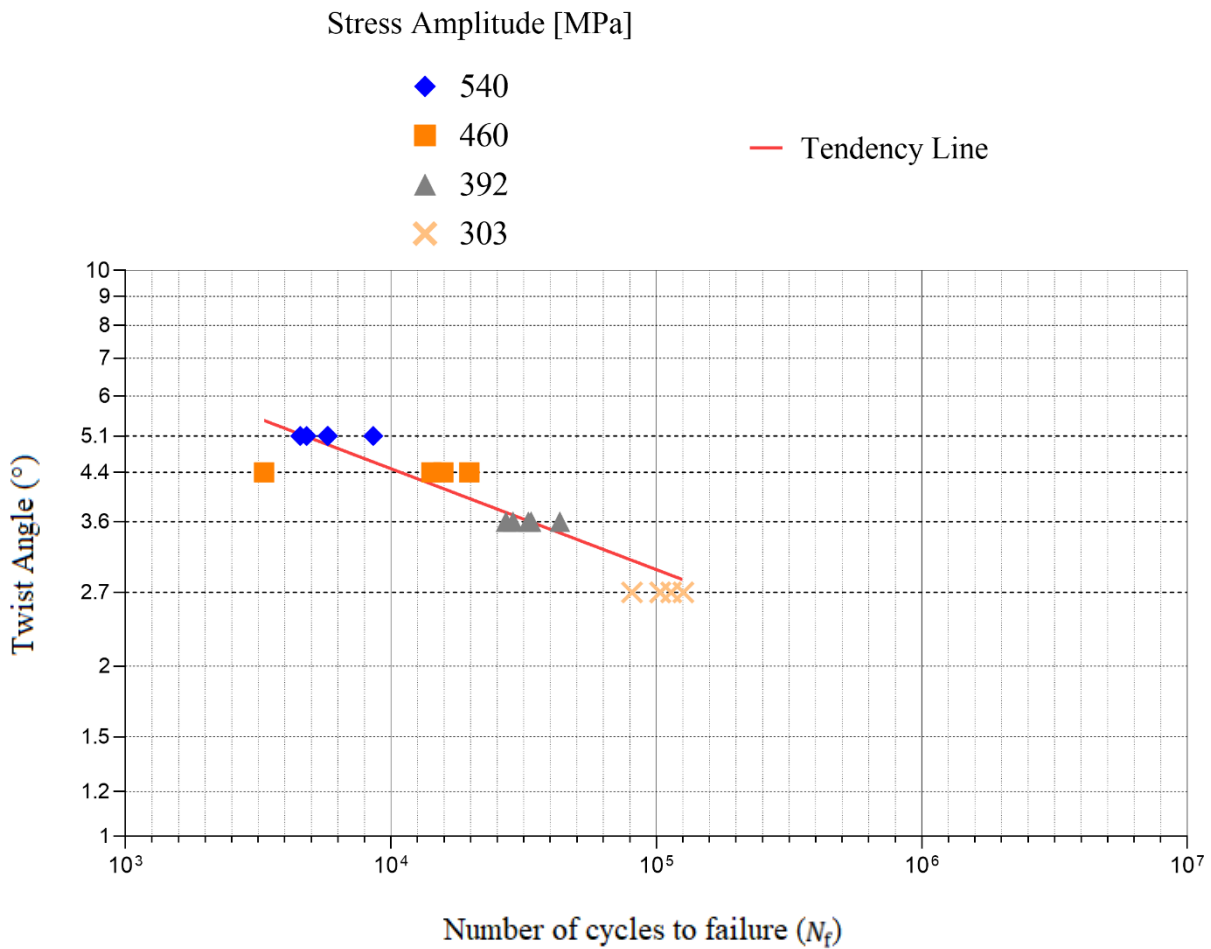


Figure 4. 16: Log-log plot of the angle of twist vs. number of cycles to failure (N_f)

5. CONCLUSIONS, RECOMMENDATIONS, AND LIMITATIONS

This master's thesis investigates the effect of porosity on the fatigue behavior of DMLS produced maraging steel 1.2709 with a chemical composition 18Ni9Co5Mo1Ti using 3D X-ray Computed Tomography and Torsion Fatigue Testing. The main objective of this work is to find a statistically significant correlation between the porosity and fatigue life and to build a stochastic model with this. In order to meet the final objective, the porosity percentages, object densities, total number of closed pores, number of pores in the critical area, and pore sizes in twenty-five fatigue test samples were found. Torsional fatigue test results were compared with the findings related to porosity. The following conclusions can be drawn from this study:

Twenty-five torsional fatigue test specimens were successfully produced using the DMLS method from the FeNiCo-based powder, which has a chemical composition similar to Werkstoff Nr. 1.2709 / X3NiCoMoTi 18-9-5. Aging heat treatment was applied at 490°C for 6 hours. The surface finish was improved by the rotary surface grinding machine for 28 hours. The high-resolution 3D X-ray micro-CT analyzed all the fatigue test specimens for their porosities. Twenty of them were fatigue tested by the custom-made torsion fatigue test machine. The porosity analysis by the micro-CT exposed the total, open, and closed porosity percentages, the number of closed pores, object densities, and pore sizes in six different ranges. The torsion fatigue tests revealed fatigue lives under four different twist angles; five tests were conducted for each twist angle. The average total porosity of the twenty-five specimens was found to be 0.03%. The highest porosity observed in one sample is 0.113% in specimen 19, whereas the specimen with the lowest total porosity is specimen 7 with 0.07%. The total porosity was found to be heavily controlled by the closed porosity as only a small fraction of the total porosity is composed of the open porosity.

Object densities are met with what the LPBF or DMLS technologies promise as they are capable of producing near full density parts. Furthermore, the metal powder provider indicates that the typical relative density percentage should be higher than 99.8% after the heat treatment operation. Moreover, the average object density was found to be 99.97% which is near fully dense. Hence, the machine capability is in good condition with the expectations.

The CT software measured six different pore size ranges. Pores sized between 27 and 45 μm are dominant in almost every specimen except for four samples having the smallest pores (between 9 and 27 μm) the most. The larger pores are the least present ones. Pores

between 81 and 99 μm aren't exceeded 3% in any specimen. In fact, seven samples don't even contain pores larger than 81 μm . Specimen 23 is the only sample with a pore size between 99 and 117 μm pore.

Specimen 16 and 14 failed at 81k and 113k cycles, respectively, despite exhibiting almost the exact amounts of the total, closed, and open porosity percentages. To find out the reason for different numbers of cycles exhibited, the number of pores in the critical region has been found. In fact, specimen 16 has 730, and specimen 14 has 646 pores in the critical area. Hence, it was thought to justify the different number of cycles to failure. However, the same comparison has been made with other specimens. It was observed that not every time the specimen with more pores in the critical region exhibits a shorter fatigue life, especially in higher stress levels.

The total porosity percentages of the specimens are highly similar to each other. The total object densities of different samples are alternating between 99.89% and 99.99%, which is only a 0.1% difference between the least dense and highest dense part. Also, the closed and open porosity percentages of the different specimens are highly similar to each other.

The pores formed from the AM process are spread out into the specimens, and not all the pores are as detrimental to the fatigue failure as those in the critical area. Stress concentrations occurred around the pores in the vicinity of the sub-surface area, and the magnitudes of Misses and S13 stresses exceeded the stress levels on the surface. The stress levels are hardly altered by the pores near the center of the model and should not affect the fatigue life. This conclusion was obtained from the FEM simulation.

After conducting correlation analyses, the conclusion made is that no absolute coherence was found between the measured global porosity (regardless of total, closed, and open porosity percentages or the number of pores) and fatigue life for the short-life fatigue as we have not found any correlation for the two higher stress levels we tested. It was attributed to the very similar amount of porosity of the printed samples. However, the effect of these values could be more visible if the difference was higher in different specimens. For long-life fatigue, especially after 100.000 cycles, we start to see a correlation even though it is not very strong. A correlation was observed for the twist angles 2.7° and 3.6°. Especially for the twist angle 2.7°, a correlation between porosity and fatigue life was found even though it is not very strong as the correlation coefficient r is close to -1 in many cases. So, we can state that correlation analyses found that at higher number of cycles, we can talk about the correlation between porosity and fatigue life. However, no correlation was found for the lower number of cycles/higher stress levels. Therefore, further fatigue tests should be performed in the HCF region for one million cycles, or if possible, even for ten million cycles to discover whether a stronger correlation

can be found. Also, more fatigue tests should be conducted for each stress level for more reliable correlation analysis.

The S-N curve found can be improved and further used to predict the fatigue lives under different stress levels or twist angles by inserting a regression line. The accuracy would be higher if more tests were conducted in the HCF regime.

Periodical CT scans with interrupted fatigue testing would reveal the effect of individual pores on the fatigue life. From this study, it was observed that the global porosity percentages (regardless of total, open or closed porosity) or the number of pores dispersed in the specimens do not strongly affect fatigue life when the porosity amounts are highly similar in each specimen. However, the effect of these values could be more visible when the difference was higher in different specimens. It would be more helpful to build a statistical material model for the fatigue life-porosity relation in the future if further researchers include the investigation of the effect of individual pores with their individual locations. This way, a statistical evaluation can be made with the probability of the detrimental pores being in the critical sub-surface region.

Time was a limitation for this master's thesis. The long duration of fatigue tests, especially in the HCF regime, prevented us from conducting more tests in lower torsion angles. The duration of the longest fatigue test was around 7 hours, reaching 126.340 cycles, and four other tests have been performed with the same torsion angle. If one million cycles were aimed to stop the fatigue tests, one test would take around 55.5 hours. Also, it should be noted that the minimum number of tests for each torsion angle is five, as indicated by the standard to build a correct S-N curve for fatigue lives. Furthermore, ten million cycles are also an option to stop the fatigue tests or call the specimens as runout if they are not failed after ten million. However, performing fatigue tests to ten million cycles is beyond the time constraints of this master's thesis since one test would last around 23 days to finish with the torsion fatigue test machine used, which is capable of applying cyclic loads at 5 Hz or lower.

APPENDIX A

TECHNICAL DRAWINGS

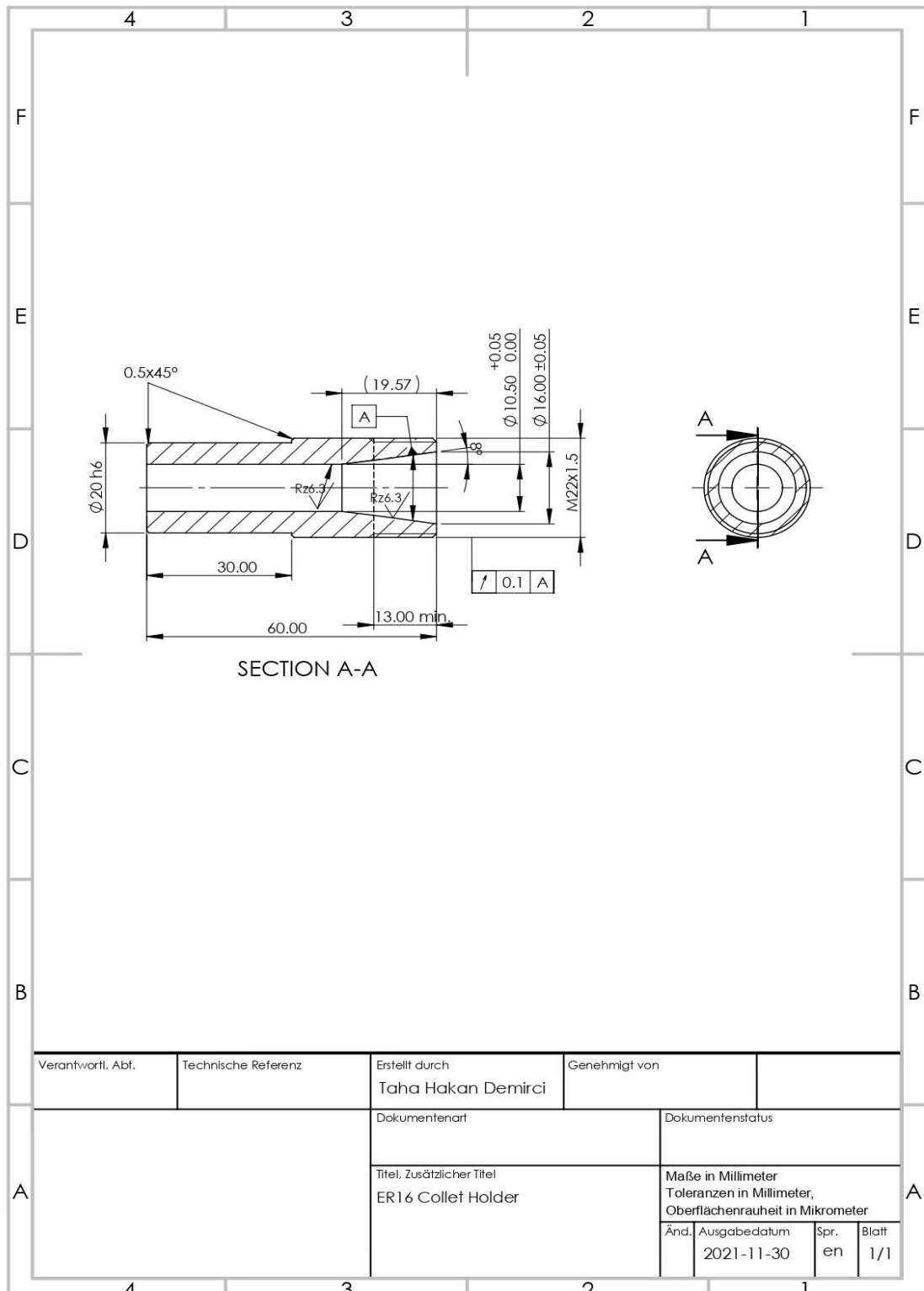


Figure A. 1: ER16 Collet Holder Technical Drawing

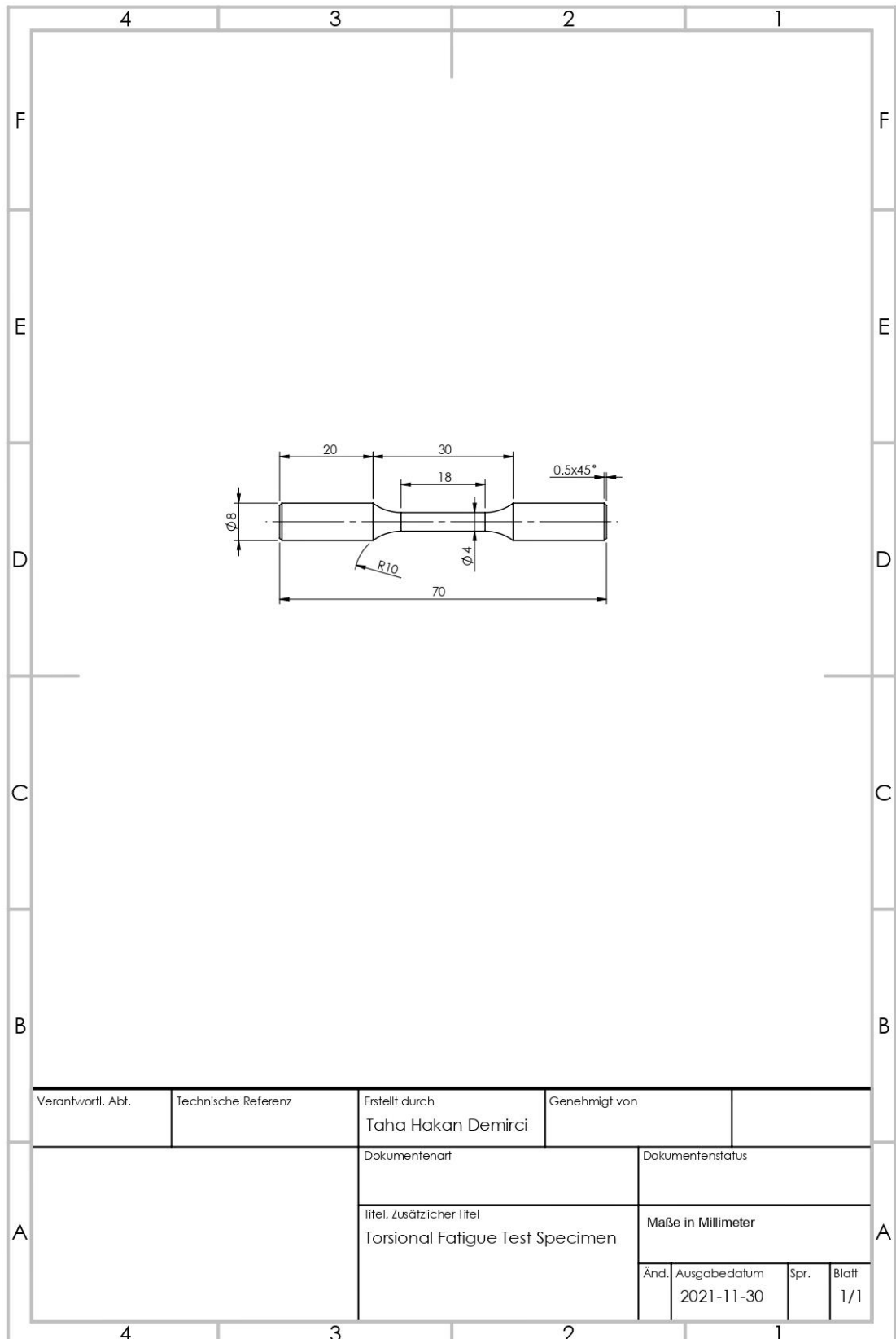


Figure A. 2: Torsional Fatigue Test Specimen Technical Drawing

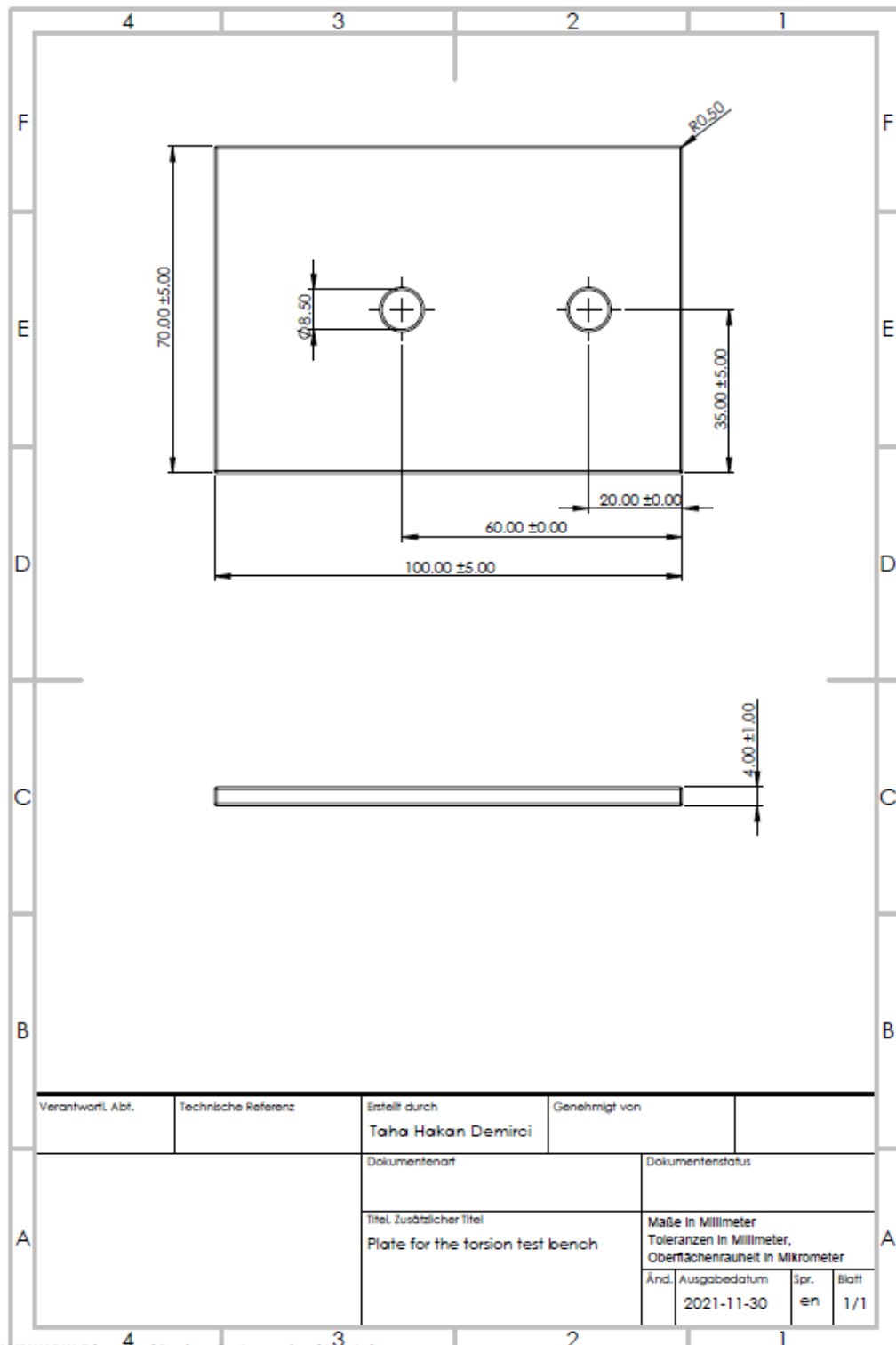


Figure A. 3: Straight Plate Technical Drawing

REFERENCES

- [1] ISO/TC, "ISO/ASTM 52900:2021," ISO/ASTM, 2021.
- [2] R. Shanmugam, "A Review on the significant classification of Additive Manufacturing," *Journal of Physics: Conference Series*, vol. 2027, 2021.
- [3] ASTM, "Standard Terminology for Additive Manufacturing Technologies," ASTM F2792, 2014.
- [4] Blakey-Milner et al., "Metal additive manufacturing in aerospace: A review," *Materials & Design*, vol. 209, 2021.
- [5] Sing et al., "Laser powder bed fusion for metal additive manufacturing: perspectives on recent developments," *Virtual and Physical Prototyping*, vol. 15, no. 3, pp. 359-370, 2020.
- [6] Cao et al., "Optimization of surface roughness and dimensional accuracy in LPBF additive manufacturing," *Optics & Laser Technology*, vol. 142, 2021.
- [7] John A. Slotwinski, Edward J. Garboczi, Keith M. Hebenstreit, "Porosity Measurements and Analysis for Metal Additive Manufacturing Process Control," *Journal of research of the National Institute of Standards and Technology*, vol. 119, p. 494–528, 2014.
- [8] Joy Gockel, Luke Sheridan, Brittanie Koerper, Bo Whip, "The influence of additive manufacturing processing parameters on surface roughness and fatigue life," *International Journal of Fatigue*, vol. 124, pp. 380-388, 2019.
- [9] Frondelius et al., "Stochastic continuum approach to high-cycle fatigue: Modelling stress history as a stochastic process," *European Journal of Mechanics - A/Solids*, vol. 92, 2022.
- [10] K. Sobczyk, "Stochastic Models for Fatigue Damage of Materials," *Advances in Applied Probability*, vol. 19, no. 3, pp. 652-673, 1987.
- [11] K. Tanaka, "4.04 - Fatigue Crack Propagation," in *Comprehensive Structural Integrity*, Pergamon, 2003, pp. 95-127.
- [12] S. M. Yongming Liu, "Stochastic fatigue damage modeling under variable amplitude

- loading," *International Journal of Fatigue*, vol. 29, no. 6, pp. 1149-1161, 2007.
- [13] G. Ziółkowski, E. Chlebus, P. Szymczyk, J. Kurzac,, "Application of X-ray CT method for discontinuity and porosity detection in 316L stainless steel parts produced with SLM technology," *Archives of Civil and Mechanical Engineering*, vol. 14, no. 4, pp. 608-614, 2014.
- [14] Romali Biswal et al., "Interrupted fatigue testing with periodic tomography to monitor porosity defects in wire + arc additive manufactured Ti-6Al-4V," *Additive Manufacturing*, vol. 28, pp. 517-27, 2019.
- [15] S. Tammam-Williams, P. J. Withers, I. Todd & P. B. Prangnell, "The Influence of Porosity on Fatigue Crack Initiation in Additively Manufactured Titanium Components," *Nature: Sci Rep*, vol. 7, no. 7308, 2017.
- [16] A. d. Plessis, I. Yadroitsava and I. Yadroitsev, "Effects of defects on mechanical properties in metal additive manufacturing: A review focusing on X-ray tomography insights," *Materials & Design*, vol. 187, 2020.
- [17] Charles W. Hull , "3DSYSTEMS," [Online]. Available: <http://www.3dsystems.com/files/downloads/3D-Systems-Charles-W-Hull-Executive-Bio.pdf>. [Accessed 6 2 2022].
- [18] A. Gebhardt and J.-S. Hötter, in *Additive Manufacturing - 3D Printing for Prototyping and Manufacturing*, 2016, pp. 1-2.
- [19] "TriMech Blog," [Online]. Available: <https://blog.trimech.com/a-brief-history-of-additive-manufacturing>.
- [20] "Twi-Global," [Online]. Available: <https://www.twi-global.com/technical-knowledge/faqs/faq-manufacturing-what-is-rapid-prototyping>.
- [21] KV Wong, A Hernandez, "A Review of Additive Manufacturing," *International Scholarly Research Network - ISRN Mechanical Engineering*, vol. Volume 2012, no. doi:10.5402/2012/208760, p. 10, 2012.
- [22] G. Profozich, "CMTC," [Online]. Available: <https://www.cmtc.com/blog/six-industries-benefiting-from-additive-manufacturing>. [Accessed 2022].
- [23] Francesco TAMBURRINO, Valeria PERROTTA, Raffaella AVERSA, Antonio APICELLA, "Additive technology and design process: an innovative tool to drive and assist product development," in *HERITAGE and TECHNOLOGY Mind*

Knowledge Experience, Aversa, Capri, 2015.

- [24] Ruth Jiang, , Robin Kleer, Frank T. Piller, "Predicting the future of additive manufacturing: A Delphi study on," *Technological Forecasting & Social Change*, vol. 117, p. 89, 2017.
- [25] S. Floreen, "Met. Rev., Review 126," p. 115, 1968.
- [26] King Wayne & Anderson et al., "Laser powder bed fusion additive manufacturing of metals; physics, computational, and materials challenges," *Applied Physics Reviews*, vol. 2, 2015.
- [27] M. Leary, Design for Additive Manufacturing, Vols. Chapter 11 - Powder bed fusion., Elsevier, 2020, pp. 295-319.
- [28] Zackary Snow, Abdalla R. Nassar, Edward W. Reutzler, "Invited Review Article: Review of the formation and impact of flaws in powder bed fusion additive manufacturing,," *Additive Manufacturing*, vol. Volume 36, 2020.
- [29] Zhiyuan Liu, Dandan Zhao, Pei Wang, Ming Yan, Can Yang, Zhangwei Chen, Jian Lu, Zhaoping Lu, "Additive manufacturing of metals: Microstructure evolution and multistage control," *Journal of Materials Science & Technology*, vol. 100, no. 1005-0302, pp. 224-236, 2022.
- [30] M.X. Gan, C.H. Wong, "Practical support structures for selective laser melting," *Journal of Materials Processing Technology*, vol. 238, pp. 474-484, 2016.
- [31] C. Yan, L. Hao, A. Hussein, P. Young and D. Raymont, "Advanced lightweight 316L stainless steel cellular lattice structures fabricated via selective laser melting," *Materials & Design*, vol. 55, pp. 533-541, 2014.
- [32] A. Moussa, D. Melancon, A. E. Elmi and D. Pasini, "Topology optimization of imperfect lattice materials built with process-induced defects via Powder Bed Fusion," *Additive Manufacturing*, vol. Volume 37, 2021.
- [33] Josef Tomas, Leonhard Hitzler, Marco Köller, Michael Sedlmajer, Ewald Werner and Markus Merkel, "The Dimensional Accuracy of Thin-Walled Parts Manufactured by Laser-Powder Bed Fusion Process," *Manufacturing and Materials Processing*, vol. 4, no. 3, 2020.
- [34] A. Cutolo, B. Engelen, W. Desmet and B. V. Hooreweder, "Mechanical properties of diamond lattice Ti–6Al–4V structures produced by laser powder bed fusion: On the

- effect of the load direction," *Journal of the Mechanical Behavior of Biomedical Materials*, vol. 104, 2020.
- [35] Singh et al., "Powder bed fusion process in additive manufacturing: An overview," *Materials Today: Proceedings*, Vols. Volume 26, Part 2, pp. 3058-3070, 2020.
- [36] Nesma T. Aboulkhair, Nicola M. Everitt, Ian Ashcroft, Chris Tuck, "Reducing porosity in AlSi10Mg parts processed by selective laser melting," *Additive Manufacturing*, Vols. 1-4, pp. 77-86, 2014.
- [37] S. Tammam-Williams et al., "XCT analysis of the influence of melt strategies on defect population in Ti–6Al–4V components manufactured by Selective Electron Beam Melting," *Materials Characterization*, vol. 102, pp. 47-61, 2015.
- [38] Cross, C. & Eliezer, Dan & Boellinghaus, Thomas, "The Role of Hydrogen in Titanium Alloy Weldments," in *22nd International Titanium Conference*, San Diego, 2006.
- [39] S.M. Gaytan, L.E. Murr, F. Medina, E. Martinez, M.I. Lopez, R.B. Wicker, "Advanced metal powder based manufacturing of complex components by electron beam melting," *Mater. Technol*, vol. 24, no. 3, p. 180–190, 2013.
- [40] S. Sun, M. Brandt, M. Easton, "2 - Powder bed fusion processes: An overview,," in *Laser Additive Manufacturing*, Woodhead Publishing, 2017, pp. 55-77.
- [41] Valérie Gunenthiram et al., "Analysis of laser–melt pool–powder bed interaction during the selective laser melting of a stainless steel," *Journal of Laser Applications*, vol. 29, no. 2, 2017.
- [42] Subin Shrestha, Thomas Starr, Kevin Chou, "A Study of Keyhole Porosity in Selective Laser Melting: Single-Track Scanning With Micro-CT Analysis," *Journal of Manufacturing Science and Engineering*, vol. 141, no. 7, 2019.
- [43] S. Kumar, "Selective laser sintering: A qualitative and objective approach," *JOM*, vol. 55, pp. 43-47, 2003.
- [44] Subrahmanyam et al., "CRITICAL REVIEW ON CHARACTERIZATION OF DMLS MATERIALS," *Journal of Xi'an University of Architecture and Technology*, vol. 14, pp. 665-688, 2020.
- [45] Ź. A. Mierzejewska, "Effect of Laser Energy Density, Internal Porosity and Heat Treatment on Mechanical Behavior of Biomedical Ti6Al4V Alloy Obtained with

DMLS Technology," *Materials*, vol. 12 (14), p. 2331, 2019.

- [46] Malekipour E. & El-Mounayri H., "Common defects and contributing parameters in powder bed fusion AM process and their classification for online monitoring and control: a review," *The International Journal of Advanced Manufacturing Technology*, vol. 95, pp. 1-4, 2018.
- [47] A. Townsend, N. Senin, L. Blunt, R. Leach and J. Taylor, "Surface texture metrology for metal additive manufacturing: a review," *Precision Engineering*, vol. 46, pp. 34-47, 2016.
- [48] Mukul Anand, Alok Kumar Das, "Issues in fabrication of 3D components through DMLS Technique: A review," *Optics & Laser Technology*, vol. 139, 2021.
- [49] A. I. Qurmoshi, "Additive manufacturing of stainless steel," Western Sydney University, Sydney, 2018.
- [50] M. Moshiri, "Integrated process chain for first-time-right mould components production using laser powder bed fusion metal additive manufacturing," Technical University of Denmark, PhD Thesis, 2020.
- [51] Ian Gibson, David W. Rosen, Brent Stucker, Additive Manufacturing Technologies (2nd), New York, USA: Springer, 2015.
- [52] Gu D, Shen Y, "Processing conditions and microstructural features of porous 316L stainless steel components by DMLS," *Appl Surf Sci*, vol. 255, pp. 1880-1887, 2008.
- [53] J. Cherry, H. Davies, S. Mehmood, N. Lavery, S. Brown and J. Sienz, "Investigation into the effect of process parameters on microstructural," *Int J Adv Manuf Technol*, vol. 76, pp. 869-879, 2015.
- [54] C. Hauser, "SELECTIVE LASER SINTERING OF A STAINLESS," University of Leeds, Leeds, 2003.
- [55] A. Chatterjee, S. Kumar, P. Saha, P. Mishra and A. Choudhury, "An experimental design approach to selective laser sintering of low carbon steel," *Journal of Materials Processing Technology*, vol. 136, pp. 151-157, 2003.
- [56] Tiago Czelusniak, Fred L. Amorim, Armin Lohrengel, Camila F. Higa, "Development and application of copper–nickel zirconium diboride as EDM electrodes manufactured by selective laser sintering," *The International Journal of Advanced Manufacturing Technology*, vol. 72, pp. 905-917, 2014.

- [57] H. Shipley et al., "Optimisation of process parameters to address fundamental challenges during selective laser melting of Ti-6Al-4V: A review," *International Journal of Machine Tools and Manufacture*, vol. 128, pp. 1-20, 2018.
- [58] S.Kumar, "Selective Laser Sintering/Melting," *Comprehensive Materials Processing*, vol. 10, pp. 93-134, 2014.
- [59] A. Yadollahi, N. Shamsaei, S. M. Thompson, A. Elwany and L. Bian, "Effects of building orientation and heat treatment on fatigue behavior of selective laser melted 17-4 PH stainless steel," *International Journal of Fatigue*, Vols. 94, Part 2, pp. 218-235, 2017.
- [60] A. E. Hawkins, *The shape of powder-particle outlines*, Taunton, Somerset, England: Research Studies Press, 1993.
- [61] H.H. Zhu, J.Y.H. Fuh, L. Lu, "The influence of powder apparent density on the," *Int. J. Mach. Tools Manuf.*, vol. 47, pp. 294-298, 2007.
- [62] G. Teixeira, "Fatigue of Metals: Failure and Success," researchgate.net, 2017.
- [63] Ribeiro, Alfredo & Correia, José & Silva, António & De Jesus, Abilio, "EVOLUTION OF FATIGUE HISTORY," in *21st Brazilian Congress of Mechanical*, Natal, 2011.
- [64] A. Wöhler, "Versuche zur Ermittlung der auf die Eisenbahnwagenachsen einwirkenden Kräfte und die Widerstandsfähigkeit der Wagen-Achsen," *Zeitschrift für Bauwesen*, vol. X, pp. 583-616, 1860.
- [65] "material-properties.org," [Online]. Available: <https://material-properties.org/what-is-fatigue-limit-fatigue-strength-definition/>. [Accessed 11 04 2022].
- [66] P. Strzelecki and T. Tomaszewski, "Application of Weibull distribution to describe S-N curve with using small number specimens," *AIP Conference Proceedings*, vol. 1780, no. 020007, 2016.
- [67] Jwo Pan, Mark Barkey, Yung-Li, *Fatigue Testing and Analysis*, Butterworth-Heinemann, 2005.
- [68] Sean Gallagher, Mark C. Schall Jr., "Musculoskeletal disorders as a fatigue failure process: evidence, implications and research needs,," *Ergonomics*, pp. 255-269, 2016.

- [69] G. Wang, Y. Ma, Z. Guo, H. Bian, L. Wang and J. Zhang, "Fatigue life assessment of high-strength steel wires: Beach marks test and numerical investigation," *Construction and Building Materials*, vol. 323, 2022.
- [70] A. Paul, "Materialpedia," *Materials Science Encyclopedia*, 2019. [Online]. Available: <https://materialpedia.materialsscience.net/2019/03/17/fatigue-life/>. [Accessed 18 June 2022].
- [71] Tec-Science, "Tec-Science," 7 July 2018. [Online]. Available: <https://www.tec-science.com/material-science/material-testing/fatigue-test/>. [Accessed 18 June 2022].
- [72] Withers et al., "X-ray computed tomography," *Nature, Nat Rev Methods Primers*, vol. 1, 2021.
- [73] L. De Chiffre, S. Carmignato, J.-P. Kruth, R. Schmitt, A. Weckenmann, "Industrial applications of computed tomography," *CIRP Annals*, vol. 63, no. 2, pp. 655-677, 2014.
- [74] Zhe Du, Yongguang Hu, Noman Ali Buttar, Ashraf Mahmood, "X-ray computed tomography for quality inspection of agricultural products: A review," *Food Science & Nutrition*, vol. 7, no. 10, pp. 3146-3160, 2019.
- [75] A. Thompson, I. Maskery and R. K. Leach, "X-ray computed tomography for additive manufacturing: a review," *Measurement Science and Technology*, 2016.
- [76] "matsusada.com," 02 11 2021. [Online]. Available: https://www.matsusada.com/column/xray_tube_ps.html. [Accessed 07 05 2022].
- [77] "oreilly.com," [Online]. Available: https://www.oreilly.com/library/view/biomedical-imaging/9783110423518/content/10_chapter03_4.xhtml. [Accessed 07 05 2022].
- [78] "bruker.com," [Online]. Available: <https://www.bruker.com/en/products-and-solutions/diffractometers-and-scattering-systems/x-ray-diffractometers/davinci-components/sources.html>. [Accessed 07 05 2022].
- [79] O. M. H. Ahmed, "Calculation of Beam Hardening in Industrial X-ray Computed Tomography and its Correction using Filtration and Linearization Methods," in *5th International Conference on Energy Equipment Science and Engineering*, 2020.
- [80] M.A. Ali, R. Umer, K.A. Khan, W.J. Cantwell, "Application of X-ray computed

tomography for the virtual permeability prediction of fiber reinforcements for liquid composite molding processes: A review," *Composites Science and Technology*, vol. 184, no. 19, 2019.

- [81] Bruker microCT in Belgium, "SkyScan 1275 User Manual V1.2," Kontich, 2016.
- [82] Mankovich N. J., Cheeseman A. M. and Stoker N. G., "The display of three-dimensional anatomy with stereolithographic models," *Journal of Digital Imaging (JDI)*, vol. 3, no. 200, 1990.
- [83] R., Spierings A. Schneider M. and Eggenberger, "Comparison of density measurement techniques for additive manufactured metallic parts," *Rapid Prototyping J.*, vol. 17, 2011.
- [84] Van Bael S., Kerckhofs G., Moesen M., Pyka G., Schrooten J. and and Kruth J-P, "Micro-CT-based improvement of geometrical and mechanical controllability of selective laser melted Ti6Al4V porous structures," *Mat. Sci. Eng. A*, vol. 528, 2011.
- [85] Truscello S., Kerckhofs G., Van Bael S., Pyka G., Schrooten J. and Van Oosterwyck H., "Prediction of permeability of regular scaffolds for skeletal tissue engineering: a combined computational and experimental study," *Acta Biomater*, vol. 8, 2012.
- [86] Wessel W. Wits, Simone Carmignato, Filippo Zanini, Tom H.J. Vaneker, "Porosity testing methods for the quality assessment of selective laser melted parts," *CIRP Annals - Manufacturing Technology*, vol. 65, pp. 201-204, 2016.
- [87] Shubham Saraf, Ajendra Singh, Bhawanisingh G Desai, "Estimation of Porosity and Pore size distribution from Scanning Electron Microscope image data of Shale samples: A case study on Jhuran formation of Kachchh Basin, India," *ASEG*, Vols. Volume 2019,, no. Issue 1: 2nd Australasian Exploration Geoscience Conference: Data to Discovery, pp. 1-3, 2019.
- [88] Koch A, Wittke P, Walther F., "Computed Tomography-Based Characterization of the Fatigue Behavior and Damage Development of Extruded Profiles Made from Recycled AW6060 Aluminum Chips," *Materials*, vol. 12, no. 15, 2019.
- [89] Péter Szalva, Imre Norbert Orbulov, "Fatigue testing and non-destructive characterization of AlSi9Cu3(Fe) die cast specimens by computer tomography," *fatigue & Fracture of Engineering Materials & Structures*, vol. 43, no. 9, pp. 1949-1958, 2020.
- [90] A. Brandão, J. Gumpinger, M. Gschweidl, P. C. Seyfert, Hofbauer and T. Ghidini,

- "Fatigue properties of additively manufactured AlSi10Mg-surface treatment effect," *Procedia Struct. Integr.*, vol. 7, pp. 58-66, 2017.
- [91] Q.C. Liu, J. Elambasseril, S.J. Sun, M. Leary, M. Brandt, P.K. Sharp, "The effect of manufacturing defects on the fatigue behaviour of Ti-6Al-4V specimens fabricated using selective laser melting," *Adv. Mater. Res.*, Vols. 891-892, p. 1519–1524, 2014.
- [92] Olivier Andreau et al., "A competition between the contour and hatching zones on the high cycle fatigue behaviour of a 316L stainless steel: Analyzed using X-ray computed tomography," *Materials Science and Engineering*, vol. 757, pp. 146-159, 2019.
- [93] Junwen Zhao, Mark Easton, Ma Qian, Martin Leary, Milan Brandt, "Effect of building direction on porosity and fatigue life of selective laser melted AlSi12Mg alloy," *Materials Science and Engineering*, vol. 729, pp. 76-85, 2018.
- [94] S. Romano, A. Brandão, J. Gumpinger, M. Gschweidl, S. Beretta, "Qualification of AM parts: Extreme value statistics applied to tomographic measurements," *Materials & Design*, vol. 131, pp. 32-48, 2017.
- [95] F. A. Kandil, "The UNCERT manual of codes of practice for the determination of uncertainties in mechanical tests on metallic materials," in *National Physical Laboratory*, Teddington, UK, 2000.
- [96] J. V. D. Avyle, "LOW CYCLE FATIGUE OF TUBULAR SPECIMENS," *Scripta METALLURGICA*, vol. 17, pp. 737-740, 1983.
- [97] Y. Li, Z. Chen, L. Lin, S. Liu, H. Wang and J. Zhang, "Effect of pores on the stress field of high-frequency vibration of TC17 specimen manufactured by laser additive," *Int J Fract*, 2022.
- [98] J. Feil, "SkyScan Tutorial," RJL Micro & Analytic GmbH, Karlsdorf-Neuthard, 2016.
- [99] Andronov, Šimota, Beránek, Blažek and Rušar, "Optimization of Process Parameters for Additively Produced Tool Steel 1.2709 with a Layer Thickness of 100 μm ," *Materials*, vol. 14, no. 11, 2021.
- [100] A. International, "ASTM," [Online]. Available: <https://www.astm.org/about/overview/fact-sheet.html>. [Accessed 3 March 2022].
- [101] A. Porreco, "www.portlandbolt.com," Portland Bolt, 10 October 2011. [Online].

Available: <https://www.portlandbolt.com/technical/faqs/calculating-strength/>.
[Accessed 02 05 2022].

[102] Weisstein Eric W, "Wolfram Mathworld," From MathWorld - A Wolfram Web Resource, [Online]. Available: <https://mathworld.wolfram.com/RadonTransform.html>. [Accessed 07 05 2022].